Compact few-cycle mid-wave and long-wave infrared OPCPA

based on a Cr:ZnS front-end

Dissertation
zur Erlangung des akademischen Grades

DOCTOR RERUM NATURALIUM (Dr. rer. nat.)

im Fach Physik:
Spezialisierung: Experimentalphysik

eingereicht an der
Mathematisch-Naturwissenschaftlichen Fakultät der
Humboldt-Universität zu Berlin
von

M.Sc. Pia Johanna Fürtjes

Präsidentin der Humboldt-Universität zu Berlin
Prof. Dr. Julia von Blumenthal

Dekanin der Mathematisch-Naturwissenschaftlichen Fakultät
Prof. Dr. Caren Tischendorf

1. Gutachter: Prof. Thomas Elsässer
2. Gutachter: Prof. Oliver Benson
3. Gutachterin: Prof. Clara Saraceno

Tag der mündlichen Prüfung: 22. Mai 2023

Zusammenfassung

Die Weiterentwicklung von Ultrakurzimpulslaserquellen hat die Horizonte für Wissenschaft, Medizin und Industrie stetig erweitert. Ultrakurze Impulsdauern und hohe Energien erzeugen Spitzenleistungen auf der Gigawatt-Skala, deren zeitliche und spektrale Charakteristik ideale Voraussetzungen für nichtlineare zeitaufgelöste Spektroskopie und ultraschnelle nichtlineare Optik bieten. Die Untersuchung von Molekülschwingungen im sogenannten *Fingerabdrucksbereich* (engl. *fingerprint region*) und die effiziente lasergetriebene Erzeugung von Hohen-Harmonischen- und Röntgenimpulsen benötigen Laserquellen im mittleren bis langwelligen Infrarot. Da oberhalb einer Wellenlänge von 4 µm keine Festkörperlaserquellen existieren, hat sich optische parametrische Verstärkung zur Schlüsseltechnik in diesem Wellenlängenbereich entwickelt.

In dieser Arbeit werden Laserimpulse oberhalb von 4 µm Wellenlänge mittels optischer parametrischer Verstärkung gestreckter Impulse erzeugt, deren Energien den Micro- bis Millijoule Bereich bei einer Kilohertz-Wiederholrate erreichen. Die Pumpwellenlänge von 2 µm ist vorteilhaft gegenüber den üblicherweise verwendeten Pumpen im nahen Infraroten und erlaubt zur Generation der Eingangsspektren besonders innovative kompakte Laserarchitekturen. Der Cr:ZnS Masteroszillator bei 2.4 µm und einer Impulsdauer von 30 fs liefert alle spektralen Komponenten zur Erzeugung der 2 µm Pumpimpulse und Signalimpulse. Die Pumpquelle ist ein regenerativer Verstärker basierend auf dem Kristall Ho:YLF und liefert bei 1 kHz Repetitionsrate Impulse einer Dauer von 3 ps. Mit einer Ausgangsenergie von 13.4 mJ und einer Stabilität von 0.35 % stellt dieser Verstärker eine exzellente Pumpquelle für mehrstufige parametrische Verstärkersysteme im mittleren bis langwelligen infraroten Spektralbereich dar.

Für den Verstärker im mittleren Infrarotspektralbereich werden die Signalimpulse bei 2.4 µm in einer Fluoridfaser durch den Raman-Effekt in ihrer Frequenz verschoben. In dem nichtlinearen Kristall $ZnGeP_2$ werden die Idlerimpulse durchstimmbar zwischen 5.4 und 6.8 µm Wellenlänge mit bis zu 400 µJ Energie erzeugt, die auf unter 100 fs Impulsdauer komprimierbar sind. Mit diesen Parameters ist dieser Verstärker einzigartig in seiner Durchstimmbarkeit und Ausgangsenergie. Im langwelligen Infrarotspektralbereich können die Impulse des Oszillators für das Signal direkt verwendet werden und ergeben Idlerimpulse bei 11.4 µm Wellenlänge. Im nichtlinearen Kristall GaSe werden Impulse mit einer Energie von 70 µJ, komprimierbar auf 185 fs erzeugt, und ergeben eine bisher unerreichte Spitzenleistung von 0.35 GW. Das dazugehörige Spektrum überlappt mit der Absorptionsbande der Libration L2 von flüssigem Wasser bei 660 cm^{-1}. Die hohen Impulsenergien ermöglichen erstmals nichtlineare Absorptionsmessungen durch direkte Anregung. Der Vergleich zwischen den experimentellen Ergebnissen und der Lösung von quantenbasierten Übergangsratengleichungen erlaubt eine Abschätzung der Lebensdauer der Librationsanregung auf unter 20 fs.

Abstract

The progress in the development of ultrafast laser sources has opened up new horizons in science, medicine and industry. Pulses of ultrashort duration and high energy reach gigawatt peak power which offer ideal conditions for time-resolved nonlinear absorption spectroscopy and ultrafast nonlinear optics. The investigation of vibrational states of biomolecules in the so-called *fingerprint region* and strong-field experiments aiming for the generation of high-harmonics or x-rays quest for such laser sources in the mid- to long-infrared spectral range. Due to the lack of existing solid state lasers beyond 4 µm, optical parametric amplification has emerged as the key technique to generate adequate infrared pulses.

In this work, optical parametric chirped pulse amplification (OPCPA) is the key technique used to generate 100 µJ-level energy pulses at kHz repetition rate beyond 4 µm. In this context, novel front-end architectures are designed, tailored to compactness and to exploit the advantages of 2 µm pumped OPCPA over the typically used near-infrared drivers around 1 µm. The novel front-end based on a femtosecond Cr:ZnS oscillator emitting 30 fs pulses at 2.4 µm provides the necessary spectral components for the 2 µm pump and the signal. This approach avoids complicated front-end architectures relying on multiple nonlinear stages to provide the necessary seed wavelengths. The 2 µm pump is a mature regenerative amplifier based on the gain crystal Ho:YLF, providing intense pulses at a 1 kHz repetition rate with a 3.0 ps pulse duration. Its output energy of 13.4 mJ has an excellent stability of 0.35 % and is used as the pump for OPCPA systems in the mid- and long-wave infrared with multiple stages.

The mid-infrared OPCPA system is unique in terms of tunability range and output power. The signal pulses of the Cr:ZnS oscillator are self-frequency shifted in a fluoride fibre and generate idler pulses between 5.4 and 6.8 µm in the nonlinear crystal $ZnGeP_2$. With a record output energy of 400 µJ, these pulses are compressible down to sub-100 fs.

The long-wave infrared OPCPA uses the femtosecond seed pulses centred at 2.4 µm directly for the pump and the signal to generate idler pulses at 11.4 µm with unprecedented energy, overcoming the stagnant maximum energy of a few-µJ for two decades. Three parametric stages based on GaSe crystals amplify the idler pulses to 70 µJ which are compressed to 185 fs. The peak power of 0.35 GW enables nonlinear absorption measurements of water librations for the first time. The idler spectrum overlaps with the librational L2 band centred at $660\,\mathrm{cm}^{-1}$. The analysis of the experimental results with a two-level rate equation approach suggests a sub-20 fs lifetime of the librational excitation.

"Ich ziehe es vor, mich mit Menschen zu umgeben, die ihre Unvollkommenheit offenlegen, anstatt ihre Vollkommenheit zu fälschen." - *Charles F. Glassman*

Table of Contents

Title Page i

Zusammenfassung iii

Abstract v

List of Figures xi

1 Introduction 1

2 Theoretical background 7
- 2.1 Pulses in dielectric media 7
- 2.2 Dispersion 9
- 2.3 Three wave mixing 10
- 2.4 Birefringence of uni- and biaxial crystals 11
- 2.5 Parametric Amplification 12
  - 2.5.1 Chirped Pulse Amplification 16
- 2.6 Optical Kerr effect 18
- 2.7 Nonlinear Schrödinger Equation 20

3 Design concepts of high-energy mid-IR OPCPAs 23
- 3.1 Infrared crystals and materials 24
- 3.2 Parametric amplification in ZGP and GaSe 27
  - 3.2.1 Collinear and non-collinear phase matching 27
  - 3.2.2 Influence of group velocity mismatch - comparing 1 µm and 2 µm pumping 29
  - 3.2.3 Wavelength tuning in GaSe 31
  - 3.2.4 Spatio-temporal distortion 33
- 3.3 Temporal dispersion management 34
  - 3.3.1 Dispersion management in bulk material 34
  - 3.3.2 Compensation of higher-order phases 35
- 3.4 Bandwidth and efficiency optimization 37
  - 3.4.1 Parametric Gain 37
  - 3.4.2 Pulse duration ratio between signal to pump 39
  - 3.4.3 Spatio-temporal pulse shape optimization 42
- 3.5 Summary for LWIR OPCPA in GaSe 45

4 Regenerative amplifier based on Ho:YLF 47
4.1 Dynamics of high repetition rate regenerative amplifiers 48
4.2 Simulation of the regenerative amplifier 49
4.3 Technical details 50
4.4 Spectral broadening of RA output pulses 53

5 Front-end for mid-wave and long-wave infrared OPCPA 55
5.1 Femtosecond Cr:ZnS front-end oscillator 57
5.2 LWIR front-end 58
5.3 MWIR front-end 59
  5.3.1 Raman self-frequency shifting of signal pulses 60
  5.3.2 Simulation of pulse evolution inside the fibre 63
  5.3.3 Energy stability and timing jitter of the soliton 64

6 Mid-wave infrared OPCPA 69
6.1 Two stage optical parametric amplifier 70
6.2 Spectral characterization 73
6.3 Temporal characterization 73
6.4 Precise phase shaping with AOPDF 74

7 Long-wave infrared OPCPA 79
7.1 Experimental setup 80
7.2 Spectral analysis 83
7.3 Temporal analysis 84
7.4 FROG measurement and output stability 85
7.5 Comparison with simulation 87

8 Nonlinear absorption of water 89
8.1 Experimental implementation 90
8.2 Theoretical approach 92
8.3 Analysis of the experimental results 95

9 Summary and outlook 97

References 99

Appendix A Glossary 111

Appendix B Publications 115

Appendix C Selbstständigkeitserklärung 117

Appendix D Danke 119

List of Figures

1.1 Overview of laser sources, typically used for accessing the infrared spectral range directly or via parametric interaction by providing the seed spectra. Shown laser types: solid state lasers (SSL), semiconductor lasers in the infrared (Quantum Cascade Lasers (QCL)), and gas lasers relying on various gas mixtures (adapted from [25] Fig. 1.6). 2
1.2 Schematic representation of optical parametric chirped pulse amplification (OPCPA). The signal seed is stretched from femtosecond to picosecond pulse duration prior to the optical parametric amplification process, where the signal is amplified and a third idler beam is created. Subsequent compression of the signal and/or idler pulses leads to pulse ultrashort durations. 3
1.3 State of the art of few optical cycle table-top OPCPA systems, showing the high number of systems between 0.8 and 4 µm system. The longer the wavelength the more sophisticated is the system architecture and the lower is the output power. Beyond a wavelength of 4 µm, all systems rely on $ZnGeP_2$ (ZGP) or $LiGaS_2$ (LGS), and the number is fairly limited. Figure adapted from [39], see paper for detailed references. Please find the abbreviations of the crystals in Appendix A. 5

2.1 Parametric processes: (a) SHG, (b) SFG, (c) DFG 10
2.2 (a) Collinear and (b) non-collinear phase matching geometry, where k_1 is the wave vector of the pump, k_2 of the signal and k_3 of the idler. Non-collinear geometry allows typically for a broader bandwidth than collinear geometry. . . 11
2.3 Definition of phase matching angle in birefringent crystals: (a) uniaxial crystal where the extraordinary refractive index is along $\hat{z}$, the grey plane is the phase matching plane rotating around $\hat{y}$. (b) biaxial crystal where $n_\perp$ indicates the normal incident vector of the phase matching plane. For $\phi = 0$ the biaxial crystal resembles the uniaxial one with a phase matching plane rotating around $\hat{y}$. 12
2.4 Evolution of the pump and signal photon flux with increasing parametric amplification for Gaussian intensity profiles. The central part of the pump pulse is depleted before the signal pulses saturate. The following backconversion process reversing the energy transfer limits the conversion efficiency of an optical parametric amplifier. Figure adapted from [73]. 15
2.5 Parametric gain calculated for LWIR generation in 1 mm GaSe. 16

2.6 Parametric output for LWIR parametric generation in 2 mm GaSe. 16
2.7 Schematic representation of optical parametric chirped pulse amplification, starting from a Fourier limited pulse through chirp before parametric amplification and recompression. 17

3.1 Figure of merit, ratio between effective nonlinearity d and refractive index n, directly relating to the conversion efficiency for non-oxide birefringent crystals in the infrared region, modified Figure taken from [82]. Crystal abbreviations: Tellurium (Te), Cadmium Germanium Arsenide ($CdGeAs_2$, CGA), Selenium (Se), Cadmium Silicon Phosphide (CSP, $CdSiP_2$), Zinc Germanium Phosphide ($ZnGeP_2$, ZGP), Gallium Selenide (GaSe), Mercury Thiogallate ($HgGa_2S_4$, HGS), Lithium Gallium Tellurite ($LiGaTe_2$, LGT), Silver Gallium Selenide ($AgGaSe_2$, AGSe). 25
3.2 Transparency range of nonlinear crystals covering the target MWIR and LWIR spectrum (grey bar): BBO, beta barium borate (BaB_2O_4); KTA, potassium titanyle arsenate ($KTiOAsO_4$); CSP, cadmium silicon phosphide ($CdSiP_2$); AGS silver gallium sulfide ($AgGaS_2$); ZGP, zinc germanium phosphide ($ZnGeP_2$); BGS, barium gallium sulfide ($BaGa_4S_7$); BGGS, barium gallium germanium sulfide ($BaGa_2GeS_6$); AGSe, silver gallium selenide ($AgGaSe_2$); BGSe, barium gallium selenide ($BaGa_4Se_7$); BGGSe, barium gallium germanium selenide ($BaGa_2GeSe_6$); GaSe, gallium selenide. Wavelength of the pump (green dotted line), and the signal seed (black dotted line) (from the Cr:ZnS oscillator). . . . 26
3.3 Phase matching angles (internal) for a 2.05 µm pump in (a) $ZnGeP_2$, pump in (o) and (b) GaSe, pump in (e) for type I and type II. The lighter line indicates the signal, the darker line the idler. 28
3.4 Non-collinear phase matching in $ZnGeP_2$ for MWIR and GaSe for LWIR for different non-collinear angles and a 2.05 µm pump. 28
3.5 GVM for a 1.03 µm pump in GaSe at 14.1° with $\nu_s(1.12\,\mu m) = -68$ fs/mm and $\nu_i(11.5\,\mu m) = -638$ fs/mm, indicated by grey vertical lines. 30
3.6 GVM for a 2.05 µm pump in GaSe at 12.2° with $\nu_s(2.4\,\mu m) = 12$ fs/mm and $\nu_i(11.5\,\mu m) = -28$ fs/mm, indicated by grey vertical lines. 30
3.7 GVM for a 2.05 µm pump in $ZnGeP_2$ at 58.5° with $\nu_s(3.2\,\mu m) = -58$ fs/mm and $\nu_i(5.4\,\mu m) = -112$ fs/mm, indicated by grey vertical lines. 30
3.8 Comparison of parametric coefficient with (solid line) and without (dashed line) group velocity consideration for 2 mm thick GaSe (type II) and $ZnGeP_2$ (type I). 31
3.9 Conversion efficiency for type I phase matching in 2 mm GaSe for different phase matching angles (pump at 2.05 µm). 31
3.10 Efficiency of idler generation in GaSe for specific phase matching angle with 2.05 µm pump depending on the crystal thickness. (a) and (b) type I, (c) type II phase matching. 32
3.11 Conversion efficiency and bandwidth in 2 mm thick nonlinear crystal. Type II phase matching in GaSe at $\theta = 12.17°$ and BGSe at $\theta = 5.0°$ and $\phi = 90°$. . . . 33
3.12 Group velocity dispersion (GVD) and third-order dispersion (TOD) values for typical infrared materials transparent beyond 2 µm. 35

3.13 Signal Parametric Gain in GaSe for 12.17° in type II PM, pump at 2.05 µm with $d_{\text{eff}} = 53.7\,\text{pm/V}$. 39
3.14 Idler Parametric Gain in GaSe for 12.17° in type II PM, pump at 2.05 µm with $d_{\text{eff}} = 53.7\,\text{pm/V}$. 39
3.15 Signal Parametric Gain in GaSe for 14.1° in type II PM, pump at 1.03 µm with $d_{\text{eff}} = 56.2\,\text{pm/V}$. 39
3.16 Idler Parametric Gain in GaSe for 14.1° in type II PM, pump at 1.03 µm with $d_{\text{eff}} = 56.2\,\text{pm/V}$. Legend of Fig. 3.15 applies. 39
3.17 Parametric coefficient for type II phase matching in 2 mm GaSe at 12.17°. . . . 40
3.18 Parametric coefficient for type II phase matching in 2 mm GaSe at 12.29°. . . . 40
3.19 Direct comparison of type II phase matching in GaSe for the pump wavelength at 2.05 µm at 12.17° and 2.25 µm at 12.29°. This graph is the horizontal cross section of Fig. 3.17 and 3.18. 40
3.20 The Simulation results of the LWIR OPCPA: high gain (a,b,d) in 2 mm GaSe with $E_p = 321\,\mu\text{J}$, seeded with $E_s = 1\,\text{nJ}$ and (c) low gain amplification in 1 mm GaSe with $E_p = 1.6\,\text{mJ}$, seeded with $E_s = 15\,\mu\text{J}$. (a,c) output bandwidth in percent from input bandwidth and conversion efficiency in dependence of the temporal signal to pump ratio τ_s/τ_p, and corresponding signal (b) and idler (d) spectrum for two τ_s/τ_p values. 41
3.21 Simulation results of MWIR OPCPA: (a) in 2 mm $ZnGeP_2$ with 325 µJ pump energy, seeded with 2.5 nJ signal showing bandwidth and conversion efficiency in dependence of the temporal signal to pump ratio τ_s/τ_p, and (b) corresponding signal spectrum. 41
3.22 Simulation with Sisyfos of two stage GaSe ($d_{\text{eff}} = 30\,\text{pm/V}$) OPCPA for LWIR generation in 2 mm in OPA 1 ((a)(b),(e)(f)), and using the depleted pump in OPA 2 with 1 mm GaSe ((c)(d),(g)(h)), pump at 2.05 µm and signal at 2.4 µm. Upper part: with 2nd order Gaussian beam profile, lower part: with 10th order. Left column: temporal profile, right column: spatial profile. 44

4.1 Simulation of the Ho:YLF regenerative amplifier showing (a) the exponentially amplified pulse energy reaching depletion after 19 round-trips, (b) the gain evolution until complete population depletion, (c) the seed and the output spectrum of the amplified pulses and (d) the bandwidth reduction due to gain narrowing as a dependence of the number of round-trips. 51
4.2 Scheme of the regenerative amplifier (RA) setup including the front-end with the fs Cr:ZnS oscillator and the dichroic mirror (DM), the stretching in chirped volume Bragg gratings (CVBG) to ≈ 1 ns and pre-amplification in a thulium doped fibre amplifier. The RA comprises the gain crystal Ho:YLF being pumped by a CW Tm:fibre laser at 1940 nm, the Pockels cell (PC) and the thin-film polarisers (TFP) as in- and output ports. It follows a Treacy-type grating compressor to compensate for the residual chirp of the amplified pulses before taken for the parametric stages of the OPCPA. 52

4.3 Spectra related to the regenerative amplifier with (a) the seed from the fs Cr:ZnS oscillator spectrum split at 2.1 µm and the CVBG selecting the amplified spectrum (green box), (b) the output of the Tm:fibre pre-amplifier (light green) with 2.5 nJ energy serving as the seed and the output spectrum of the RA after amplification and gain narrowing at 2051 nm (dark green and black Gaussian fit). 53
4.4 Autocorrelation measurement of the amplified pulses after compression with sech^2 fit and pulse duration of 2.4 ps (Fourier limit 2.3 ps). 53
4.5 Long-term energy stability measurement after compression. Inset: far-field intensity distribution. 53
4.6 Autocorrelation measurement of RA pulses with intracavity shaping using a BaF_2 etalon after compression with sech^2-fit. 54
4.7 Comparison between amplified RA pulses with (black) and without (green) intracavity shaping. Simulation with etalon shaping in blue. 54

5.1 Absorption cross section of Cr:ZnS and Cr:ZnSe and emission lines of potential pump sources, taken from [53] (Fig. 3). 56
5.2 Emission cross section of Cr:ZnS and Cr:ZnSe and atmospheric vapour absorption cross section, taken from [53] (Fig. 4). 56
5.3 Front-end architecture based on a Cr:ZnS oscillator for MWIR and LWIR OPCPA. Mirror (1) can be flipped to select the LWIR or MWIR signal pulses. 57
5.4 Front-end architecture based on a Er:fibre oscillator of MWIR OPCPA adapted from [41], generating a fixed signal at 3.4 µm. 57
5.5 Spectrum of Cr:ZnS master oscillator with 350 nm FWHM bandwidth. 58
5.6 Autocorrelation trace of Cr:ZnS oscillator pulses (miniTPA, APE) and fit. . . . 58
5.7 Front-end architecture comprising the master oscillator, a $\lambda/2$ waveplate and a dichroic mirror (DM). 58
5.8 Long-term power stability of Cr:ZnS master oscillator behind dichroic mirror. Total output power is 1.06 W, corresponding to 12 nJ pulse energy. 58
5.9 Spectrum of signal seed pulses for LWIR OPCPA beyond 2.1 µm. 59
5.10 Autocorrelation trace of signal seed pulses for LWIR OPCPA - recorded with TPA mini AC (APE) - and sech^2 fit. 59
5.11 Calculated group velocity dispersion (GVD) for a 6.5 µm core ZBLAN fibre with a zero-dispersion wavelength (ZDW) at 1.99 µm. Vertical dashed line: laser central wavelength. 61
5.12 Spectrum of Raman self-frequency shifted solitons for different launched pulse energies behind 60 cm long ZBLAN fibre. 62
5.13 Measured self-frequency shifted solitons (solid lines) for different launched pulse energies behind 2 m long ZBLAN fibre and simulated soliton spectra (dashed lines) with *fiberdesk*. The spectral width (FWHM) has been fitted with a hyperbolic secant shape to the data. 62
5.14 Spectral and temporal characterisation of the self-frequency shifted soliton with 1.4 nJ at 2.99 µm behind the 2 m long ZBLAN fibre. 63

5.15 Lower graph (b): Simulated spectral evolution of soliton in 2 m long ZBLAN fibre using the nonlinear Schrödinger equation (eq. 2.44). Upper graph (a) measured spectrum for 3.2 µm soliton and simulation at 2 m. 64
5.16 Lower graph (b): simulated temporal evolution of soliton in 2 m long ZBLAN fibre using the nonlinear Schrödinger equation (eq. 2.44), upper graph (a) temporal intensity distribution at 2 m. 64
5.17 Stability measurement of 3.25 µm soliton behind the 2 m ZBLAN fibre. 65
5.18 (a) Comparison and evolution of the measured frequency shift of solitons for different energies in the 2 m and 60 cm fibre. (b) How energy instability transfers to frequency jitter under assumption of linear energy-frequency dependency. . 67

6.1 MWIR OPCPA setup with an idler output energy of >0.4 mJ tunable between 5.4 and 6.8 µm and sub-150 fs pulse duration. The setup includes the front-end with the Cr:ZnS oscillator and the soliton shifting ZBLAN fibre, the 2.05 µm Ho:YLF regenerative amplifier (RA) as the pump and two optical parametric amplification (OPA) stages. DM: dichroic mirror, S: stretcher, C: compressor. . 70
6.2 Simulation of 2-stage OPA using *Sisyfos* pumped at 2.05 µm based on ZGP for implemented configuration for the different signal wavelengths. 71
6.3 Simulated spectrum for 2-stage OPA pumped at 2.05 µm based on ZGP for the 2.9 µm and 3.2 µm signal. The simulation confirms that the entire seed spectrum is amplified without showing any signs of gain narrowing for all input seed wavelengths. 72
6.4 Measured spectrum of signal and idler pulses, color code transfers between signal and corresponding idler. The signal is tuned between 3.0 µm and 3.3 µm which translates into an idler covering 5.4 µm to 6.8 µm. The atmospheric absorption (transmission through 10 cm air) is shown by the black line, explaining the structured idler spectrum. 73
6.5 Autocorrelation measurement of amplified signal behind 2nd OPA stage at 3.0 µm, uncompressed, recorded with mini TPA (APE). 74
6.6 Autocorrelation measurement of idler pulses behind 2nd OPA stage at 5.4 µm, in ambient condition (RH: 40 %) after compression in a CaF_2 prism pair, recorded with Pyrocam. 74
6.7 Two stage OPCPA setup based on ZGP including the AOPDF (Dazzler, Fastlite) for precise phase shaping and idler output purged with nitrogen. DM: dichroic mirror, S: stretcher, C: CaF_2 compressor. 75
6.8 Measured spectrum of tunable idler pulse in nitrogen purged surrounding with the possibility of phase pre-shaping with Dazzler. In analogy to Fig. 6.4. 76
6.9 Characterization of idler pulses with home-built FROG setup, based on $AgGaS_2$ and recorded with monochromator (Horiba): (a) Measured and, (b) retrieved FROG trace, (c) retrieved pulse and phase in temporal domain, (d) retrieved pulse and phase in spectral domain, and measured spectrum (with APE wavescan) with grey background. The structure of the spectrum is not real and can be attributed to the repetition rate on the rotating grating inside the spectrometer. 77

6.10 Long-term energy measurement for idler at 5.4 µm behind OPA 2 with root-mean-square stability of 2.1 %. Inset: Idler intensity profile, recorded with Pyrocam. 77

7.1 Overview of the most relevant publications on femtosecond, µJ laser systems beyond 10 µm listing the central wavelength λ, the pulse duration τ, the pulse energy E, the peak power P_p, the repetition rate f, the nonlinear crystal, the process for generating the pulses and the type of driver front-end. 80

7.2 Setup of LWIR OPCPA comprising the front-end with the fs Cr:ZnS oscillator, a phase shaper (AOPDF) for the signal pre-shaping, the pump based on a regenerative amplifier and three OPA stages with the nonlinear crystal GaSe. 81

7.3 Measurement of idler energy behind 2nd OPA stage in dependence of the crystal angles, tuning over type I and type II phase matching. 82

7.4 Measurement of the signal spectrum behind the 1st stage with GaSe for different output energies. 83

7.5 Signal spectrum of first, second and third OPCPA stages, all seeded with the signal pulse. 83

7.6 Signal spectra of LWIR OPCPA for the seed, the first and second OPA stage and parametric coefficient for type II phase matching at 12.2° in 2 mm GaSe (gray shaded area). 84

7.7 The corresponding idler spectra of the LWIR OPCPA behind the second and third stage. Both measured curves are in good agreement to the simulation (dashed line). 84

7.8 Autocorrelation of signal behind OPA 2 after compression in a Martinez compressor, recorded with the miniTPA (APE). The pulse duration is 121 fs ($\tau_{\mathrm{FTL}} = 115$ fs). 85

7.9 Autocorrelation of idler pulses behind OPA 3 after compression in bulk ZnSe showing a pulse duration of 185 fs ($\tau_{\mathrm{FTL}} = 170$ fs) in home-built autocorrelator. 85

7.10 Measured and retrieved FROG traces for LWIR idler pulses at 11.4 µm behind OPA 3. (a) Measured trace, (b) retrieved trace with 0.4 % error, (c) temporal retrieval of 185 fs pulse duration ($\tau_{\mathrm{FTL}} = 170$ fs) and (d) spectral retrieval matching the measured spectrum (grey area). 86

7.11 Long-term pulse stability of idler pulses behind OPA 3. Inset: far-field intensity distribution. 86

7.12 Simulation with best experimental agreement of three stage LWIR OPCPA based on GaSe with $d_{\mathrm{eff}} = 30$ pm/V, pumped at 2.05 µm with 50 GW/cm^2 and seeded at 2.4 µm. 1st stage with 2 mm GaSe and 2nd stage with 1 mm GaSe, both seeded with the signal, 3rd stage with 1 mm GaSe seeded with the idler. . 87

8.1 Librational L2 mode of a water molecule. 89

8.2 Absorption of different rotational bands in liquid water, including libration, OH-bending and OH-stretching modes and typical decay times. Modified figure taken from [154] (Fig. 1). 90

8.3 Setup of nonlinear transmission measurement of a 12 µm thick water sample between two 1 mm thick BaF_2 windows, irradiated with 200 fs long pulses at 11.4 µm. The ZnSe plate compresses the pulses, in addition to the dispersion of the BaF_2 polariser necessary for energy adjustment and the 50 mm ZnSe lens to reach a beam waist of 150 µm inside the water sample. Two ZnSe lenses project the transmitted light onto a Pyrocam (Spiricon) or spectrometer (Horiba). . . 90

8.4 Normalized incident (green curve) and transmitted (purple curve) spectrum of LWIR pulses centred at 11.4 µm behind 12 µm thick water sample. Absorbance [155] of the librational band (shown in black) defined as $-\log_{10}(T) = \epsilon_0 cd$, where ϵ_0 the linear molar absorptivity, $c = 55\,\text{mol/l}$ the concentration of water and $d = 12 \times 10^{-4}\,\text{cm}$ the sample thickness. 91

8.5 Experimental results of nonlinear transmission measurement of 12 µm thick water cell, irradiated with 200 fs LWIR pulses centred at 11.4 µm. 92

8.6 Stationary limit for population inversion and absorption as a function of the light field intensity. 93

8.7 Time dependent population inversion for 200 fs pulse at different peak intensities and $\tau = 100\,\text{fs}$ lifetime of the libration state. Excitation pulse profile shown by dashed line. 93

8.8 Surface irradiated by light pulse is divided into rings of thickness d_r. 93

8.9 Transmission calculated from non-stationary solution of two-level quantum system for different vibrational upper state lifetime τ, calculated for 150 µm spot size, 12 µm sample thickness and 200 fs pulse duration, in dependence of input energy. Absorption coefficient α defined as $T = e^{-\alpha d}$. 95

8.10 Experimental results of LWIR transmission measurement of 12 µm water sample with a transmission change of 1.4 % between 2 and 27 µJ. The graph includes a linear fit for the experimental results with $T = 0.08 + 5.6 \times 10^{-3}\,(\mu\text{J})^{-1} E_p$, and the calculated transmission (solution of rate equations presented in sec. 8.2) is drawn with an y-offset of 0.55 % for a lifetime of 10 and 20 fs. 96

1

Introduction

Since the advent of the laser in 1960 [1, 2], the variety of laser systems has been developing and their specifications have been determined by the requirements of the high number of scientific, medical and industrial applications. Nowadays, telecommunication relies on semiconductor and fibre lasers at 1.5 µm wavelength [3], eyes are corrected with femtosecond infrared pulses [4], Quantum Cascade Lasers (QCL) are used for food analysis [5] and biomedical diagnostics [6, 7]. In fundamental research and physics, hot atoms are cooled and stored with narrow-linewidth lasers for potential quantum technology [8, 9], atomic ensembles are trapped in optical lattices [10], frequency combs enhance the precision in metrology [11] and ultrafast processes can be studied via pump-probe spectroscopy [12–14].

Lasers work in continuous wave or pulsed mode, and cover a large part of the electromagnetic spectrum. They exist in the ultraviolet (UV) region between 150 nm and 380 nm, in the visible (VIS) region between 380 nm and 780 nm, followed by the near-infrared (NIR) between 800 and 1060 nm, the short-wave infrared (SWIR) between 1.5 and 3 µm, the mid-wave infrared (MWIR) between 3 and 8 µm, and the long-wave infrared (LWIR) between 8 and 16 µm. In an experiment, the wavelength, repetition rate and pulse duration determine the spatial and temporal resolution limit. Fig. 1.1 summarizes different lasers for the infrared region. In the NIR spectral region, active materials based on the rare earth ions Ti^{3+}, Nd^{3+}, Yb^{3+} are well established and used in a wide range of scientific applications. At 2 µm wavelength, Ho^{3+} and Tm^{3+} doped crystals and fibres are commonly used in lasers and amplifiers. Beyond such laser materials, crystals doped with Cr^{2+} ions are very promising since they can be pumped with commercially available fibre lasers and emit broadly in the infrared region around 2.4 µm. Fe^{2+} lasers, in contrast, lack suitable pump sources. Beyond that, QCLs cover a wide spectral range between 5 and 20 µm and the terahertz range but come at limited average power and long pulse durations [15]. Gas lasers use the vibrational and rotational transitions of molecules to extend the wavelength range well beyond 10 µm. In industry, CO_2 lasers [16] are widely used for cutting and welding as they emit high average power [17]. However, reaching the femtosecond pulse regime with this laser type requires sophisticated post compression schemes [18]. Lately, the popularity of multipass-cells has tremendously increased in order

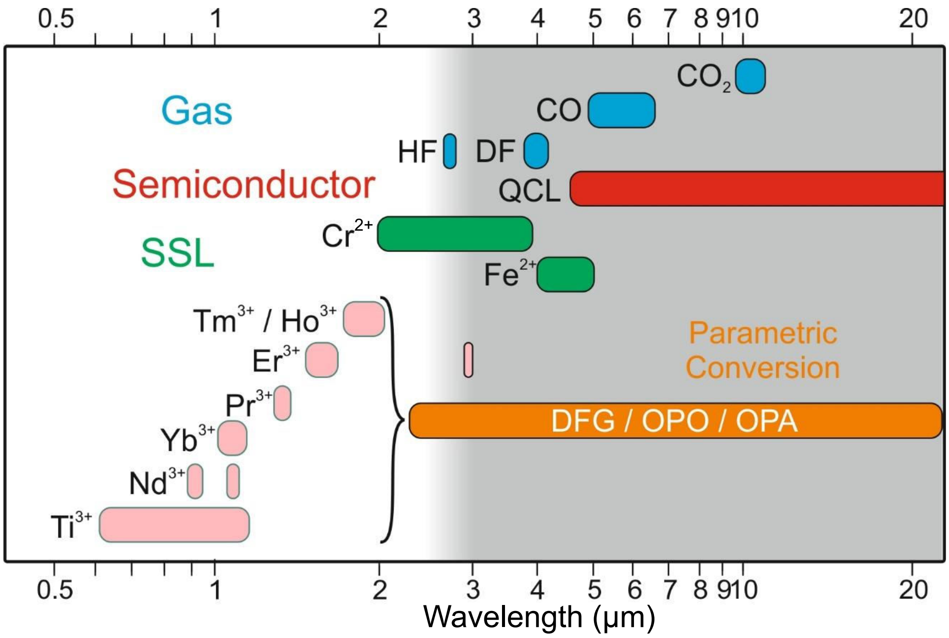

Figure 1.1: Overview of laser sources, typically used for accessing the infrared spectral range directly or via parametric interaction by providing the seed spectra. Shown laser types: solid state lasers (SSL), semiconductor lasers in the infrared (Quantum Cascade Lasers (QCL)), and gas lasers relying on various gas mixtures (adapted from [25] Fig. 1.6).

to reach femtosecond pulse durations by additional spectral broadening and simultaneous temporal compression of picosecond sources [19, 20].

Driving nonlinear processes with high efficiency requires peak intensities of 10^{11} W/cm^2 to 10^{18} W/cm^2, reachable with femtosecond laser pulses in the µJ to mJ energy range. Fig. 1.1 shows the lack of solid state gain materials beyond 4 µm which can be pumped with commercially available solid-state or fibre lasers. Pulses of a femtosecond duration in this spectral region are only producible via difference frequency generation (DFG), in optical parametric oscillators (OPO) or optical parametric amplifiers (OPA). Tunable OPO and OPA systems offer easy adoption to custom applications, but typically generate rather low energy pulses [21–23].

In recent years, enormous effort was put into the development of femtosecond mid-wave infrared lasers. In the region between 2.5 and 20 µm lies a rich set of molecular vibrational absorption lines, also referred to as the *fingerprint region*. Spectroscopy in this wavelength range allows to probe vibrational and/or rotational transitions of chemical bonds or functional groups directly [24].

The development of mid-IR laser sources is also triggered by potential applications in strong-field physics. Structures and dynamics of materials can be studied with enhanced temporal and spatial resolution when using ultrashort extreme ultraviolet (EUV) or x-ray sources. The typically limited beam time at large scale facilities providing hard and soft x-rays from a free electron laser demands for table-top solutions. High-energy femtosecond lasers with intensities $> 10^{15}$ W/cm^2 focussed into various targets produce photons of energies from several electronvolts to the keV range through highly nonlinear processes. In high pressure gases, high harmonic generation produces coherent pulses from the vacuum ultraviolet to soft x-ray regime with attosecond pulse duration [26–28]. Here, the highest accessible photon energy scales with the wavelength (and the gas type), but at the same time results in lower efficiency. On metal targets, incoherent hard x-rays can be generated with high brightness [14, 29, 30]. Mid-IR sources beyond 2.2 µm lead to an improved x-ray flux compared to near-IR driver sources, as the ponderomotive potential of electrons scales with λ^2 [29]. Few-cycle laser systems in the kHz-regime operating at 3.9 µm [30] and 5 µm [14] have opened up new potential for x-ray diffraction experiments providing a spatial resolution of the order of 0.1 nm.

Accessing the mid-IR spectral region via OPCPA

The generation of new frequency components via parametric processes relies on the nonlinear interaction and energy exchange between two laser pulses in a nonlinear medium. Combining the advantages of chirped pulse amplification (CPA), demonstrated by D. Strickland and G. Mourou in 1985 [31], with optical parametric amplification (OPA), see Fig. 1.2, it is possible to generate laser pulses with TW peak powers and kW average powers, supporting few-cycle to femtosecond pulse durations. Parametric amplification creates a new idler frequency from a strong narrowband pump and a weak broadband signal under energy and momentum conservation. After pioneering theoretical and experimental work of A. Piskarskas [32], the first successful implementation of optical parametric chirped pulse amplification (OPCPA) was demonstrated by A. Dubietis in 1992 [33] and is since then evolving continuously. OPCPA enables the generation of pulses in spectral regions not accessible with direct laser transitions and because of their potential of surpassing the performance of current femtosecond laser systems, they are also referred to as *Third Generation Femtosecond Technology* [34].

OPCPA offers a flexible design and enables customized pulse durations, repetition rates and target wavelengths but comes at the expense of complex front-end architecture [35, 36]. Efficient parametric amplification requires a nonlinear crystal with high effective nonlinearity, high damage threshold and a broad phase matching bandwidth [37]. When correctly designed, the OPCPA energy stability can be superior to the stability of the pump source [38]. If the pump and the signal pulses are stemming from the same seed pulse, the carrier envelope phase (CEP) of the generated idler pulses is inherently stable.

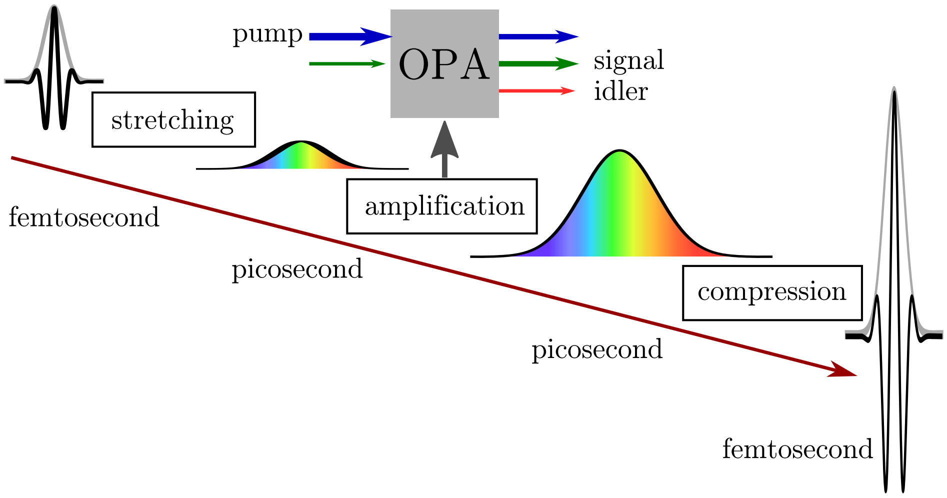

Figure 1.2: Schematic representation of optical parametric chirped pulse amplification (OPCPA). The signal seed is stretched from femtosecond to picosecond pulse duration prior to the optical parametric amplification process, where the signal is amplified and a third idler beam is created. Subsequent compression of the signal and/or idler pulses leads to pulse ultrashort durations.

The accessible spectral region via OPCPA has grown with the improvement of suitable pump sources and nonlinear crystals over the years from the NIR to the LWIR region [39], see Fig. 1.3. The generation of femtosecond pulse durations requires seed pulses with a sufficiently broad spectral width and a nonlinear crystal providing broadband phase matching conditions. High energy pump sources are necessary to generate pulses in the µJ to mJ range. Yb^{3+}, Er^{3+} and Nd^{3+} based driver sources around 1 µm as well as Ti^{3+}:Sa lasers at 800 nm are commonly used in OPCPA architectures. These systems generally rely on multiple nonlinear stages such as supercontinuum (SC) generation, difference frequency generation (DFG) or optical parametric generation (OPG) to provide the required seed wavelengths [28, 40, 41].
Due to the properties of the available nonlinear crystals, efficient parametric generation beyond 4 µm using near-IR pump sources has been limited to the µJ energy level [37] because of unfavourable phase matching properties, low damage threshold of the nonlinear crystals and the intrinsic pump/signal to idler photon energy relation. This can be seen in Fig. 1.3, where all OPCPA systems beyond 4 µm rely on 2 µm pump sources.
The number of systems in the mid-infrared spectral region between 3 and 9 µm is fairly limited. In 2011, the first MIR source has reached the multi-millijoule regime with few-cycle pulses at a repetition rate of 20 Hz [29, 42]. This system emits pulses at 3.9 µm with a pulse energy exceeding 8 mJ with a pulse duration of 83 fs in the gain crystal KTA. The most powerful system generates idler pulses at 5 µm at 1 kHz repetition rate in ZGP with a Ho:YLF regenerative amplifier at 2 µm as the pump [41]. The best performance at 2 µm has reached 3.4 mJ energy compressed to 89 fs pulse duration corresponding to 33 GW peak power [43]. The group of J. Biegert has, for the first time in 2016, generated laser pulses at 7 µm wavelength with a repetition rate of 100 Hz in ZGP, with a pump at 2052 nm amplified in a Ho:YLF regenerative amplifier [44]. After initially reaching a pulse energy of 200 µJ, they increased the output energy to 0.75 mJ three year later with a pulse duration of 185 fs [40]. There are two OPCPA systems emitting pulses at 9 µm amplified in the nonlinear crystal $LiGaS_2$ (LGS) and pumped with a Yb:YAG laser at 1030 nm [45, 46]. The first system generates pulses with a duration of 142 fs at 10 kHz repetition rate. The second is tunable between 4 and 11 µm having the maximum output energy at 9 µm with 2.2 µJ energy at 200 kHz repetition rate supporting a Fourier limit of 50 fs.

The efficiency for the generation of pulses in the LWIR spectral region via parametric amplification is much lower due to the even more unfavourable signal to idler energy ratio. Systems relying on parametric processes aiming for the wavelength region beyond 10 µm with µJ energy level and fs pulse duration rely typically on a near-IR driver source [47–50]. For almost 20 years, the energy record was set to 1.4 µJ via DFG. Only very recently, this energy limitation has been overcome, setting the new record to 10 µJ at kHz repetition rate [23, 51] but come along with rather complicates architectures.

OPCPA components

The two nonlinear crystals $ZnGeP_2$ (ZGP) and GaSe offer high nonlinear coefficients of 78 pm/V and 56 pm/V, and adequate phase matching conditions in the mid-infrared spectral range when pumped at 2 µm. ZGP has a short wavelength absorption edge which prohibits pump sources below 2.0 µm. Also, the damage threshold of GaSe at 2 µm is much higher

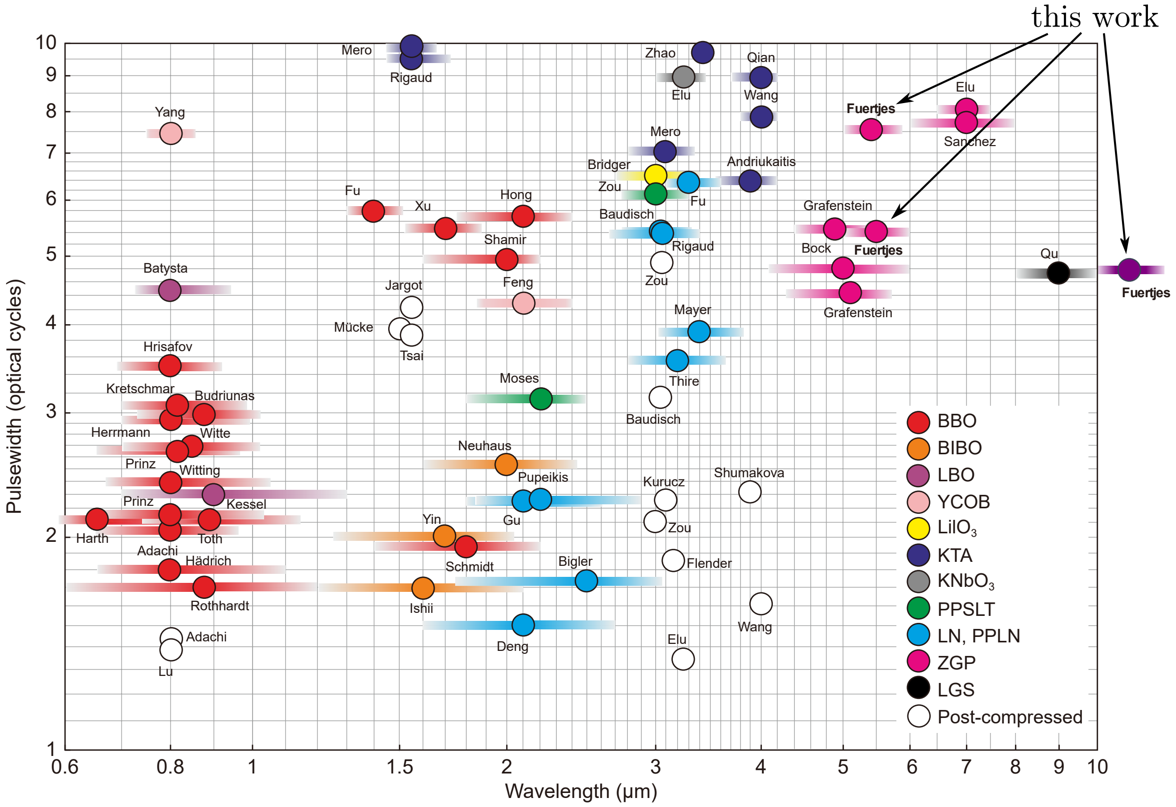

Figure 1.3: State of the art of few optical cycle table-top OPCPA systems, showing the high number of systems between 0.8 and 4 µm system. The longer the wavelength the more sophisticated is the system architecture and the lower is the output power. Beyond a wavelength of 4 µm, all systems rely on $ZnGeP_2$ (ZGP) or $LiGaS_2$ (LGS), and the number is fairly limited. Figure adapted from [39], see paper for detailed references. Please find the abbreviations of the crystals in Appendix A.

than at 1 µm since there is much more pronounced nonlinear absorption coefficient caused by two-photon absorption near half the bandgap energy at 2.1 eV. Using 2 µm pump sources is additionally advantageous to reach the mid-IR spectral region because of the intrinsic energy relation between pump and signal wavelength in parametric processes [37, 52].

For stable operation, the pump and signal pulse either need to be actively synchronized or stem from the same source. Laser front-ends with broad spectra that simultaneously seed the pump and the signal are therefore advantageous. If the same pump and signal pulse are combined in the parametric process, the idler output is inherently CEP-stable.
Cr^{2+} doped zinc sulphide (Cr:ZnS) allows for pumping with NIR fibre lasers and display a broad emission spectrum [53, 54]. This type of laser is referred to as the *Titanium Sapphire of the mid-infrared* as it has a similarly broadband spectrum enabling femtosecond pulse durations at high energies. The emission spectrum spanning over an octave, being mainly limited by atmospheric absorption towards longer and shorter wavelengths, has enabled single cycle pulse durations of 9 fs centred at 2.4 µm [55]. Cr:ZnS oscillators have very recently become commercially available and open up a new horizon for infrared applications [56–58].

Objectives and outline of this thesis

This thesis aims to create novel powerful few-cycle sources in the infrared spectral regions via OPCPA. It strives to overcome the current limitations with pulse energies exceeding 100 µJ at a wavelength beyond 4 µm and at a 1 kHz repetition rate. A very simple front-end based on a Cr:ZnS oscillator is explored as an alternative to the well-established near-IR front-ends for a MWIR and LWIR OPCPA. The stability of a regenerative amplifier at 2 µm seeded with the new front-end is evaluated in the stable regime. The architecture necessary to reach the boundaries of energy scaling towards longer wavelengths is analysed. The potential for ultrafast nonlinear spectroscopy is demonstrated by the first nonlinear transmission study in the range of the librational L2 band of water.

Chapter 2 introduces the relevant theoretical background for generating femtosecond pulses in the MWIR and LWIR region at the µJ to mJ-energy level. The design considerations for an OPCPA system are presented in chapter 3. The performance and the underlying physical equations for the Ho:YLF regenerative amplifier used as the driver are described in chapter 4. The novel front-end based on a Cr:ZnS oscillator is presented in Chapter 5. Next, the implementation and the output characteristics of the OPCPA system in the MWIR and LWIR spectral region are presented in chapter 6 and 7, respectively. Finally, a nonlinear transmission measurement on liquid water using the µJ-energy pulses beyond 10 µm are presented in chapter 8. The summary and outlook can be found in chapter 9.

2

Theoretical background

In the 19th century, James C. Maxwell unified electric and magnetic phenomena in a set of coupled partial differential equations [59]. From these equations, it is possible to derive equations that describe the propagation of light in a dispersive medium. While Maxwell has focussed on the limit of linear light-matter-interaction, the formalism has been extended to describe nonlinear optical phenomena.
In the following, this chapter aims to outline the difference between linear and nonlinear phenomena and to provide an explanation of the coupling between light waves. This is necessary in order to understand the principles of parametric amplification being the main topic of this thesis. The slowly varying envelope approximation (SVEA) is applied which fails for pulse durations approaching the few-cycle regime but is valid for longer pulses. The presented description follows the standard textbooks [60–62]. In order to include the nonlinearity of media playing an significant role in the context of (ultra-)short pulses in fibres, the Nonlinear Schrödinger Equation (NLSE) is explained [63].

2.1 Pulses in dielectric media

From Maxwell's equations, the wave equation describing the light propagation in a charge free and non-magnetic medium can be written in terms of the macroscopic polarization $\vec{P}$ resulting from the electric field $\vec{E}$

$$\nabla^2 \vec{E}(\vec{r},t) - \frac{1}{c_0^2}\frac{\partial^2}{\partial t^2}\vec{E}(\vec{r},t) = \mu_0 \frac{\partial^2}{\partial t^2}\vec{P}(\vec{r},t), \tag{2.1}$$

where $c_0 = \sqrt{1/(\epsilon_0 \mu_0)}$ is the vacuum speed of light expressed in terms of the vacuum dielectric ϵ_0 and the magnetic permittivity μ_0. The general solution of this equation is a plane monochromatic wave oscillating with a phase depending on the frequency ω and the wave vector $\vec{k}$

$$\vec{E}(\vec{r},t) = \vec{E}_0 \exp\left(i(\omega t - \vec{k}\cdot\vec{r})\right). \tag{2.2}$$

In general, the E-field is a vector being linearly, circularly or elliptically polarized. For the sake of simplicity, the vector-nature of the solution is omitted and the E-field is assumed to be a scalar quantity. The electric field amplitude of a monochromatic wave can be decomposed into an slowly varying amplitude envelope $A(z,t)$ and an oscillating part with frequency ω, having a wave vector k pointing in the z direction

$$E(z,t) = \mathrm{Re}\left(A(z,t)e^{-i(kz-\omega t)}\right) = \frac{1}{2}A(z,t)e^{-i(kz-\omega t)} + \frac{1}{2}A^*(z,t)e^{i(kz-\omega t)}. \tag{2.3}$$

Correspondingly, the intensity is defined as

$$I(z,t) = \frac{1}{2}\epsilon_0 c_0 n|E(z,t)|^2. \tag{2.4}$$

As a plane wave solves the wave equation 2.1, the sum over plane waves with different frequencies ω is also a solution

$$E_{pulse} = \sum_{\omega} A(\omega)e^{-i(\beta z-\omega t)+i\phi(\omega)},$$

where $A(\omega)$ represents the amplitude of the individual spectral components and $\beta(\omega) = n(\omega)\frac{\omega}{c}$ replaces the wavevector k. Pulses are a coherent superposition of plane waves with a certain phase relation and accordingly, pulses can be written in Fourier space as

$$E(z,t) = \int_{-\infty}^{\infty} E(z,\omega)e^{i(\omega t-kz+\phi)}\,\mathrm{d}\omega \tag{2.5}$$

and inversely as

$$E(z,\omega) = \frac{1}{2\pi}\int_{-\infty}^{\infty} E(z,t)e^{-i(\omega t-kz+\phi)}\,\mathrm{d}t. \tag{2.6}$$

In the slowly varying envelope approximation (SVEA) ${}^{\mathrm{d}^2E}\!/_{\mathrm{d}t^2} \ll \omega_0{}^{\mathrm{d}E}\!/_{\mathrm{d}t}$, the pulse amplitude envelope varies slowly with time t, and one can write the pulse in terms of an envelope $A(z,t)$ and an oscillation with carrier frequency ω_0

$$E(z,t) = \frac{1}{2}\left(A(z,t)e^{-i(k_0 z-\omega_0 t+\phi)} + c.c.\right). \tag{2.7}$$

This mathematical representation of a light pulse allows to study the different effects in dielectric media.

A pulse has its minimum duration when all phases ϕ of all spectral components are equal to zero at a given point in time. In this case, one speaks about a Fourier transform limited (FTL) pulse duration. The Fourier-transform limit depends on the spectral shape and width of the pulse, where we can attribute $\Delta\omega_p\tau_p \geq 2\pi c_B$, where $\Delta\omega_p$ is the spectral width and τ_p the pulse duration. Throughout this thesis, the spectral width is given for the full width half maximum (FWHM). The relations for three relevant pulse shapes are summarized in tab. 2.1.

In the SVEA and for interaction of the E-field with the medium far from medium resonance, one can rewrite the induced polarization in power series of the electric field

$$\begin{aligned}\vec{P} &= \epsilon_0\left(\chi^{(1)}\vec{E} + \chi^{(2)}\vec{E}^2 + \chi^{(3)}\vec{E}^3 + ...\right) &(2.8)\\ &= \epsilon_0\chi\vec{E} + \vec{P}_{NL}, &(2.9)\end{aligned}$$

Shape	Intensity profile I(t)	τ_p (FWHM)	c_B
Gauss	$\exp(-2(t/\tau_G)^2)$	$1.177\tau_G$	0.441
Sech	$\operatorname{sech}^2(t/\tau_S)$	$1.763\tau_S$	0.315
Lorentz	$(1+(t/\tau_L)^2)^{-2}$	$1.287\tau_L$	0.142

Table 2.1: Standard pulse profiles and Fourier transform limit with $\Delta\omega_p\tau_p \geq 2\pi c_B$.

and thereby include the nonlinearity of the medium. The induced polarization can be split into a linear and a nonlinear part attributed to the susceptibility tensor $\chi^{(i)}$ of different orders i.

The value of $\chi^{(1)}$ has the largest value contribution to the polarization. From the definition of the linear term

$$\epsilon_r = n^2 = 1 + \chi^{(1)}(\omega) \tag{2.10}$$

$$n(\omega) = n_{\text{real}}(\omega) + ik(\omega), \tag{2.11}$$

where n_{real} the linear refractive index (simply written as n in the following) and the imaginary part k the linear absorption coefficient.

Close to resonance of the medium, the value of $k = \sqrt{\text{Im}[\chi^{(1)}])}$ becomes large which leads to strong absorption of the dielectric material at certain frequencies. Typically, $\partial n/\partial\omega$ is positive in the visible to infrared region, meaning that blue frequency components experience a larger refractive index than the red components. The refractive index causes refraction and leads to dispersion of a pulse when traversing dielectric media. Most glasses have a refractive index around 1.5 in the visible spectral range. In the infrared range, some materials have much larger refractive indices, as zinc selenide (ZnSe) of 2.4, gallium selenide (GaSe) of 2.7 or silicon (Si) of 3.4 at 5 µm, which leads to large Fresnel losses at uncoated surfaces.

The higher order or nonlinear effects attributed to $\chi^{(2)}$ and $\chi^{(3)}$ become relevant at high peak intensities and are discussed later in this chapter.

2.2 Dispersion

The refractive index of dielectric materials is frequency dependent. Hence, a pulse traversing a dielectric medium experiences dispersion and broadens as the different frequencies accumulate different phases due to the material properties. The phase of a pulse at a center frequency ω_0 can be calculated from the derivative of refractive index at ω_0. The wavevector β can be written as a Taylor expansion of the wave vector at the centre frequency ω_0

$$\beta(\omega) = n(\omega)\frac{\omega}{c} \tag{2.12}$$

$$= \beta(\omega_0) + \frac{\partial\beta}{\partial\omega}\bigg|_{\omega_0}(\omega-\omega_0) + \frac{1}{2!}\frac{\partial^2\beta}{\partial\omega^2}\bigg|_{\omega_0}(\omega-\omega_0)^2 + \frac{1}{3!}\frac{\partial^3\beta}{\partial\omega^3}\bigg|_{\omega_0}(\omega-\omega_0)^3 + \mathcal{O}(\omega^4) \tag{2.13}$$

$$= \beta_0 + (\omega-\omega_0)\beta_1 + \frac{1}{2}(\omega-\omega_0)^2\beta_2 + \frac{1}{6}(\omega-\omega_0)^3\beta_3 + \mathcal{O}(\omega^4) \tag{2.14}$$

where the 0^{th} order term denotes the inverse phase velocity, the first order the inverse group velocity $\beta_1 = \mathrm{d}\beta/\mathrm{d}\omega = 1/v_g$, the second order the group velocity dispersion (GVD) and the third order the dispersion of the group velocity dispersion or the third-order dispersion (TOD). However, not all terms lead to temporal pulse broadening. The phase velocity only changes the phase (constant phase change for all ω) and the group velocity only shifts the pulse in time (linear phase change). Both phase terms do not affect the pulse duration. On the contrary, the dispersive terms GVD and TOD add a specific phase term of second or third order to every individual spectral component, and thus, elongate the pulse. In the context of ultrashort pulses, GVD and TOD control are the prerequisite for Fourier limited pulse durations and the correct phase management becomes essential when using femtosecond pulses.

2.3 Three wave mixing

After dividing eq. 2.8 into a linear and nonlinear polarization part, the largest contribution to the nonlinear polarization and the consequences of the $\chi^{(2)}$ nonlinearity are studied in the following. In general, $\chi^{(2)}_{ijk}(\omega)$ is polarization and frequency dependent and is here assumed to be instantaneous. The lowest order contribution to the nonlinear polarization reads

$$P_i^{nl} = \epsilon_0 \chi^{(2)}_{ijk} E_j E_k, \quad \text{with} \quad i,j,k = x,y,z. \tag{2.15}$$

Considering a plane wave with two frequency components, the nonlinear response associated with the $\chi^{(2)}E^2$ term in eq. 2.8 can be studied when writing the electric field as the composition of two plane waves with amplitude $E_{1,2}$ and frequencies $\omega_{1,2}$

$$E = \frac{1}{2}\left(E_1 \exp(-i\omega_1 t) + E_2 \exp(-i\omega_2 t) + c.c.\right). \tag{2.16}$$

Substituting this into $P = \epsilon_0 \chi^{(2)} E^2$, we find

$$\begin{aligned} P^{(2)}(t) = 2\epsilon_0\chi^{(2)}\Bigg(&\frac{1}{2}E_1^2 e^{-2i\omega_1 t} + \frac{1}{2}E_2^2 e^{-2i\omega_2 t} + c.c. && \text{SHG} \quad (2.17)\\ &+ E_1E_2 e^{-i(\omega_1+\omega_2)t} + c.c. && \text{SFG} \quad (2.18)\\ &+ E_1E_2 e^{-i(\omega_1-\omega_2)t} + c.c. && \text{DFG} \quad (2.19)\\ &+ (E_1E_1^* + E_2E_2^*)\Bigg). && \text{OR} \quad (2.20) \end{aligned}$$

These equations show the creation of new frequency components which are called second harmonic generation (SHG), sum frequency generation (SFG), difference frequency generation (DFG) and optical rectification (OR). These nonlinear processes, depicted in Fig. 2.1, are called second order parametric processes. However, all the above processes are normally very inefficient, as phase matching is the prerequisite to ensure efficient energy exchange.

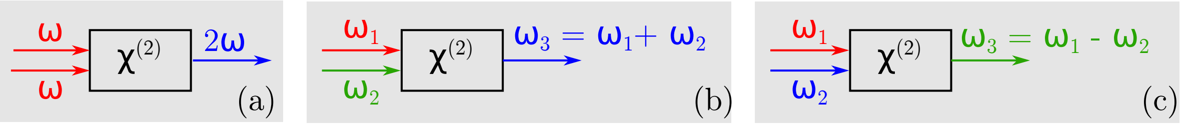

Figure 2.1: Parametric processes: (a) SHG, (b) SFG, (c) DFG

Phase matching is ensured if energy and k-vector are conserved, i.e.

$$\hbar\omega_1 = \hbar\omega_2 + \hbar\omega_3 \tag{2.21}$$

$$\vec{k}_1 = \vec{k}_2 + \vec{k}_3, \tag{2.22}$$

where the index 1 describes the pump, 2 the signal and 3 the idler with $\omega_1 > \omega_2 > \omega_3$. In order to do so, the process needs to fulfil the following conditions

$$\Delta k = \vec{k}_1 - \vec{k}_2 - \vec{k}_3 \tag{2.23}$$

$$\Delta k = \frac{1}{c}(n_1\omega_1 - n_2\omega_2 - n_3(\omega_1 - \omega_2)) = 0. \tag{2.24}$$

These conditions can be fulfilled with two geometries, a collinear and non-collinear phase matching scheme, see Fig. 2.2. Both matching schemes aim for $\Delta k = 0$ and are used for different purposes. In collinear geometry, the pump and the signal propagate in parallel directions and are easy to align. Non-collinear configuration, however, typically allows for a broader phase matching bandwidth as the non-collinear angle provides an additional degree of freedom for fulfilling phase matching. While the seed beam maintains its profile, the newly created pulse profile is spectrally chirped. The spatially and spectrally dispersed beam profile is typically unused and requires a dedicated compression scheme before further use [64]. As visible in Fig. 2.2(b), the angle allows geometrically for a broader spectrum as the different signal and idler pulse components sum to $\Delta k = 0$ at a slightly different angle. Another limiting factor of non-collinear geometry is the finite distance over which the beams overlap spatially.

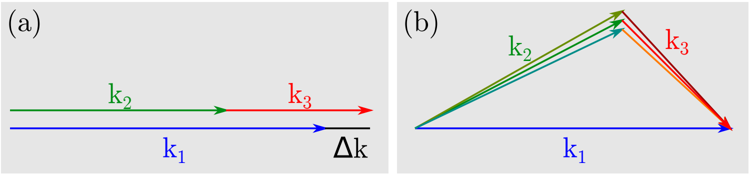

Figure 2.2: (a) Collinear and (b) non-collinear phase matching geometry, where k_1 is the wave vector of the pump, k_2 of the signal and k_3 of the idler. Non-collinear geometry allows typically for a broader bandwidth than collinear geometry.

2.4 Birefringence of uni- and biaxial crystals

Birefringent crystals can be divided into three categories, positive and negative uniaxial and biaxial. The *extraordinary* axis is either larger $n_e > n_o$ (positive) or smaller $n_e < n_o$ (negative) than the other two axes. If n_e is defined to be the z-axis, as shown in Fig. 2.3 (a), the phase matching plane is rotating around the x-axis. The grey area indicates the plane along which the crystal is typically cut. The *ordinary* wave is polarized along the x-axis and experiences $n_x = n_o$. The extraordinary beam has perpendicular polarization ($k_y = 0$) as in the depicted plane. Depending on the phase matching angle θ, the extraordinary wave's refractive index is calculated from the projection onto $\hat{z}$ and $\hat{x}$ according to [65]

$$\frac{1}{n_e^2(\theta)} = \frac{\sin^2\theta}{n_e^2} + \frac{\cos^2\theta}{n_o^2}. \tag{2.25}$$

In a biaxial crystal, all three axes have a different refractive index. The polar coordinates θ and φ describe the normal incident vector of the phase matching plane. In the case of $\varphi = 0°$, the situation is almost the same as in the uniaxial crystal, see Fig. 2.3(b). The ordinary wave is polarized along the y-direction while the extraordinary wave has its projection onto $\hat{z}$ and $\hat{x}$ and eq. 2.25 applies. Similarly, for $\varphi = 90°$, the ordinary wave is polarized along $\hat{x}$, and the extraordinary depends on n_y and n_z and eq. 2.25 applies where $n_y = n_e$ and $n_z = n_o$.

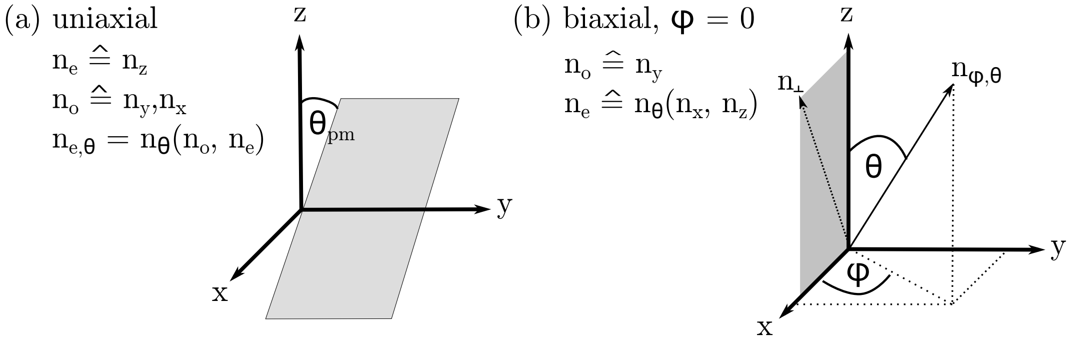
(a) uniaxial
$n_e \triangleq n_z$
$n_o \triangleq n_y, n_x$
$n_{e,\theta} = n_\theta(n_o, n_e)$
z
θ_{pm}
y
x
(b) biaxial, $\varphi = 0$
$n_o \triangleq n_y$
$n_e \triangleq n_\theta(n_x, n_z)$
z
$n_\perp$
$n_{\varphi,\theta}$
θ
y
φ
x

Figure 2.3: Definition of phase matching angle in birefringent crystals: (a) uniaxial crystal where the extraordinary refractive index is along $\hat{z}$, the grey plane is the phase matching plane rotating around $\hat{y}$. (b) biaxial crystal where $n_\perp$ indicates the normal incident vector of the phase matching plane. For $\phi = 0$ the biaxial crystal resembles the uniaxial one with a phase matching plane rotating around $\hat{y}$.

Parametric processes are called type I or type II, depending on the polarization of the involved pulses to achieve $\Delta k = 0$. Type I phase matching is realized if the signal and idler are polarized in the same direction. If the two are orthogonally polarized, the technical term is type II phase matching. One chooses type I or type II phase matching according to the possible refractive index arrangements and momentum and energy conservation. If both types are possible, the decision relies on phase matching bandwidth and effective nonlinearity considerations. Type II phase matching has the drawback of spatial walk-off effects in long crystals along the extraordinary axis, since the wave vector $\vec{k}$ is not parallel to the energy flow $\vec{S}$ [35].

2.5 Parametric Amplification

The creation of new frequency components by exploiting the $\chi^{(2)}$ nonlinearity has been discussed in section 2.3. The right phase matching condition selects the aforementioned processes and the corresponding wavelengths are generated. This technique allows to create frequency components that are not accessible with lasers or gain materials.

In the following section, the analysis is limited to second order effects and omits nonlinear polarization of third order. The second order nonlinear polarization can be written as

$$P_{\mathrm{NL}}(z,t) = \epsilon_0 \chi^{(2)} E^2(z,t) = 2\epsilon_0 d_{\mathrm{eff}} E^2(z,t) \tag{2.26}$$

where d_{eff} is the effective nonlinearity, a scalar value that is derived from the $\chi^{(2)}$ tensor, depending on the polarization of the input field.

Optical parametric amplification (OPA) is a process where a strong pump interacts in a nonlinear material with a small signal wave, amplifies it, and generates in parallel a third wave, namely the idler [35, 66, 67]. In this work, ω_1 is the pump, ω_2 the signal and ω_3 the idler frequency. They relate to each other as $\omega_1 > \omega_2 > \omega_3$, i.e. a pump photon has the largest energy and the idler photon the lowest.

Many textbooks [68–70] have derived the coupled amplitude equations neglecting losses for three monochromatic plane waves to describe the interaction and energy transfer between the light fields

$$\frac{\partial A_1}{\partial z} = i\frac{\omega_1}{n_1 c} d_{\text{eff}} A_3 A_2 e^{-i\Delta k z} \tag{2.27}$$

$$\frac{\partial A_2}{\partial z} = i\frac{\omega_2}{n_2 c} d_{\text{eff}} A_1 A_3^* e^{-i\Delta k z} \tag{2.28}$$

$$\frac{\partial A_3}{\partial z} = i\frac{\omega_3}{n_3 c} d_{\text{eff}} A_1 A_2^* e^{-i\Delta k z}. \tag{2.29}$$

For an absent field of ω_3 prior to interaction, i.e. $I_3(z=0)=0$, and the assumption that the conversion efficiency is small enough that it has a negligible effect on the amplitude A_1, one finds

$$I_3 = \frac{2\mu_0\omega_3^2 L^2}{n_1 n_2 n_3 c_0} d_{\text{eff}}^2 I_1 I_2 \operatorname{sinc}^2\left(\frac{\Delta k L}{2}\right), \tag{2.30}$$

where L is the crystal thickness. The maximum conversion efficiency occurs if $\Delta k = 0$, i.e. perfect phase matching. Otherwise, the output idler intensity scales with $\operatorname{sinc}^2(\Delta k L/2)$.

Under the assumption that the pump is undepleted, i.e. A_1 is constant and $\partial A_1/\partial z = 0$, and there is zero idler input at the beginning of the parametric process, it is possible to combine the two non-zero equations 2.28 and 2.29 to one second-order coupled equation. Then, the idler output can be expressed in terms of the gain coefficient g

$$I_3 = \frac{\omega_3}{\omega_2} I_{20} \sinh^2(gL), \quad \text{where} \tag{2.31}$$

$$g = \sqrt{\Gamma^2 - \left(\frac{\Delta k}{2}\right)^2}, \tag{2.32}$$

$$\Gamma^2 = \frac{2\omega_2\omega_3 d_{\text{eff}}^2}{n_1 n_2 n_3 \epsilon_0 c^3} I_1. \tag{2.33}$$

The gain coefficient reduces with a non-zero Δk. For $\Delta k = 0$ and $\Gamma z \gg 1$, the relation $\sinh^2(x) = 1/4(\exp(2x) - \exp(-2x))$ holds true, and the second term is negligible.

The idler output intensity can be rewritten as an exponential function depending on the small signal gain Γ and the crystal length L,

$$I_3 = \frac{1}{4}\frac{\omega_3}{\omega_2} I_{20} \exp(2\Gamma L). \tag{2.34}$$

According to this equation, the idler intensity grows exponentially with the pump intensity and depends on the ratio between idler and signal. The idler intensity grows linear with the ratio $\omega_{\text{idler}}/\omega_{\text{signal}} = \lambda_{\text{signal}}/\lambda_{\text{idler}}$. To provide an example for mid-wave infrared (MWIR) generation, one could use $E_{\text{pump}}(2.05\,\mu\text{m}) = E_{\text{signal}}(3.2\,\mu\text{m}) + E_{\text{idler}}(5.4\,\mu\text{m})$ with a ratio $3.2/5.4 = 0.59$. In the case of an long-wave infrared (LWIR) idler, $E_{\text{pump}}(2.05\,\mu\text{m}) = E_{\text{signal}}(2.4\,\mu\text{m}) + E_{\text{idler}}(14\,\mu\text{m})$ follows $2.4/14 = 0.17$. As a consequence, the LWIR idler output contains less energy than the MWIR idler output. The energy ratio ω_3/ω_2 following from energy conservation leads to a reduced idler energy, the larger the frequency gap between signal and idler in the parametric process.

The term $G = I_2(L)/I_{20} = 1/4\exp(2\Gamma L)$ is referred to as *parametric gain*. The gain coefficient Γ depends on the signal and idler frequency, the corresponding refractive indices but most importantly squares with the efficient nonlinearity d_{eff} and grows linear with intensity. However, the material constant d_{eff} can vary significantly for different nonlinear crystals. While β-Barium Borate (BBO), typically used for near-infrared (NIR) amplification, exhibits only $d_{\text{eff}} = 2\,\text{pm/V}$, the two infrared materials Zinc Germanium Phosphite (ZGP) and Gallium Selenide (GaSe) exhibit $d_{\text{eff}} = 78\,\text{pm/V}$ and $d_{\text{eff}} = 56\,\text{pm/V}$, respectively. The infrared crystals require much less intensity than the NIR crystal in order to reach the same gain, and typically much thinner crystals can be used, therefore it is advantageous to select a nonlinear crystal with a large effective nonlinearity coefficient.

So far, the analysis was conducted for monochromatic waves, but in practice, laser pulses are often used as they exhibit higher peak powers and offer large bandwidths. Focussed to a few millimetre spot sizes, lasers pulses reach with picosecond duration MW/cm^2 to TW/cm^2 peak intensities which are much more favourable to trigger nonlinear processes.

If speaking about pulses, it is important to mention that Δk in the parametric gain coefficient (eq. 2.33) takes into account the phase matching bandwidth and the group velocity mismatch. Under the assumption of zero phase mismatch in eq. 2.24 for a certain PM crystal angle (see sec. 2.4) and $\Delta\omega_2 = \Delta\omega_1 - \Delta\omega_3$, one finds [62]

$$\Delta k = \left(\frac{\partial k_1}{\partial \omega_1} - \frac{\partial k_2}{\partial \omega_2}\right)\Delta\omega_1 - \left(\frac{\partial k_3}{\partial \omega_3} - \frac{\partial k_2}{\partial \omega_2}\right)\Delta\omega_3, \tag{2.35}$$

where $k_i/\omega_i = (v_{g,i})^{-1}$ are the inverse group velocities, defined in eq. 2.14. As a consequence, if the GVM becomes large, the phase matching bandwidth reduces, as well as the conversion efficiency.

As pulsed systems enable much larger gain coefficients, pump depletion must be considered. The pump is typically a strong but rather narrow bandwidth source, while the signal is weak but broadband. The result of the interaction is the creation of intense broadband pulses supporting up to few-cycle or femtosecond pulse durations. Since the main goal of an OPA system is to maximize the extracted energy, the solution of the coupled amplitude equations (2.27)-(2.29) for a negligible change of the pump amplitude is inapplicable and the equations must be solved numerically.

As depicted in Fig. 2.4, pump depletion occurs in the center of the pulse much faster than at the wings. The central part of the pulse reaches saturation before the wings and starts backconverting. The inhomogeneous depletion of the Gaussian pump profile limits the total conversion efficiency of the system. Flat top profile pumping [71, 72] and the removal of the idler pulse along the parametric process [73] have been proposed to overcome this limitation, and to maximize pump depletion without facing backconversion. In the experiment, saturation and backconversion manifest in the beam intensity profile deviating from the Gaussian distribution and showing a non-Gaussian spectral distribution at the surroundings.

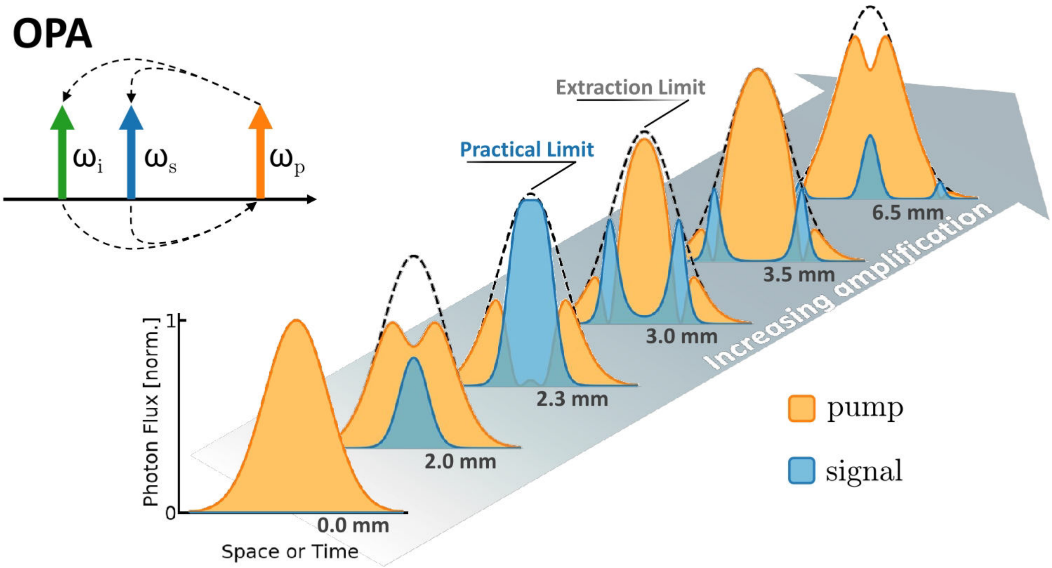

Figure 2.4: Evolution of the pump and signal photon flux with increasing parametric amplification for Gaussian intensity profiles. The central part of the pump pulse is depleted before the signal pulses saturate. The following backconversion process reversing the energy transfer limits the conversion efficiency of an optical parametric amplifier. Figure adapted from [73].

As a consequence, the exponential gain expression in eq. 2.34 for the idler intensity needs to be used with care. The following analysis for picosecond signal and pump pulses shows that the exponential growth is only valid within certain limits. The limits of the analytic solution become visible in Fig. 2.5 where the parametric gain is plotted against the crystal length for different pump intensities. Depending on the pump intensity I_p, the approximation (dotted grey line) only holds true for a specific crystal thickness (or $\Gamma L \gg 1$). The second condition for this analytic solution is an undepleted pump. Under real conditions, this is only fulfilled up to a certain idler energy. The larger the amplification of the idler and signal, the greater the fraction between pump and idler/signal energy. The assumption of an undepleted pump becomes wrong from a certain pump intensity.

The typical gain curve for the pump, signal and idler in pulsed OPA systems can be split into three gain regimes. After initial exponential amplification of the idler and signal pulses, the gain becomes first linear until it reaches saturation and backconversion begins. Eventually, the energy transfer from the pump to signal and idler photon reverses its direction. In theory in the absent of losses and inhomogeneous pump depletion, the pump intensity can principally recover completely. Laser pulses with Gaussian beam profiles and a spatio-temporal intensity

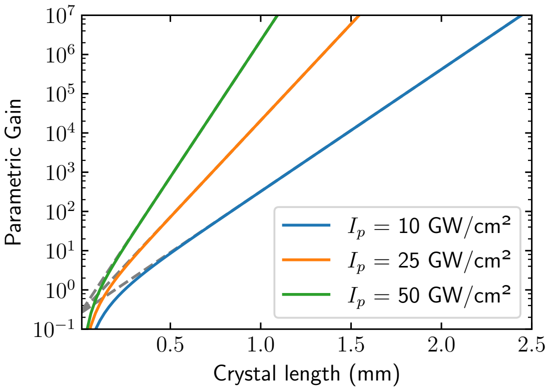

Figure 2.5: Parametric gain calculated for LWIR generation in 1 mm GaSe.

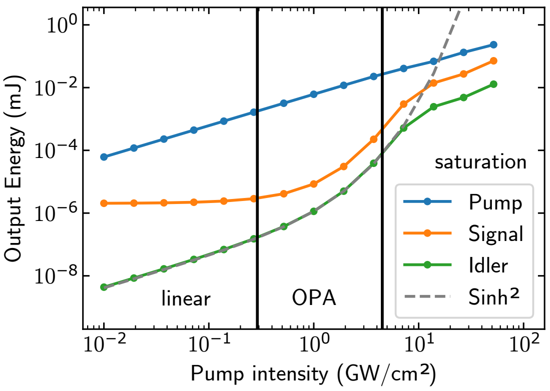

Figure 2.6: Parametric output for LWIR parametric generation in 2 mm GaSe.

distributions lead to varying gain coefficients along time and space.

The output energies for pump, signal and idler are plotted in Fig. 2.6 for a 2 mm GaSe crystal and $I_{20} = 0.49\,\mathrm{MW/cm^2}$ signal seed intensity against the pump intensities. This graph shows three amplification regimes namely the linear, OPA/exponential and saturation/backconversion regime. In the linear regime, increasing the pump intensity results in a linear growth of the idler energy. This is the same region where the exponential approximation eq. 2.34 of the gain coefficient $\sinh^2$ fails for $\Gamma L \gg 1$.

The transition to the OPA regime is shown by the first black line which represents the threshold pump intensity for $\Gamma z = 1$

$$I_{\mathrm{thr}} = \frac{n_1 n_2 n_3 \epsilon_0 c^2}{2\omega_1 \omega_2 d_{\mathrm{eff}}} L^{-2}. \tag{2.36}$$

In the OPA regime, the output idler energy grows exponentially with the input pump intensity. This holds true up to the point where the pump cannot be considered undepleted and saturation begins. The $\sinh^2$ approximation (dotted grey line) becomes inaccurate, the output energies grow slower and eventually result in an ultimate decrease of signal and idler energy as backconversion occurs.

In all processes, the photon flux conserved and generally $\hbar\omega_p + \hbar\omega_s + \hbar\omega_i$ is constant which can be expressed in the form of photon number conservation in the Manley-Rowe-relations [74], neglecting absorption and scattering losses inside the crystal. From this, the intensity equations follow [75]

$$\frac{1}{\omega_3}\frac{\partial I_3}{\partial z} = \frac{1}{\omega_2}\frac{\partial I_2}{\partial z} = -\frac{1}{\omega_1}\frac{\partial I_1}{\partial z}. \tag{2.37}$$

Consequently, one pump photon at ω_1 is necessary to create a photon pair of frequencies ω_2 and ω_3, or the other way around.

2.5.1 Chirped Pulse Amplification

Another limitation factor of optical amplification is the damage threshold of the nonlinear crystals. The maximum pump intensity must be kept below the damage threshold and hence, the pump energy for the amplification is limited. In order to decrease the peak intensity on the crystal surface, the pump and the signal pulses are stretched to longer pulse durations prior to amplification, see Fig. 2.7. The successful implementation of *chirped pulse amplification* (CPA)

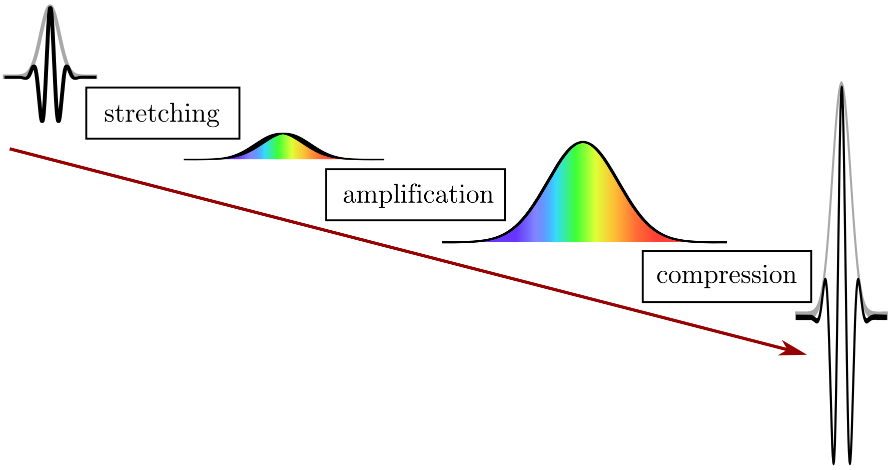

Figure 2.7: Schematic representation of optical parametric chirped pulse amplification, starting from a Fourier limited pulse through chirp before parametric amplification and recompression.

was rewarded with the Nobel Prize in 2018 and has been demonstrated in 1985 by D. Strickland and G. Mourou [31]. After the parametric amplification, compression of the signal and idler pulses is necessary in order to reach transform limited pulse durations and to increase the peak power. Combining CPA with parametric amplification has become the technique of choice to generate high-energy, few-cycle solid-state laser sources in spectral regions where no solid-state laser materials exist. The first implementation of optical parametric chirped pulse amplification in the NIR reaching fs-pulse duration was demonstrated in 1992 by A. Dubietis et. al. [33].

Phase control is the prerequisite of ultrashort pulses in the few-cycle and femtosecond regime. The broader the bandwidth of the signal and idler pulses of an OPCPA system, the more important the involved phases become. The OPA phase is defined as $\theta(t) = \phi_p(t) - \phi_s(t) - \phi_i(t)$ and indicates the energy flow. An OPCPA system exhibits the following phase relations for signal, idler and pump [66, 67]

$$\begin{aligned}
\phi_s &= \phi_s(0) - \frac{\Delta k z}{2} + \frac{\Delta k \gamma_s^2}{2} \int \frac{\mathrm{d}z}{f + \gamma_s^2}, \\
\phi_i &= \phi_p(0) - \phi_s(0) - \frac{\pi}{2} - \frac{\Delta k}{2}, \\
\phi_p &= \phi_p(0) - \frac{\Delta k}{2} \int \frac{f \mathrm{d}z}{1 - f}.
\end{aligned}$$

where $f = 1 - {}^{I_p}/_{I_p(0)}$ is the fraction depletion of the pump beam and $\gamma_s = {}^{\omega_p}/_{\omega_s} {}^{I_s(0)}/_{I_p(0)}$ the input signal photon ratio. The phases of the different pulses are determined by the initial phases of the pump and the signal, as well as by the phase mismatch Δk and the fractional pump depletion. The relationships allow to make a couple of statements. Firstly, the signal phase is independent of the initial pump phase and hence the optical quality of the signal can be ensured. Secondly, only for phase mismatch $\Delta k \neq 0$ the phase of the signal and idler changes during amplification. Thirdly, for perfect phase matching the idler phase only depends on the input phase of pump and signal. For both values being zero, the idler phase equals to

$\pi/2$. For an absent idler intensity at the input, the idler phase self adjusts to ensure maximum gain and the energy from the pump is transferred to signal and idler.

2.6 Optical Kerr effect

The induced polarization is written as the power series (eq. 2.8) of the susceptibility tensor χ and similarly to studying the $\chi^{(2)}$ effects, one can study the consequences following from the $\chi^{(3)}$ interaction. With an input field consisting of three plane waves with $\omega_1, \omega_2, \omega_3$, in analogy to eq. 2.16 in sec. 2.3, the creation of new frequency components $3\omega_i, 2\omega_i \pm \omega_j$ or $\omega_i + \omega_j \pm \omega_k$ follows [68, 70]. These 4-wave-mixing processes are usually highly suppressed since they require phase matching to be driven efficiently. However, there is an intensity dependence of the refractive index, since for $\chi^{(3)}$ interactions, one can write $P \propto \chi^{(3)} E_1 E_2 E_3$ and $E \propto n_2 I E$ neglecting the creation of new frequency components, where $I \propto E^2$ is proportional to the squared electric field. Generally, one can write the refractive index as $n(\omega, I) = n_0(\omega) + \Delta n(I)$. To account for this effect under non-resonant conditions, the refractive index is often written as the linear dependence on the intensity as

$$n(\omega, I) = n_0(\omega) + n_2 I, \tag{2.38}$$

where n_0 is the normal refractive index depending on the frequency and following from $\chi^{(1)}$. Typically, n_2 is positive for optical materials and the total refractive index increases for large intensities. This means that the larger the intensity, the larger the accumulated phase in the material. Considering the spatio-temporal Gaussian intensity profile of a laser pulse, this leads to different effects in time and space.

In the above equation, n_2 is assumed to not depend on the frequency of the light field. This is generally not true, but a reasonable assumption within the spectral bandwidth of a picosecond pulse. Across the electromagnetic spectrum, the value of n_2 can however change significantly. Mostly, the nonlinear refractive index of infrared materials has been measured in the visible or near-IR spectral region. In the mid-IR, this index is usually extrapolated from known values and can be quite inaccurate especially in the long-wave infrared spectral region. Just very recently, some infrared material's nonlinear refractive indices have been measured directly in the mid-IR spectral region [76].

The intensity dependence is playing an important role in frame work of ultrashort, femtosecond pulses and/or pulse propagation in fibres. The nonlinear refractive index n_2 in ZnSe is $1.6 \times 10^{-14}\,\mathrm{cm^2/W}$ at $2.2\,\mu\mathrm{m}$ [76], or $5.4 \times 10^{-16}\,\mathrm{cm^2/W}$ at $1.55\,\mu\mathrm{m}$ in ZBLAN fluoride fibres [77]. This is important for applications where the peak intensity reaches the $\mathrm{GW/cm^2}$ to $\mathrm{TW/cm^2}$ range. Even air exhibits a nonlinear refractive index of $4 \times 10^{-19}\,\mathrm{cm^2/W}$ at $0.8\,\mu\mathrm{m}$ at atmospheric pressure [78], which must be considered for free propagation of $> 100\,\mathrm{mJ}$-energy range, few-cycle pulses used, for example, as near-IR high-energy driver sources for high-harmonic generation.

The phenomena resulting from the intensity dependent refractive index are ascribed to the *optical Kerr effect.* In space, if a pulse with a Gaussian intensity profile transmits through a medium with significantly large $\mathrm{n}_2 > 0$, the central part of the intensity profile will experience a larger refractive index than the outer parts. This implies an intensity dependent phase change and consequently the transmitted pulse front will be distorted. This distortion leads to a focusing behaviour of the pulse. In the case of an infinitely long bulk medium, this is a run-away effect. The wavefront distortion leads to a decreasing beam waist, and the smaller beam waist leads to an even more severely distorted pulse front. This effect continues until the damage threshold is reached and the material is damaged. The critical power for self-focussing is defined as follows [68]

$$P_{crit} = \alpha \frac{\lambda^2}{4\pi n_0 n_2} \tag{2.39}$$

where α depends on the intensity profile and usually is close to 2. This equation shows that longer wavelengths are advantageous in order to avoid critical self-focussing. This is one advantage when using MWIR and LWIR radiation. In the case of thin substrates, a plan-parallel optical element with significant n_2 acts simply as a lens.

A similar effect (not related to the Kerr nonlinearity) occurs in a gain medium used for the generation of high-power lasers. The inhomogeneous heating of the gain medium typically with Gaussian temperature distribution induces a change of refractive index ${}^{dn}\!/_{dT}$ or mechanical stress. The outcome of these phenomena is again a wavefront distortion of the transmitted pulse, referred to as *thermal lensing.*

The temporal shape of a laser pulse follows a certain function, like a Gaussian, hyperbolic secant or Lorentzian pulse shape. The phase change in temporal domain evokes an effect referred to as self-phase modulation (SPM). The derivative of the phase leads to the creation of new frequency components and modulates the pulse spectrum. The frequency change can be written in terms of the nonlinear phase [63]

$$\omega(t) = \omega_0 + \delta\omega(t) = \omega_0 - \frac{\mathrm{d}}{\mathrm{d}t}\phi_{\mathrm{NL}}(t), \tag{2.40}$$

$$\phi_{\mathrm{NL}}(t) = n_2 \frac{\omega_0}{c} I(t) L, \tag{2.41}$$

directly relating to the nonlinear refractive index and the intensity.

In a nonlinear material, the accumulated phase of the spatio-temporal profile of a laser pulse with an intensity maximum at its center is summarized with in the B-integral, defined as

$$B = \frac{2\pi}{\lambda} \int n_2 I(z)\, dz. \tag{2.42}$$

It accounts for the intensity dependent phase accumulated over the length of the nonlinear medium in the temporal domain. This effect becomes especially important for the transmission through long substrates as its the case in gain media inside oscillators, fibres or regenerative amplifiers. The B-integral is considerably important as the phase can not be compensated by second and third order polynomial phase only and common compression schemes fail, see Sec. 3.3.2. In practice, large values of this integral lead to the degradation of the pulse quality and shape. In practice, the accumulated phase is reduced by the use of picosecond pulses with lower peak intensity than femtosecond pulses. This is the reason why the pulse duration for the pump seed in Sec. 4.3 is stretched in multiple chirped-volume-Bragg-gratings (CVBG) prior to amplification in the Thulium-fibre and regenerative amplifier. In practice, values below 2π are acceptable.

The nonlinear refractive index n_2 introduced in eq. 2.38 has been defined for linearly polarized light. Theoretically and experimentally, it has been shown that the nonlinear refractive index reduces by a factor of $2/3$ for circular input polarization [79]. Hence, in chirped pulse amplification systems, using circularly polarized light decreases the accumulated B-integral, reduces self-phase modulation and increases the self-focussing threshold.

2.7 Nonlinear Schrödinger Equation

For large intensities, the nonlinear contribution of the material significantly changes the amplitude, the spectrum and the phase of a pulse. It cannot be treated like a perturbation any longer and an alternative description for the evolution of the pulse amplitude is necessary. This is the case, for example, for pulse propagation inside optical fibres as the mode size is confined to a few micrometer which results in large intensities. The equation describing accurately the amplitude A, the phase and the spectrum along the propagation direction is the nonlinear Schrödinger equation (NLSE) and reads [63, 70]

$$\frac{\partial A(z,t)}{\partial z} = -\frac{\alpha}{2}A + \int_{-\infty}^{\infty} \frac{g(\omega)}{2}\tilde{A}\exp(-i\omega t)\,d\omega + \sum_{n\geq 1}\beta_n \frac{i^{n+1}}{n!}\frac{\partial^n A}{\partial t^n} \tag{2.43}$$

$$+ i\gamma\left(1 + i\tau_{shock}\frac{\partial}{\partial t}\right)\left(A(t)\int_{-\infty}^{\infty} R(\tau)|A(t-\tau)^2|\,d\tau\right), \tag{2.44}$$

where α is the attenuation coefficient accounting for losses, g the spectral gain coefficient, $\tilde{A}$ the amplitude in frequency space, β the wavevector introduced in eq. 2.12, γ the nonlinear coefficient, τ_{shock} the shock time, and $R(\tau)$ the delayed Raman response function.
The change of the spectrally dependent amplitude along propagation direction on the left side results from multiple linear and nonlinear effects. The first term on the right side of the equation simply describes a linear attenuation along the propagation direction. The second term involves the gain of the medium with a certain gain profile integrated over all frequencies, used for example in fibre amplifiers. The third term represents the material dispersion described in sec. 2.2. All terms in the second line have the prefactor $i\gamma$ indicating a phase dependency stemming from the nonlinearity of the medium. The nonlinear refractive index n_2 is hidden inside γ which is defined as

$$\gamma = \frac{n_2\omega_0}{cA_{\text{eff}}},$$

where A_{eff} is the effective mode area inside the fibre and c the speed of light. Neglecting all other terms, self-phase modulation can be written as

$$\frac{\partial A}{\partial z} = i\gamma|A|^2 A,$$

clearly showing intensity dependence $|A|^2$. The phase modulation governed by the intensity evokes not only a phase change with opposite sign at the wings, but also creates new frequency components according to

$$\omega(t) = \omega_p + \frac{\partial}{\partial t}\phi(t),$$

as already described in eq. 2.40, Sec. 2.6. The leading part creates red shifted and the trailing part blue shifted frequencies. This phenomenon becomes important for soliton formation described in section 5.3.2.

The last term of the NSLE proportional to $R(\tau)$ accounts for the temporal Raman response of the medium which has an instantaneous and delayed contribution. The delayed contribution is caused by excitation and deexcitation of the crystal structure. This effect leads to a frequency shift towards longer wavelengths caused by Raman scattering which is an energy exchange with the crystal lattice. This effect can be explored for flexible wavelength shifting in OPA front-end architectures.

If the group index is also intensity dependent, the central part of the pulse will have a different velocity than the wings. This results in a self-steepening and a shock formation which is expressed through τ_{shock} and is defined as

$$\tau_{shock} = \frac{1}{\omega_0} - \left[\frac{1}{n_{\text{eff}}}\frac{\mathrm{d}n_{\text{eff}}(\omega)}{\mathrm{d}\omega}\right]_{\omega_0} - \left[\frac{1}{A_{\text{eff}}}\frac{\mathrm{d}A_{\text{eff}}(\omega)}{\mathrm{d}\omega}\right]_{\omega_0}, \tag{2.45}$$

and can be calculated from the fibre's effective refractive index n_{eff} and mode size A_{eff}. This associated effect can result in the breaking of the pulse along propagation.

3

Design concepts of high-energy mid-IR OPCPAs

Triggered by the lack of solid-state lasers in the mid-infrared (mid-IR) region, parametric down-conversion enables access to the wavelength range between 3 and 20 µm. The generation of pulses with high peak power and femtosecond duration requires broad seed spectra and high energy pump sources in order to reach the millijoule pulse energy range. With the commercialisation of Cr:ZnS oscillators, the important spectral characteristics for the seed of the pump and the broadband signal are readily accessible necessary for infrared OPCPAs. In this work, the pump wavelength is at 2.05 µm, the signal for LWIR at 2.4 µm and for MWIR at 3.2 µm, where a Cr:ZnS front-end provides the seed for the pump and the signal simultaneously. The output characteristics of an optical parametric chirped pulse amplifier (OPCPA) are dependent on the design of the system and there are a number of criteria which optimize the output. The main goals of optimization can be summarized as follows [38]: (a) extract the maximum pump energy and reduce power requirement, (b) create signal output energy with a stability superior to the pump, (c) avoid laser-induced damage and (d) minimize beam distortion.

Basic concepts for the generation of ultrashort mid-wave infrared (MWIR, 3 - 8 µm) and long-wave infrared (LWIR, 8 - 15 µm) pulses using parametric amplification are introduced. An overview of the materials and nonlinear crystals which determine the spectral properties of the amplified pulses is provided in the first part. Secondly, the phase matching properties for the two infrared regions in zinc germanium phosphide ($ZnGeP_2$, ZGP) and gallium selenide (GaSe) relevant for the parametric amplification are given. It covers the dependencies between pump and signal pulses in temporal and spectral domain and their influence on the amplification, and aims to develop the best implementation with the underlying physical properties. The advantages of a 2 µm pump wavelength, in contrast to a 1 µm pump wavelength, are presented in detail. Typical optimization possibilities are discussed to finally present the calculations corresponding the implementation of the LWIR OPCPA.

Most of the presented design criteria are valid for the generation of LWIR pulses in GaSe and compared to the generation of MWIR pulses in $ZnGeP_2$. For the details about parametric MWIR generation in $ZnGeP_2$, the reader is referred to [80]. The parametric simulations in this chapter rely on the *Sisyfos* code [81], calculating the frequency conversion between two input beams with a defined spectral distribution and energy. It solves the differential equations 2.27-2.29 for $\chi^{(2)}$ interactions, introduced in sec. 2.5, including diffraction, birefringence, non-collinear geometry and is based on a set of Sellmeier equations for the refractive index of the nonlinear crystal.

This chapter aims to provide an overview of design criteria in $ZnGeP_2$ and GaSe, including insights into different phase matching schemes, tackling bandwidth limitations due to intrinsic crystal properties and explaining the difficulties of parametric amplification in GaSe. Inhomogeneous depletion and the influence of the signal to pump pulse duration are addressed in order to increase efficiency. Finally, calculations incorporating the earlier findings pave the way for the best OPCPA implementation for the generation of long-wave infrared pulses.

3.1 Infrared crystals and materials

The choice of the nonlinear crystal sets the bases for the parametric interaction as it sets the limitations for achievable energies, spectrum and average power. Firstly, suitable nonlinear crystals need to have low absorption over the spectral region covering the pump, the signal and the idler spectrum. While absorption of a percent per centimetre is acceptable, it lowers the damage threshold and leads to undesired thermal heating limiting the average power in the crystal. The very well known oxide crystal beta barium borate (BaB_2O_4, BBO) is transmissible up to 2 µm and potassium titanyle arsenate ($KTiOAsO_4$, KTA) has the broadest transmission window among the oxide crystals of up to 4 µm but is limited by multiphonon absorption occurring above 4 µm [82]. Oxide crystals exhibit a high damage threshold of TW/cm^2 in the near-IR range, but have a limited mid-IR transparency range and are therefore not suitable for MWIR and LWIR generation. The alternative are non-oxide materials where multiphonon absorption sets the intrinsic limit well above 20 µm. Contrary to the oxides, the development of non-oxide materials has been hampered by their volatile production techniques and the difficulty of producing large size single domains [82]. As a consequence, these crystals exhibit more defects and losses. The long-wavelength transmission comes at the expense of smaller band gaps which dictate the lowest pump photon energy to be less than half the band gap energy, in order to avoid two-photon absorption. The use of Ti^{3+}, Nd^{3+} or Yb^{3+} based pump sources in the near-IR become unfeasible. Alternatively, Er^{2+} or Er^{3+} lasers near 1.5 µm or 2.9 µm as well as Tm^{3+} and Ho^{3+} lasers at 2 µm can be used instead.

Besides the transparency range, a high nonlinear coefficient d_{eff} is the prerequisite for high-energy parametric interactions, see gain coefficient in sec. 2.5, eq. 2.33. Non-oxide materials typically exhibit one or two orders of magnitude higher nonlinear coefficient, but have a rather low damage threshold in the continuous-wave and picosecond regime. With the use of

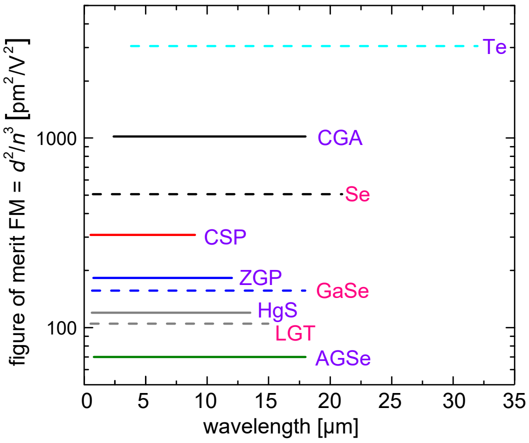

Figure 3.1: Figure of merit, ratio between effective nonlinearity d and refractive index n, directly relating to the conversion efficiency for non-oxide birefringent crystals in the infrared region, modified Figure taken from [82]. Crystal abbreviations: Tellurium (Te), Cadmium Germanium Arsenide ($CdGeAs_2$, CGA), Selenium (Se), Cadmium Silicon Phosphide (CSP, $CdSiP_2$), Zinc Germanium Phosphide ($ZnGeP_2$, ZGP), Gallium Selenide (GaSe), Mercury Thiogallate ($HgGa_2S_4$, HGS), Lithium Gallium Tellurite ($LiGaTe_2$, LGT), Silver Gallium Selenide ($AgGaSe_2$, AGSe).

femtosecond pulses, these crystals allow high gain at moderate intensities of a few GW/cm^2. The crystals $ZnGeP_2$ and GaSe have $d_{\text{eff}} = 78.4\,\text{pm/V}$ and $56.0\,\text{pm/V}$, respectively and a few millimetre crystal length of $ZnGeP_2$ and GaSe are required to reach significant gain in a single pass. The handling of non-oxide materials can, however, be more subtle due to the softness and the lower damage threshold one or two orders of magnitude compared to oxide crystals. Fig. 3.1 summarizes numerous nonlinear infrared crystals with respect to the figure of merit (FM) d_{eff}^2/n^3, found in eq. 2.30 and eq. 2.33. d_{eff} is the effective nonlinear coefficient and n the refractive index. The choice of crystals is limited by their intrinsic properties, their commercial availability and their sizes. The crystals $AgGaS_2$, $AgGaSe_2$, $CdSiP_2$, GaSe, Te and $ZnGeP_2$ are commercially available. The elementary Se and Te have high linear losses over the entire IR-range which makes them useful for diagnostic purposes of ultrashort pulses only. $AgGaS_2$ and $AgGaSe_2$ have poor thermal conductivity and anisotropic thermal expansion. Cadmium Germanium Arsenide ($CdGeAs_2$, CGA) requires low temperature in order to avoid residual losses and absorption features and Cadmium Silicon Phosphide (CSP, $CdSiP_2$) supports only narrow linewidths at 2 µm pump and its use is restricted to the multiphonon absorption limit at 6.5 µm. The crystals $ZnGeP_2$ and GaSe exhibiting high second-order nonlinearity are the best choice and are used in this work being reliable and well known among the community both allowing for 2 µm pumping. New mid-IR crystals are under development by mixing binary or ternary components aiming for an extended transmission range and/or improved thermo-mechanical properties. Structures enabling quasi-phase matching by periodically poled orientation pattern are also useful but are restricted to small aperture [83, 84].

Promising is the development of Barium based nonlinear crystals [85]. The transparency range of the new crystal types are shown in relation to the well-known nonlinear infrared crystals in Fig. 3.2. $BaGa_2GeS_6$ (BGGS) and $BaGa_2GeSe_6$ (BGGSe) are uniaxial crystals, and $BaGa_4S_7$ (BGS) and $BaGa_4Se_7$ (BGSe) biaxial. As the mid-IR cutoff wavelengths follow $S < Se$ for chalcogenides, the crystals incorporating selenide have a higher multi-phonon absorption threshold and support longer wavelength transmission. The same restriction applies here, means that the higher the cut-off wavelength, the narrower the bandgap and consequently, the longer the required pump wavelength. These crystals all support 1 µm as well as 2 µm pumping and transmit wavelengths up to 10 µm (BGGS and BGS) or 16 µm (BGGSe and BGSe). They appear well suited for MWIR as well as LWIR parametric processes with nonlinear coefficients of tens pm/V. Unfortunately, their characterization is still ongoing and they are not yet commercially available. So far, BGSe appears to be the best candidate for LWIR generation with type II phase matching at $\theta = 5°$ and $\phi = 90°$.

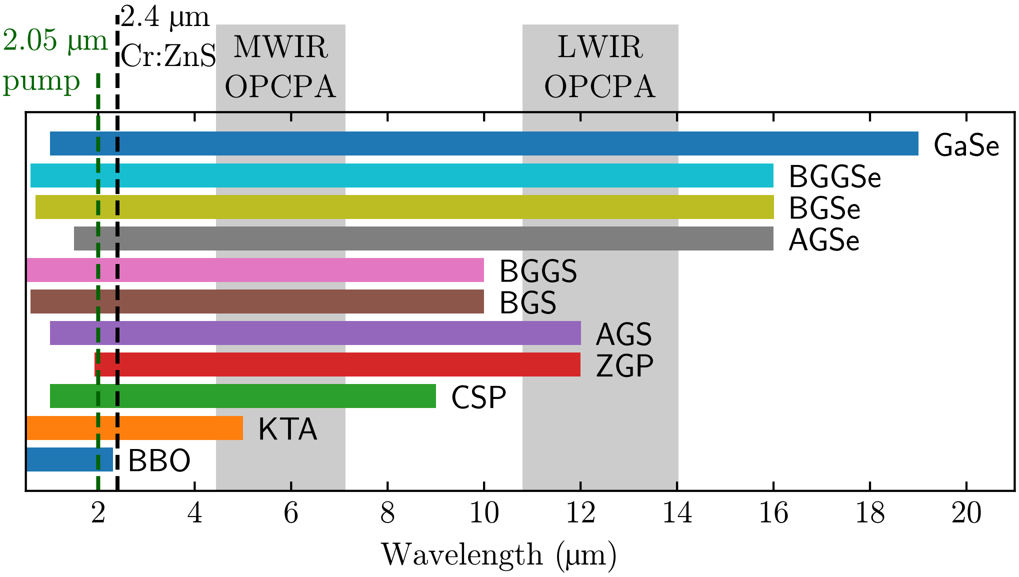

Figure 3.2: Transparency range of nonlinear crystals covering the target MWIR and LWIR spectrum (grey bar): BBO, beta barium borate (BaB_2O_4); KTA, potassium titanyle arsenate ($KTiOAsO_4$); CSP, cadmium silicon phosphide ($CdSiP_2$); AGS silver gallium sulfide ($AgGaS_2$); ZGP, zinc germanium phosphide ($ZnGeP_2$); BGS, barium gallium sulfide ($BaGa_4S_7$); BGGS, barium gallium germanium sulfide ($BaGa_2GeS_6$); AGSe, silver gallium selenide ($AgGaSe_2$); BGSe, barium gallium selenide ($BaGa_4Se_7$); BGGSe, barium gallium germanium selenide ($BaGa_2GeSe_6$); GaSe, gallium selenide. Wavelength of the pump (green dotted line), and the signal seed (black dotted line) (from the Cr:ZnS oscillator).

For the comparison of $ZnGeP_2$ and GaSe, the relevant properties and gain parameters are listed in Tab. 3.1. The transparency range makes $ZnGeP_2$ only usable in the MWIR region and GaSe for both MWIR and LWIR generation. The table lists the values for a signal at 2.4 µm for LWIR and 3.2 µm for MWIR. GaSe has a lower second-order linearity disadvantageous for the gain but can in return be pumped with higher peak intensities. $ZnGeP_2$ can securely allow peak intensities up to 10 GW/cm^2 [86] and GaSe 50 GW/cm^2 for a 3 ps-2 µm-pump. Type I phase matching is more advantageous in $ZnGeP_2$, and type II in GaSe, as discussed later in sec. 3.2.2. The handling of $ZnGeP_2$ is easier as it has an acceptance angle 5 times larger than GaSe and a lower walk-off angle. Their performance in an OPCPA generating MWIR and LWIR pulses are studied throughout this chapter.

	$ZnGeP_2$		GaSe	
Transparency (µm)	1.9 – 10.6		0.65 – 18	
$\lambda_{\mathrm{signal}}$(µm)	2.48	3.2	2.4	3.2
d_{eff}(pm/V)	80.7	78.4	53.7	56.0
phase matching	$o \rightarrow ee$	$o \rightarrow ee$	$e \rightarrow oe$	$e \rightarrow oo$
$n(\lambda_p)$	3.14	3.14	2.72	2.72
angl. acc. (mrad cm)	6.5	8.79	1.5	2.09
$\phi_{\mathrm{walk-off}}$(°)	0.69	0.66	3.44	3.21
$\theta_{\mathrm{coll.PM}}$(°)	51.9	54.9	12.2	11.5
I_{sft}(GW/cm^2)	10	10	50	50
$\Gamma(I_{\mathrm{sft}})$(1/mm^2)	8.0	11.2	4.6	5.6

Table 3.1: Gain parameter for the nonlinear crystals $ZnGeP_2$ and GaSe for MWIR and LWIR generation. The pump wavelength is 2.05 µm for a 2.4 and 3.2 µm signal wavelength. d_{eff}: effective nonlinearity, $n(\lambda_p)$: refractive index at pump wavelength, angl. acc.: angular acceptance, $\phi_{\mathrm{walk-off}}$ walk-off angle, $\theta_{\mathrm{coll.PM}}$: collinear phase matching angle and, I_{sft}: safe working intensity for 3.0 ps pump pulse duration, $\Gamma(I_{\mathrm{sft}})$: respective parametric gain

3.2 Parametric amplification in ZGP and GaSe

Beyond the available nonlinear crystals in the infrared, $ZnGeP_2$ and GaSe are most promising in terms of transparency range for the generation of broadband MWIR and LWIR idler pulses via parametric amplification. The amplified spectrum determines the Fourier limit of the output pulses of the amplifier, and thereby dictates whether or not the output pulses can reach femtosecond duration or even the few-cycle regime. The intrinsic crystal properties determining the bandwidth of the parametric processes and the different aspects of improving the bandwidth will be discussed in this section.

3.2.1 Collinear and non-collinear phase matching

A first flavour for the supported bandwidth provides the phase matching (PM) graph for the possible PM types. The PM angle is calculated from energy and momentum conservation, where the momentum of the different pulses depends on the ordinary and the extraordinary refractive indices of the crystal, depending on the input polarization. As a consequence, different crystals do not necessarily support all wavelength combinations. Fig. 3.3 shows the PM angle in dependence of the signal and idler wavelength for the nonlinear crystals (a) $ZnGeP_2$ and (b) GaSe for a 2.05 µm pump. In $ZnGeP_2$, type I PM offers the broadband generation of an MWIR idler around 4 µm. In GaSe, however, type I PM supports an idler at 10 µm and type II at 12 µm both with a much weaker angle dependence than $ZnGeP_2$. In GaSe, the angles of the two PM types differ by only 1.3° and the best PM configuration requires further investigations. The here presented PM angles represent the internal angle. Typically, the nonlinear crystal is cut to the PM plane which allows to use the crystal under normal incidence. However, GaSe can only be cut in one plane and the crystal tilted. Due to the refractive index of the crystal, the external angle is much larger than the internal one and hence, in case of GaSe, the internal angle of 12.2° corresponds to 34° externally. Consequently, the tilt of the crystal surface is large and has some consequences which are discussed later.

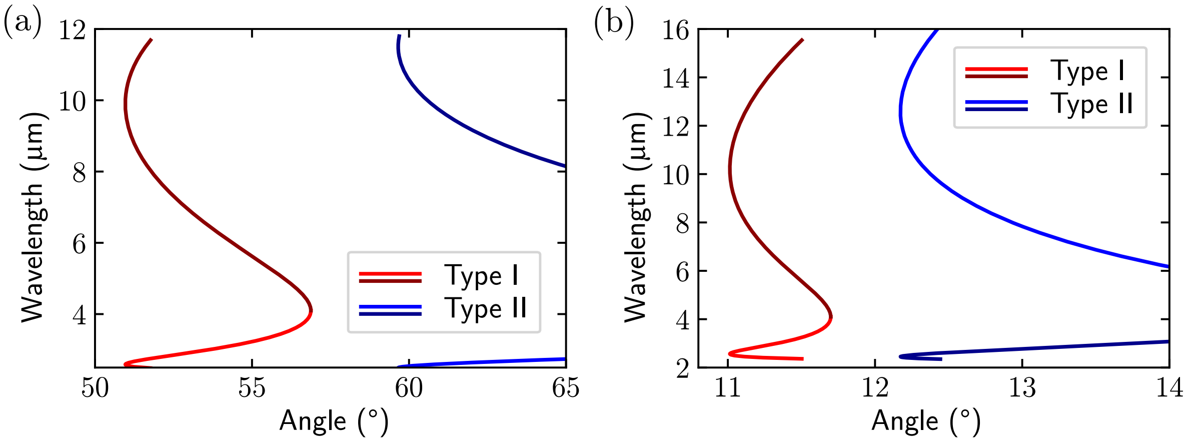

Figure 3.3: Phase matching angles (internal) for a 2.05 µm pump in (a) $ZnGeP_2$, pump in (o) and (b) GaSe, pump in (e) for type I and type II. The lighter line indicates the signal, the darker line the idler.

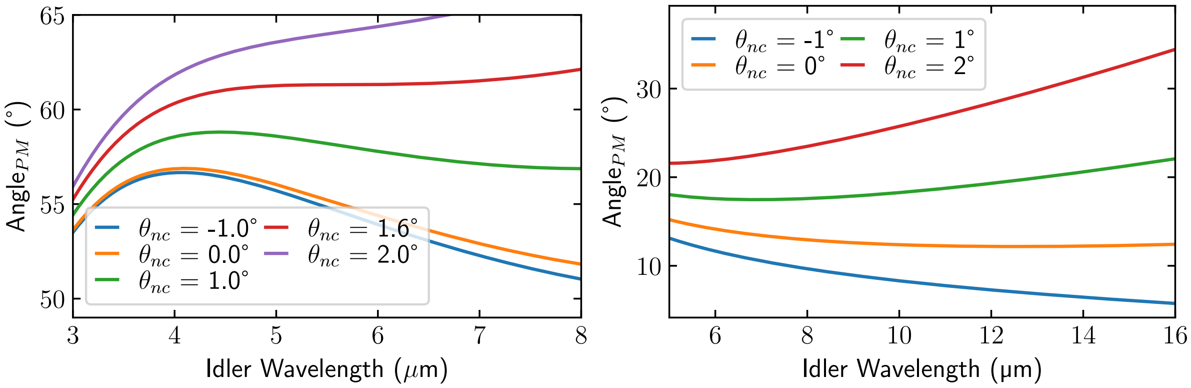

(a) $ZnGeP_2$, type I, pump(o) -> signal(e) + idler(e). **(b)** GaSe, type II, pump(e) -> signal(o) + idler(e).

Figure 3.4: Non-collinear phase matching in $ZnGeP_2$ for MWIR and GaSe for LWIR for different non-collinear angles and a 2.05 µm pump.

In the past, non-collinear geometry has been found advantageous for parametric amplification when the frequency spacing between the pump and the idler pulse is large. It prevents severe temporal walk-off caused by crystal dispersion and enlarges the PM bandwidth [87]. In practice, a small angle θ_{nc} is introduced between the pump and the signal. To guarantee energy and momentum conservation, the phase matching angle needs to be adjusted, see Fig. 3.4. The two graphs display the different phase matching characteristics in $ZnGeP_2$ and GaSe, both pumped at 2.05 µm. Non-collinear phase matching increases the bandwidth in $ZnGeP_2$, with an optimal non-collinear angle at 1.6°. On the contrary, non-collinear geometry reduces the bandwidth in GaSe (Fig. 3.4(b)) which is not the typical behaviour. Consequently, non-collinear configuration is advantageous in $ZnGeP_2$, but should be avoided in GaSe.

3.2.2 Influence of group velocity mismatch - comparing 1 µm and 2 µm pumping

The bandwidth of a parametric process is determined by the group velocity match between the pump, signal and idler pulses, as shown in sec. 2.6, eq. 2.35. The group velocity mismatch (GVM) between two pulses with index $1, 2$ can be derived from the group velocity dispersion (GVD), introduced in eq. 2.14 in sec. 2.2, and is defined as

$$\delta_{1,2} = \left(\frac{1}{v_{g,1}} - \frac{1}{v_{g,2}} \right), \tag{3.1}$$

directly relating to eq. 2.35, where $v_{g,1}$ and $v_{g,2}$ are the group velocities of the respective pulses. GVM leads to temporal walk-off of the interacting pulses and limits the interaction length. The pulse splitting length indicates the propagation length after which the pulses separate temporarily. Beyond this length, parametric interaction is not taking place and the use of longer crystals becomes obsolete. Positive GVM means that the pump pulse travels faster than the generated pulse which directly influences the parametric gain, as shown in sec. 3.4.1). The group velocity mismatch is shown for GaSe with a 1 µm pump in Fig. 3.5, for a 2 µm pump in Fig. 3.6 and for $ZnGeP_2$ with a 2 µm pump in Fig. 3.7. From these values, the pulse splitting length can be calculated being defined as [35]

$$l = \frac{\tau}{\delta_{s,i}} \tag{3.2}$$

where τ is the pump pulse duration and $\delta_{s,i}$ is the group velocity mismatch between the pump and signal/idler. Tab. 3.2 summarizes the pulse splitting lengths for the three configurations calculated for a pump pulse duration of 3 ps. For all possibilities, the pulse splitting length is exceeding the nonlinear crystal length of maximally 2 mm used in the experiments (this might become critical for the idler with 1 µm pump in GaSe).

	1 µm GaSe	2 µm GaSe	2 µm $ZnGeP_2$	
l_{sp}	44 mm	250 mm	51 mm	signal
l_{ip}	4.7 mm	100 mm	26 mm	idler

Table 3.2: Pulse splitting length for 1 µm and 2 µm pump in GaSe and 2 µm,3 ps pump in $ZnGeP_2$.

The broadest parametric bandwidth is expected if the group velocities of the signal and the idler are similar, as its the case in $ZnGeP_2$. Also, it becomes apparent that pumping GaSe at 2 µm is favourable compared to 1 µm pumping since the group velocities differ less. The large drawback with the 2 µm pump, however, is that the group velocities of signal and idler have opposite signs and walk off the pump in opposite directions. The consequences of these discrepancies manifest in the following parametric coefficient analysis.

The parametric coefficient $\text{sinc}^2(\Delta kL/2)$, introduced in sec. 2.5 (eq. 2.30), provides more insight into the amplification bandwidth of the process. In the following, the polarization plane of the light pulses is taken to be the xy-plane, and z is considered the propagation direction. In addition to the phase matching $\Delta k_{x,y}$ due to the birefringence of the nonlinear crystal

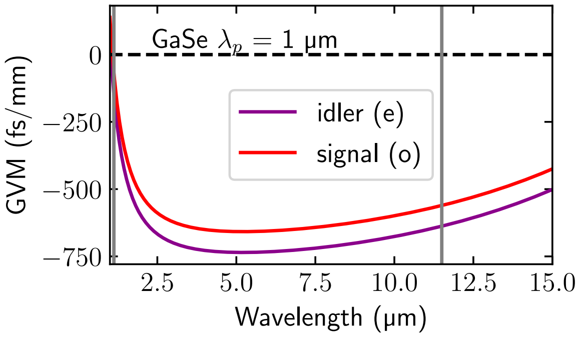

Figure 3.5: GVM for a 1.03 µm pump in GaSe at 14.1° with $\nu_s(1.12\,\mu\text{m}) = -68$ fs/mm and $\nu_i(11.5\,\mu\text{m}) = -638$ fs/mm, indicated by grey vertical lines.

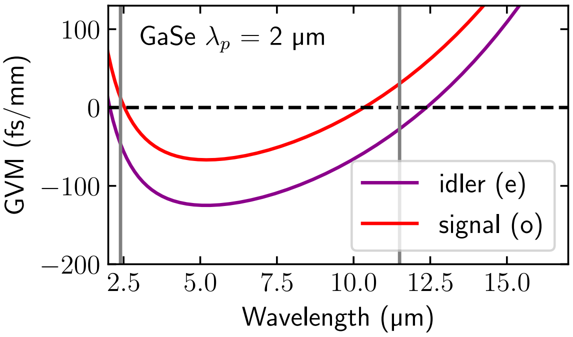

Figure 3.6: GVM for a 2.05 µm pump in GaSe at 12.2° with $\nu_s(2.4\,\mu\text{m}) = 12$ fs/mm and $\nu_i(11.5\,\mu\text{m}) = -28$ fs/mm, indicated by grey vertical lines.

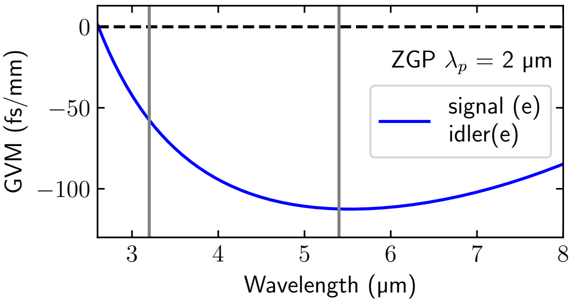

Figure 3.7: GVM for a 2.05 µm pump in ZnGeP$_2$ at 58.5° with $\nu_s(3.2\,\mu\text{m}) = -58$ fs/mm and $\nu_i(5.4\,\mu\text{m}) = -112$ fs/mm, indicated by grey vertical lines.

(eq. 2.24), it takes into account the group velocity of the three interacting beams Δk_z (eq. 2.35) and scales with the thickness of the nonlinear crystal L. Different group velocities lead to temporal walk-off between the input pulses and can have severe consequences for the output energy and spectrum. The longer the crystal, the higher the risk of temporal walk-off. This is another reason why shorter crystals with high nonlinearity d_{eff} are advantageous. In the context of femtosecond pulses, i.e. for optical parametric amplification (OPA) or difference-frequency generation (DFG) systems the temporal overlap becomes even more important.

The GVM in GaSe is much more pronounced for LWIR generation than for MWIR generation in ZGP, significantly influencing the amplification bandwidth. The influence of the GVM becomes clear in Fig. 3.8. In this graph, the parametric coefficients for ZnGeP$_2$ (type I, $\theta = 58.5°$, $\theta_{nc} = 2°$) and GaSe (type II, $\theta = 12.2°$ collinear) pumped at 2.05 µm with a 2 mm thick crystal are calculated with (solid line) and without (dashed line) taking the different group velocity into account. If the different group velocities in the crystal are taken into consideration, the two crystals show different behaviour. In ZnGeP$_2$ for the MWIR amplification, the group velocity of the three pulses barely influences the parametric coefficient. In GaSe for the LWIR, however, the group velocity mismatch Δk_z reduces the bandwidth by more than a factor of 5 and the temporal walk-off in GaSe severely limits the signal output spectrum. The parametric gain scales exponentially with the crystal thickness, thus a certain thickness is necessary to have significant gain. Therefore, when designing the OPCPA, one needs to ponder between bandwidth and gain.

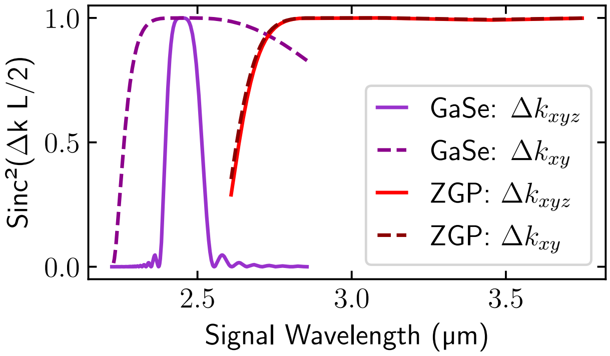

Figure 3.8: Comparison of parametric coefficient with (solid line) and without (dashed line) group velocity consideration for 2 mm thick GaSe (type II) and $ZnGeP_2$ (type I).

3.2.3 Wavelength tuning in GaSe

At the beginning of this chapter, the phase matching angle for $ZnGeP_2$ and GaSe have been presented in Fig. 3.3. In the parametric process, the angle of the nonlinear crystal determines which wavelength components can be amplified in the parametric process. In both crystals, the angle changes slightly across the target spectrum and needs adjustment depending on the desired idler wavelength. The resulting amplification is then given by the overlap between the seed spectrum and the phase matching bandwidth. Fig. 3.9 shows the parametric conversion efficiency for type I phase matching in GaSe at different crystal angles. The amplified signal spectrum shifts from a broad bandwidth of > 200 nm around 2.55 μm to a narrow spectrum of 40 nm at 2.4 μm, given the seed covers the whole spectrum.

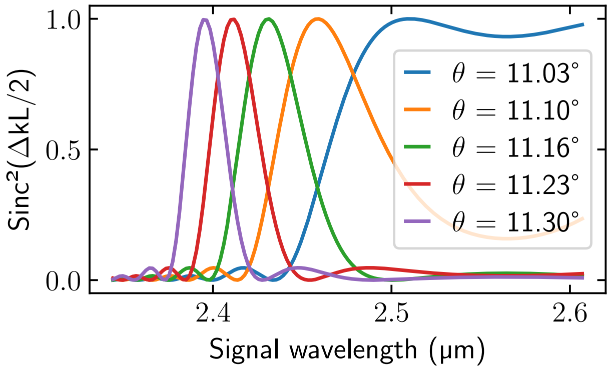

Figure 3.9: Conversion efficiency for type I phase matching in 2 mm GaSe for different phase matching angles (pump at 2.05 μm).

The same phenomenon is visible in Fig. 3.10 where the parametric coefficient in GaSe for a 2 μm pump is shown for type I and type II phase matching at three different angles and for three crystal thicknesses, with respect to the signal wavelength at the bottom and the idler wavelength at the top. It shows that type I phase matching enables a broad idler spectrum around 10 μm when seeded with 2.6 μm signal. Changing the angle of the nonlinear crystal shifts the phase matching spectrum. When rotating the crystal by 0.2° to 11.27° to amplify the signal seed spectrum at 2.4 µm, the spectrum becomes narrow, especially for a 2 mm thick crystal necessary for the first amplification stage (Fig. 3.10(b)). The alternative type II phase matching enables better amplification of wavelengths beyond 12 µm, as shown in Fig. 3.10(c)). This analysis motivates why it is not advisable to only consider the *simple* phase matching condition, as the group velocity dispersion can have a huge influence and reduces the supported bandwidth, and underlines the angle sensitivity of this process. Amplifying idler pulses at 10 µm is possible with large bandwidth, but aiming for longer wavelengths comes at the expense of bandwidth, no matter type I or II phase matching.

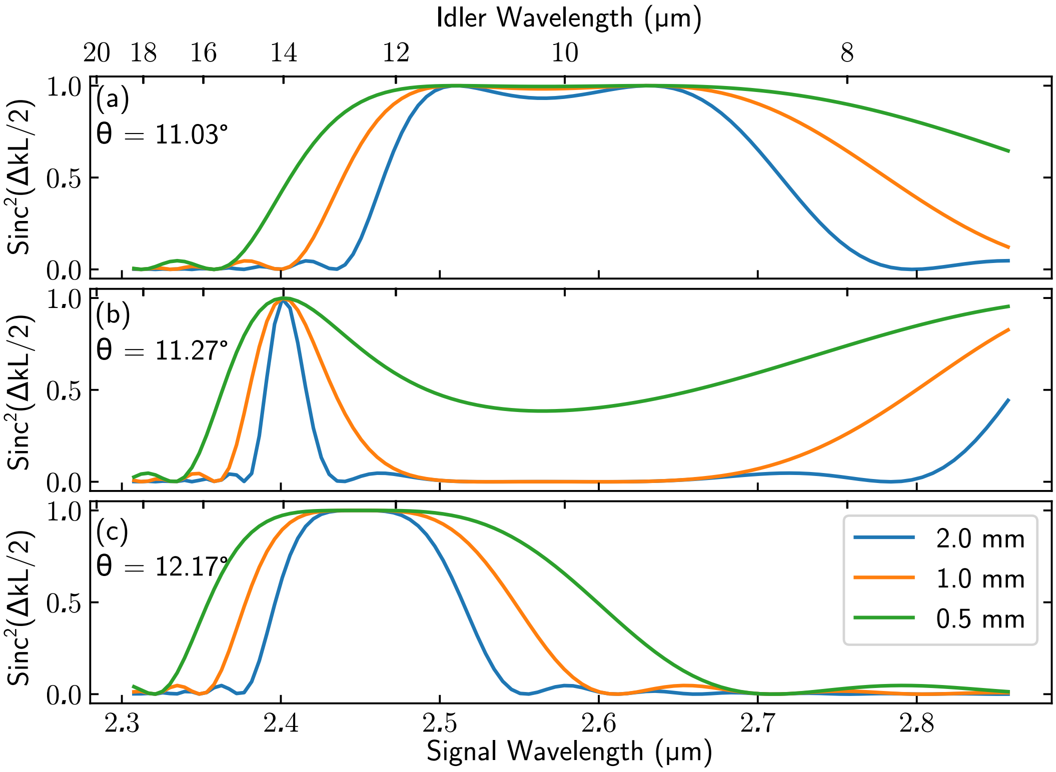

Figure 3.10: Efficiency of idler generation in GaSe for specific phase matching angle with 2.05 µm pump depending on the crystal thickness. (a) and (b) type I, (c) type II phase matching.

In the newly developed crystal BGSe, being transparent up to 16 µm and the possibility of pumping at 1 and 2 µm wavelength (see Fig. 3.2), the problem of group velocity mismatch becomes even more prominent. As already mentioned, this is the most promising candidate in terms of effective nonlinearity among the other barium based crystals. Fig. 3.11 shows the parametric coefficient for GaSe and BGSe with a thickness of 2 mm pumped at 2.05 µm, where GaSe supports a signal bandwidth of 115 nm and BGSe 36 nm. Knowing that the effective nonlinearity of BGSe is lower than GaSe by more than a factor of 2, it is questionable whether or not the possibility of applying anti-reflection coating and cutting the crystal to the phase matching plane outbalances the much narrower bandwidth and lower parametric gain.

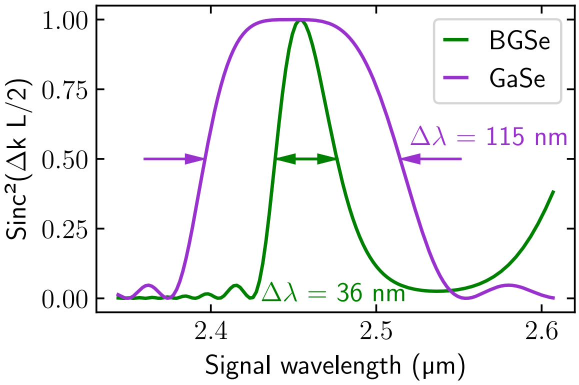

Figure 3.11: Conversion efficiency and bandwidth in 2 mm thick nonlinear crystal. Type II phase matching in GaSe at $\theta = 12.17°$ and BGSe at $\theta = 5.0°$ and $\phi = 90°$.

3.2.4 Spatio-temporal distortion

The most efficient way of generating a high energy output is to seed all OPA stages with the target wavelength, namely 11.5 µm for the LWIR and 5 µm in the MWIR. It ensures a beam profile without angular dispersion and the largest amplification factor. Since the idler is usually created by the parametric interaction itself, at least one stage needs to be seeded with the signal. Seeding with the signal or the idler pulse is one of the design criteria for a multi-stage OPCPA setup.

The last stage of an OPCPA must ensure beam profiles which are suitable for the following experiments, no matter what geometry has been employed in the previous stages. A collinear geometry provides spatially undispersed signal and idler profiles, whereas non-collinear geometry ensures a non-dispersive profile only for the seed pulse. The other pulse requires an additional angular re-shaping [64]. Seeding the last stage with the signal and compensating the idler profile should be avoided because of the lack of adequate optical components in the LWIR. The signal's angular dispersion could be compensated by gratings or prisms with appropriate coatings and low absorption. However, this could introduce large amounts of dispersion. Also, a deformable mirror is one way to create a round beam profile.

In the spatial domain, walk-off exists for collinear and non-collinear geometry limiting the interaction length. The pulses separate over the propagation distance as the birefringence leads to a Poynting vector walk-off of the extraordinary pulses. For type I and type II phase matching schemes, at least one beam is polarized in extraordinary direction. This is the spatial equivalent to the temporal walk-off, mentioned in sec. 3.4.1. The walk-off angle, quantifying the strength of this effect, is in GaSe much higher than in $ZnGeP_2$. In a 2 mm thick GaSe crystal, the lateral walk-off amounts to 120 µm for the pump and the idler and separate from the signal over the propagation distance. Hence, if utilizing pulses with beam diameters approaching this walk-off difference, this can lead to a reduced interaction length. Ideally, the birefringent walk-off can be compensated by the non-collinear walk-off, as for BBO [88], which is unfortunately not possible for LWIR pulses in GaSe.

The extraordinary refractive index leads to a tilted pulse front which needs to be considered when using this beam for the next parametric stage or might require correction. For ideal parametric interaction, the wavefront curvature of the seed and the pump must coincide and should be parallel. The strength of this effect on the parametric interaction length depends on the beam profile and the pulse duration. Another disadvantage when working with GaSe as the nonlinear crystal is the necessity of tilting the crystal by almost 30° externally and the corresponding internal pulse profiles. When using GaSe, the pulse profile inside the crystal is elliptical. Usually, nonlinear crystals are cut to the PM angle to avoid this situation, but this is simply not possible in GaSe. For an internal angle of 12.2°, the beam profile is 20 % larger in one direction than in the other and the idler profile is expected to be elliptical as well.

3.3 Temporal dispersion management

The phase matching geometry, the group velocity of the involved pulses and their spectral characteristics influence the efficiency of the parametric process, but also the temporal shape and phase control play a key role in chirped pulse amplification. The output energy and spectrum of an OPCPA is strongly influenced by the pulse duration of the involved pulses. The pulse duration can be modified by introducing a specific phase, see sec. 2.2, with different stretching and compression schemes, applicable to different power applications. Proper phase management is one of the main challenges to reach the femtosecond regime. In the experiment, dispersion stems from different optical components and can be divided into three groups namely material dispersion, geometrical dispersion and dispersion due to interference effects. Different techniques imprint opposite signs of second and third order of polynomial phases on the pulses as will be discussed in this section. In chirped pulse amplification, the pulses are stretched prior to amplification and recompressed afterwards, see sec. 2.5.1. For long pulses, it might be sufficient to compensate the second order only, however, few-cycle pulses also require the compensation of the third order phases.

Typically the front-end provides signal pulses with femtosecond duration, which are matched to the pump pulse duration in the picosecond range by introducing different amounts of second and third order phases. A pulse is said to be positively chirped or normally dispersed, if the blue spectral components are trailing ahead at the front of the pulse and the red components at the tail. Spatial dispersion stemming from the phase matching properties are also discussed in this section.

3.3.1 Dispersion management in bulk material

Bulk dispersion is stemming from the intrinsic property that the refractive index of a material depends on the frequency. Due to the change of index of refraction, in most materials red frequency components travel faster than the blue which is referred to as normal dispersion. The group velocity dispersion and the third-order dispersion, defined in eq. 2.12, sec. 2.2, are plotted for typical infrared materials transparent beyond 2 µm in Fig. 3.12. While group velocity dispersion (GVD) is positive for germanium (Ge) and silicon (Si), it is negative for sapphire (Al_2O_3), zinc selenide (ZnSe), barium fluoride (BaF_2), calcium fluoride (CaF_2) or magnesium fluoride (MgF_2). The third-order dispersion (TOD) is always positive for the relevant materials. As soon as the wavelength approaches the transparency limit, GVD and TOD values become very large as it is the case for sapphire beyond 5 µm or CaF_2 beyond 8 µm.

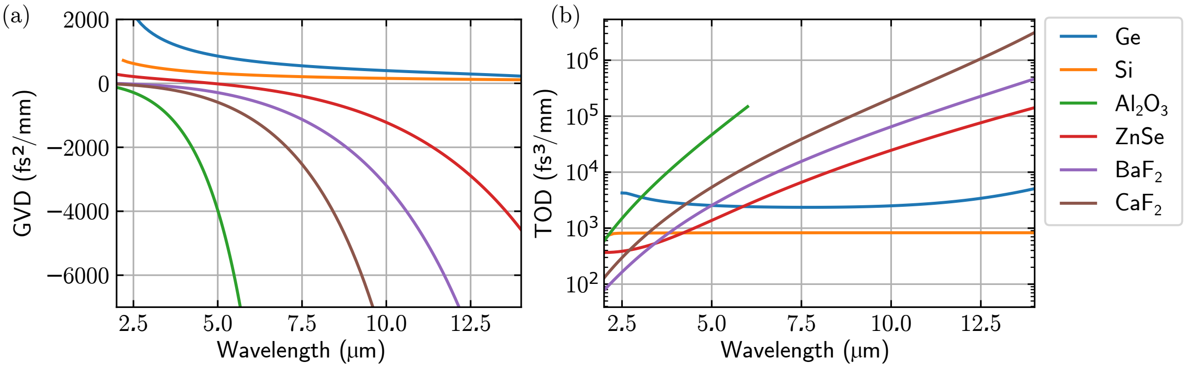

Figure 3.12: Group velocity dispersion (GVD) and third-order dispersion (TOD) values for typical infrared materials transparent beyond 2 µm.

In the context of OPCPA, seed pulse stretching in bulk material is very straight forward, easily adjustable by the thickness of the substrate and almost lossless. It allows to adjust the pulse duration of the signal or the idler in every parametric stage individually. In the parametric process, the sign of the group delay dispersion (GDD) is inverted between signal and idler, but has the same sign for the TOD. Hence, the GDD of the idler pulse can usually be compensated by the same bulk material subsequent to the amplification process if it is still transparent in this frequency range, but the TOD sums up. Compensation of the TOD of the order of 10^6 is typical.

Another factor is the nonlinear refractive index n_2 which is sensitive to the intensity of the pulse and can lead to severe pulse distortion, see sec 2.6. Materials such as Si or Ge exhibit high n_2 value and are restricted to low power application, therefore using them with µJ-fs-pulses is not advisable. In contrast, the materials BaF$_2$ and CaF$_2$ are known for their low nonlinearity and wide transparency range and appear well suited for MWIR and LWIR applications. For most infrared materials, the nonlinear refractive index is known in the near-IR spectral range and extrapolated for longer wavelengths. Deviations from the extrapolation are expectable. For the LWIR, the n_2 data availability is quasi non-existent as of the lack of high-energy laser sources in this spectral range.

The usage of transmissive materials for stretching and compression is limited by absorption and nonlinear effects, such as self-focussing, two-photon absorption, ionization or filamentation. Additionally, the introduced third-order dispersion of typical infrared materials is high for LWIR pulses and needs to be compensated with different components.

3.3.2 Compensation of higher-order phases

When bulk material is used for stretching the signal pulses prior to amplification, the idler and signal after the parametric process require compensation of second- and third order phases in order to reach the Fourier limit. If the signal is negatively chirped by the bulk material, the signal requires positive GDD and negative TOD to compensate the phase difference. The idler, however, requires negative GDD and negative TOD. Common schemes for spectral phase manipulation are grating or prism pairs, chirped mirrors, adaptive pulse shapers with deformable mirror or programmable dispersive filter [75]. A selection of common dispersive configurations are shown in Tab. 3.3 for LWIR pulses. It summarizes different compressor and stretcher designs exploiting refraction and diffraction from gratings or prisms. The optical

components in the LWIR spectral range are however very limited.
The angular dispersion resulting from the refraction of a prism always leads to negative GDD no matter the material dispersion [89]. A prism compressor is often the cheapest way to introduce a reasonable amount of GDD, if the GDD is too large for being compensated by chirped mirrors. In a prism compressor, the GDD of the material and the angular dispersion sum up and allow for the choice between positive or negative GDD. The total GDD can be continuously changed by moving the prisms along the axis perpendicular to its base [90]. Grating pairs introduce much larger amounts of GDD, but the shortest distance between the gratings might be limited by the geometry of the compressor. In both compressor types, the TOD cannot be controlled separately from the GDD. More sophisticated arrangements using a GRISM compressor consisting of a grating-prism combination allow for different GDD to TOD ratios [91], but so far only available in the near-IR. Using additional lenses acting as a Fourier transformation allows to choose between positive and negative second-order dispersion [92]. The Martinez compressor has been used for the signal compression in sec. 7.3. Inserting phase masks into the Fourier-plane of a 4-f design enables improved phase control [93].

The easiest way to imprint an almost arbitrary phase on the signal seed pulse is the use of a spatial-light modulator (SLM) or an acousto-optic programmable dispersive filter (AOPDF). Third-order phase compensation not achievable with bulk material or stretcher/compressor schemes is adjusted at any moment. These devices are however limited to low power applications and have throughput of $< 50\,\%$ for the SLM and $< 30\,\%$ for the AOPDF (Dazzler, Fastlite) which makes them usable only for seed beams. These devices exist only up to 7 µm. Depending on the maturity of the existing lasers, different optical components exist with varying quality and reliability. For the idler pulse in the LWIR, gratings with 80 % diffraction efficiency are commercially available, but the damage threshold is specified for ns-pulses. In a prism and grating pair arrangement, the pulse must traverse four optical components and as a result, losses and poor anti-reflection coatings sum up to rather low throughput. Anti-reflection coatings in that wavelength range are not always common and exploratory, i.e. the dielectric beam splitter for separating the LWIR idler from the pump and the signal in chap. 7 is customized. As anti-reflection coatings consist of coating layers with a thickness of the order of $\lambda/2$ and multiples layers are necessary to ensure high reflectivity (or high transmission), coating structures for LWIR pulses have several µm thickness. To the best of my knowledge, I am not aware of the existence of chirped mirrors in the LWIR spectral range. At 10.6 µm, coatings for CO_2 lasers are developed, designed for CW applications or ns-pulses with rather narrow spectral width and the information about their performance with femtosecond-microjoule pulses is little. The most reliable compression scheme in the LWIR is using bulk material. The transmission of bulk CaF_2 significantly decreases beyond 8 µm and that of BaF_2 at 10 µm. Only ZnSe transmits the whole spectrum up to 18 µm with $> 90\,\%$ but with the drawback of having a comparably high nonlinear refractive index. It is hence necessary to work with large beam sizes.

Eventually, indirect pulse shaping of the signal is the best practice of creating idler pulses close to the Fourier limit. This is how it is done in this work for the MWIR and LWIR OPCPA. The coarse stretching of the signal pulses is done with bulk material and the fine tuning with

	Bulk ZnSe $L = 15\,\mathrm{mm}$	Prism pair ZnSe $D = 100\,\mathrm{mm}$	Grating pair $D = 20\,\mathrm{mm}, \beta = 27°$ 100 lines/mm	Chirped mirror per reflection	SLM / AOPDF @2.4 µm
Efficiency	97 %	60 %	24 %	70 %	$50/<30\,\%$
GDD (fs^2)	-31×10^3	-118×10^3	2.91×10^6	<3 µm	50×10^3
TOD (fs^3)	740×10^3	4.0×10^6	136×10^6	only	2×10^6
GDD sign	−/+	−/+	−/+	±	±
TOD sign	+	+/−	+/−	±	±

Table 3.3: Possible dispersion compensation configurations and elements for MWIR/LWIR pulses. The efficiency and GDD and TOD numbers rely on commercially available components and coatings. The values for the spatial light modulator (SLM) and the acousto-optic programmable dispersive filter (AOPDF) are given for 2 µm pulses. L: thickness of optical element, D: distance between prism (at Brewster angle) or grating, β angle of incidence on grating.

an SLM or AOPDF. Signal pulses with negative GDD lead to idler pulses with positive GDD. If using the idler to seed one parametric stage, it needs to be positively chirped and only silicon and germanium exhibit positive GDD in this spectral range. These materials have a large nonlinear refractive index which might cause unwanted beam distortion. For the same reason, introducing positive GDD on the signal requiring the use of the same materials to recompress the idler seems most undesirable. Consequently, negative GDD is imprinted on the signal. The introduced bulk material must amount to a TOD value that is still possible to compensate with an SLM or AOPDF.

3.4 Bandwidth and efficiency optimization

Based on the intrinsic properties of the nonlinear interactions in GaSe and $ZnGeP_2$ for infrared OPCPA, optimization of the pump and the signal seed pulses can tremendously improve the overall performance of the system. The wavevector mismatch depending on the involved wavelength components reduces the parametric gain and deserves special attention. The large potential in the selection of the pump and the signal wavelengths aiming for a specific idler wavelength, as well as the influence of their energy ratio and the refractive indices are discussed in this section. The temporal and spatial overlap of the pulses determine the level of depletion leave room for improvement.

3.4.1 Parametric Gain

Most MWIR and LWIR OPCPA systems rely on driver front-ends in the near-IR region, such as Ti:Sa emitting at 800 nm, Yb:YAG at 1.03 µm, Nd:YAG at 1.06 µm or Er^{3+} fibre lasers at 1.5 µm. These laser systems are commercially available and have been proven reliable sources for many years. However, it is not advantageous to use these lasers as drivers for few-cycle OPCPA systems beyond 4 µm.

First of all, the number of nonlinear crystals which are transmissive for a near-infrared pump wavelength as well as for idler wavelengths beyond 4 µm is very limited (Fig. 3.2). $ZnGeP_2$, for example, cannot be used with a 1 µm pump. Some of the new barium based nonlinear crystals could be used instead, or GaSe. If the pump wavelength has an energy close to half the bandgap energy of the crystal $E_g/2 = hc/\lambda$, the probability of two-photon absorption (TPA) increases. If this phenomenon becomes too prominent, it causes damages in the crystal and limits the maximum applicable pump energy. In the case of GaSe, the bandgap is $E_g = 2.1\,\text{eV}$ which corresponds to $\lambda = 590\,\text{nm}$ and TPA is expected to be large for NIR wavelengths. As a consequence, GaSe should have a much lower damage threshold for the pump wavelength of $1\,\mu\text{m}$ compared to $2\,\mu\text{m}$.

The parametric gain determines the amplification of the signal and the idler pulses and depends on the pump intensity I_p, the effective nonlinearity d_{eff}, the input pulses and their refractive indices, see eq. 2.32. The wavevector mismatching can, for sufficient phase matching conditions, be neglected, but plays an important role in GaSe as the group velocity mismatch between pump, signal and the corresponding LWIR idler is large (discussed in sec. 3.2.2). The parametric gain takes into account the unfavourable signal-to-idler ratio for LWIR pulses which is neglected if only considering the sinc^2 parametric coefficient term and provides a broader picture of the amplification process. This parameter quantifies the gain of the different spectral components in the parametric interaction.
Fig. 3.13 and 3.14 show the parametric gain as a function of the signal and the idler wavelength for a $2.05\,\mu\text{m}$ pump, for different peak intensities and crystal thicknesses. The gain scales as $\Gamma \propto d_{\text{eff}}^2 I_p$ (eq. 2.33) and the peak intensity and crystal thickness combinations are chosen such that they reach the same gain value for $\Delta k = 0$. If the crystal length is divided by two, four times the pump intensity is necessary to reach the same value (the same applies for Fig. 3.15 and 3.16). Note that the peak intensity of a laser pulse describes the highest intensity in time and space. Namely, the here provided parametric gain is valid for the spatio-temporal center of the pulse and decreases towards the outer parts.
Longer nonlinear crystals decrease significantly the necessary pump intensity. In return, for non-zero wavevector matching, the reduced pump intensity comes at the expense of the bandwidth. In GaSe for type II PM at 12.17° (Fig. 3.13), the wavelength of $2.53\,\mu\text{m}$ experiences the highest gain for a 2 mm crystal and the gain favours the amplification of wavelength components beyond $2.4\,\mu\text{m}$. The better pump-to-signal ratio for longer signal wavelengths cancels with the group velocity mismatch, shown as the blue dotted line in Fig. 3.14. The GVM has its minimum value at an idler wavelength of $12.5\,\mu\text{m}$, where the parametric gain is not influenced by wavevector mismatch and decreases for all other wavelengths.

In order to see the difference of the parametric gain coefficient for another pump wavelength, Fig. 3.15 and 3.16 show the parametric gain for the signal and idler pulses for the same peak intensity and crystal thickness, but for a $1.03\,\mu\text{m}$ pump at adequate PM conditions. The supported bandwidth narrows by a factor of 5 for the crystals of 0.5 mm and 2 mm. For a $1\,\mu\text{m}$ pump, the wavevector mismatch Δk is 100 times higher than for $2\,\mu\text{m}$ (Fig. 3.16, blue dotted line) which is the reason for this behaviour. The calculated parametric gain is a factor 10 higher than for a $2\,\mu\text{m}$ pump, but at this point it is worth mentioning that the damage threshold for a $1\,\mu\text{m}$ pulse should be much smaller because of two-photon absorption close the band gap of GaSe. Depending on the light-induced damage threshold (LIDT) damage threshold it is questionable whether or not the parametric gain is still higher than at $2\,\mu\text{m}$ pump wavelength. The here assumed intensities were used for comparison purposes only.

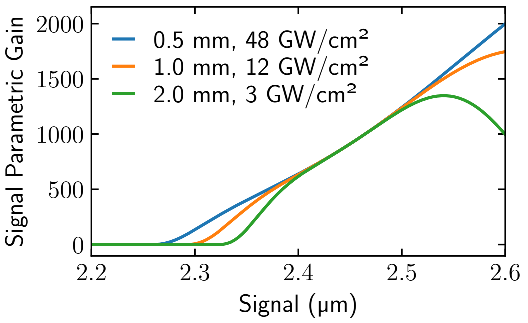

Figure 3.13: Signal Parametric Gain in GaSe for 12.17° in type II PM, pump at 2.05 µm with $d_{eff} = 53.7$ pm/V.

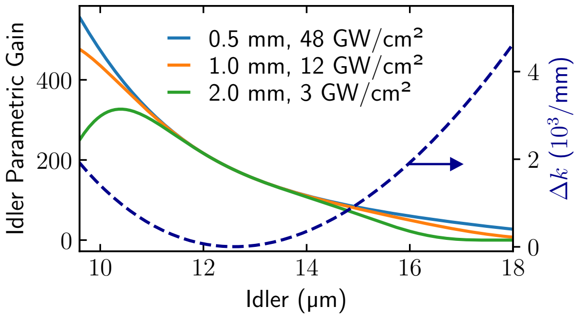

Figure 3.14: Idler Parametric Gain in GaSe for 12.17° in type II PM, pump at 2.05 µm with $d_{eff} = 53.7$ pm/V.

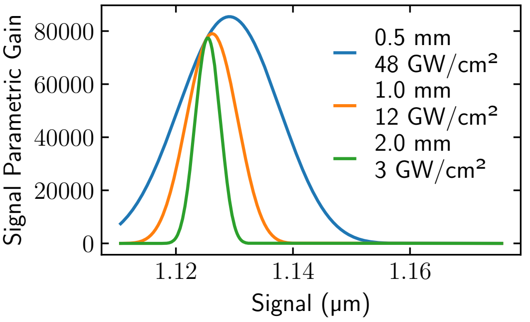

Figure 3.15: Signal Parametric Gain in GaSe for 14.1° in type II PM, pump at 1.03 µm with $d_{eff} = 56.2$ pm/V.

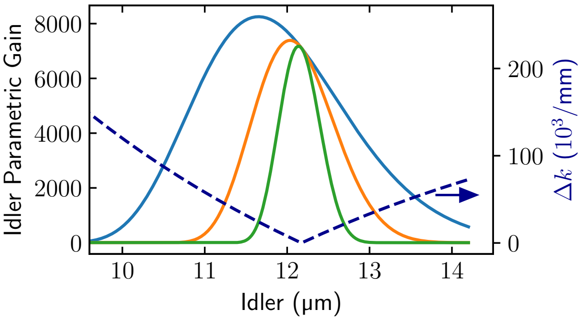

Figure 3.16: Idler Parametric Gain in GaSe for 14.1° in type II PM, pump at 1.03 µm with $d_{eff} = 56.2$ pm/V. Legend of Fig. 3.15 applies.

Nevertheless, this spectral analysis underlines the advantages of a 2 µm over a near-IR pump source to ensure a broad idler bandwidth as the first amplification stage in our system requires a 2 mm GaSe crystal to reach sufficient gain.

It is also possible to exploit the gain coefficient by using wavelengths that have a more favourable group velocity match and energy ratio. Pumping with larger wavelengths, for example, seems advantageous at the first sight. Fig. 3.17 shows the parametric coefficient for a pump spectral range of 100 nm and signal spectral range of 300 nm centred at 2.4 µm. This is compared to the same bandwidth of pump and signal but shifted in frequency aiming for the same idler wavelength. Fig. 3.18 shows the conversion efficiency at 12.29°. The comparison between these two plots suggests a broader signal bandwidth if pumped at 2.25 µm which seem to be advantageous. However, the corresponding idler bandwidth in Fig. 3.19 is shifted towards shorter wavelengths and is only marginally broader for the 2.25 µm pump than for the 2.05 µm pump. In conclusion, in terms of idler bandwidth the effort of shifting the pump wavelength to longer wavelengths might not outweight the slightly broader idler pulse shifted to shorter wavelengths.

3.4.2 Pulse duration ratio between signal to pump

In an OPCPA, the ratio between the signal and the pump pulse duration has a huge impact on the amplification characteristics (compare also with sec. 2.5.1 and 3.3). The temporal overlap determines, on one hand, the maximum output energy and, on the other hand, the

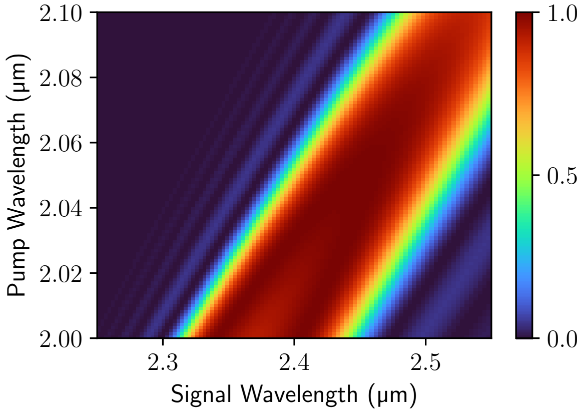

Figure 3.17: Parametric coefficient for type II phase matching in 2 mm GaSe at 12.17°.

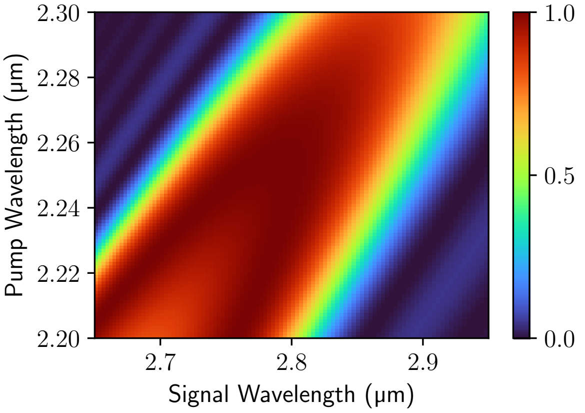

Figure 3.18: Parametric coefficient for type II phase matching in 2 mm GaSe at 12.29°.

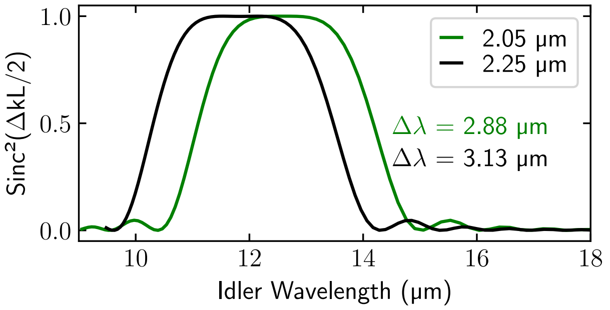

Figure 3.19: Direct comparison of type II phase matching in GaSe for the pump wavelength at 2.05 µm at 12.17° and 2.25 µm at 12.29°. This graph is the horizontal cross section of Fig. 3.17 and 3.18.

output spectrum. It affects which spectral components get amplified, governs the spectral narrowing and eventually sets the Fourier limit for the compressed idler pulses.

A LWIR OPCPA containing GaSe is simulated for experimentally realistic parameters. For all simulations, the pump duration is set to 3.0 ps with 3 nm bandwidth at 2.05 µm and with a Gaussian pulse shape, which corresponds to the experimental implementation. The input parameters are chosen according to the system parameters, introduced in the next chapters. The pump duration for the implemented system is set by the Treacy-type grating compressor after amplification. The signal seed duration, however, can be modified by introducing bulk material in the beam path or by imprinting a polynomial phase with the AOPDF (Dazzler, Fastlite) prior to initial amplification.

Fig. 3.20 shows the signal bandwidth in percent with respect to the seed bandwidth and the associated conversion efficiency for different ratios of pump τ_p to signal τ_s pulse durations, for the high (a) and low (c) gain regime. The high gain regime (a) is simulated as it has been implemented in OPA 1 of Ch. 7 where a 1 nJ seed pulse is amplified under type II phase matching at 12.17° in 2 mm GaSe. In Fig. 3.20 (c), OPA 2 of Ch. 7 is realized in a 1 mm GaSe crystal under the same phase matching conditions for a 15 µJ signal energy of the previous amplification stages. In (b) the spectrum corresponding to (a) is shown for the signal pulse. While the signal bandwidth decreases with the ratio ${}^{\tau_s}/_{\tau_p}$, the total conversion efficiency $(E_s + E_i)/E_p$ increases and reaches saturation at ${}^{\tau_s}/_{\tau_p} = 1$. It is atypical that the signal bandwidth is the broadest for the shortest pulse duration. This can partly be explained by a mixture between the more favourable gain coefficient and phase matching conditions towards longer signal wavelengths (Fig. 3.13) and saturation effects. Normally, one would expect a behaviour as it is shown for high gain in $ZnGeP_2$ in Fig. 3.21 (a) with significant phase matching bandwidth. In this case, under ideal conditions the parametric amplification reproduces the shape of the input seed spectrum. This graph shows also the signal bandwidth and conversion efficiency for different pump to signal pulse ratios for 10 GW/cm^2 in 2 mm $ZnGeP_2$, as it is implemented in OPA 1 in Ch. 6. The signal bandwidth has a clear maximum at ${}^{\tau_s}/_{\tau_p} = 0.25$ and decreases for larger ratio. Also, the conversion efficiency has a maximum at ${}^{\tau_s}/_{\tau_p} = 0.6$ and decreases afterwards.

(a) high gain (b) high gain

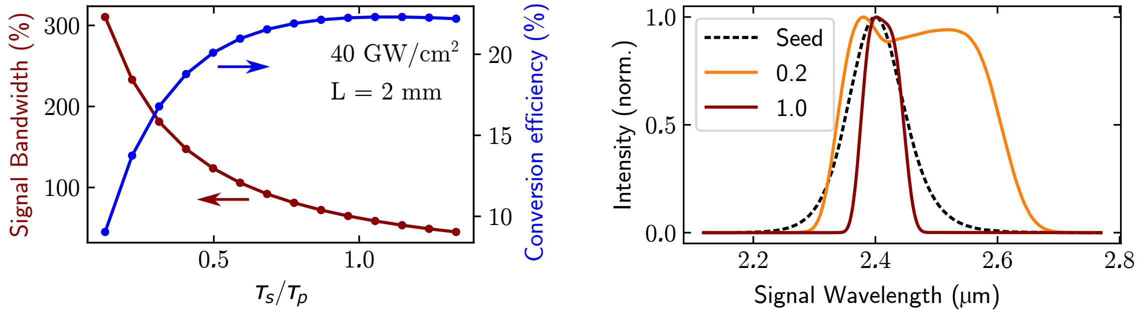

(c) low gain (d) high gain

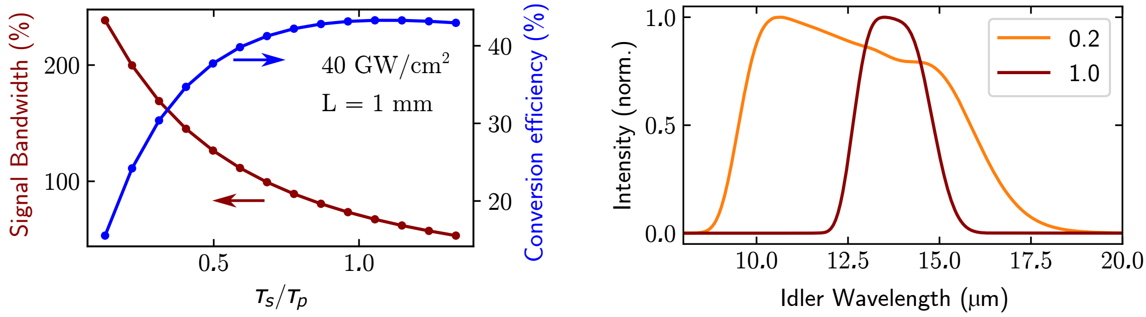

Figure 3.20: The Simulation results of the LWIR OPCPA: high gain (a,b,d) in 2 mm GaSe with $E_p = 321\,\mu J$, seeded with $E_s = 1\,nJ$ and (c) low gain amplification in 1 mm GaSe with $E_p = 1.6\,mJ$, seeded with $E_s = 15\,\mu J$. (a,c) output bandwidth in percent from input bandwidth and conversion efficiency in dependence of the temporal signal to pump ratio ${}^{\tau_s}/_{\tau_p}$, and corresponding signal (b) and idler (d) spectrum for two ${}^{\tau_s}/_{\tau_p}$ values.

(a) (b)

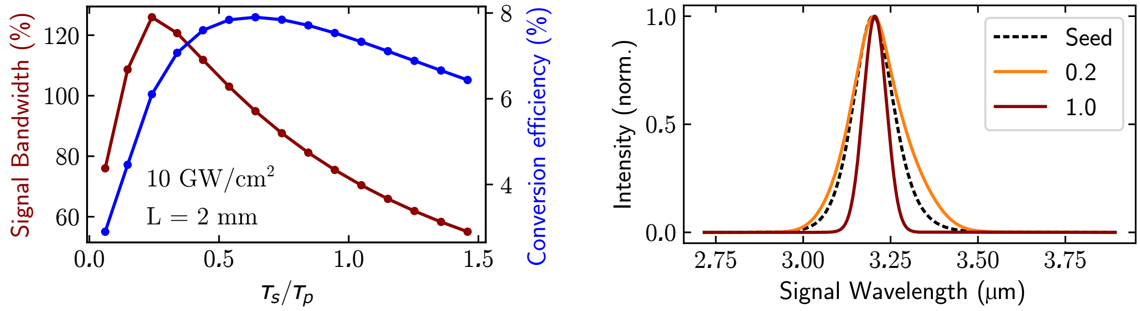

Figure 3.21: Simulation results of MWIR OPCPA: (a) in 2 mm $ZnGeP_2$ with 325 µJ pump energy, seeded with 2.5 nJ signal showing bandwidth and conversion efficiency in dependence of the temporal signal to pump ratio ${}^{\tau_s}/_{\tau_p}$, and (b) corresponding signal spectrum.

In the right columns of Fig. 3.20(b,d) and Fig. 3.21(b), the corresponding spectra for the ratios $\tau_s/\tau_p = 0.2$ and 1 are shown. For the LWIR OPCPA, the signal spectrum in Fig. 3.20(b) broadens towards longer wavelengths where the spectral wings have very little seed energy, as there is less group velocity mismatch and a higher parametric gain. Equivalently, the idler spectrum (Fig. 3.20(d)) shift towards shorter wavelengths. This frequency shift is not observed in the MWIR OPCPA in $ZnGeP_2$ (Fig. 3.21(b)) which provides negligible group velocity mismatch and a much broader phase matching bandwidth. The signal spectrum symmetrically broadens around the central seed wavelength and shows no tendency of shifting to lower or higher frequencies which is expected with the given phase matching properties.

The direct comparison between the nonlinear crystals $ZnGeP_2$ and GaSe shows once again that the parametric amplification behaves differently. While the balance between bandwidth and conversion efficiency of the system is quite clear for $ZnGeP_2$, the ratio $\tau_s/\tau_p < 0.5$ offers the opportunity of generating a much broader spectrally shifted spectrum at the expense of conversion efficiency. The latter could be compensated with an additional amplification stage. Still, I am sceptical whether the broad spectrum with short pulses allows for Fourier limited pulse durations of the idler pulse, possibly lacking sufficient dispersion control after the amplification process.

3.4.3 Spatio-temporal pulse shape optimization

The conversion efficiency of an OPCPA is strongly limited by the backconversion. The intensity at the center of the pump pulse is much higher and leads to a higher parametric gain. This part is starting backconversion before the wings have reached saturation. Hence, pump depletion occurs in the central part earlier than at the outer parts (compare Fig. 2.4 in sec. 2.5). This is a spatio-temporal phenomena. When designing an OPCPA, gain saturation and reconversion need to be balanced. Consequently, the ultimate goal is the homogeneous depletion in time and space.

Typically, the flat-top is approximated with a 10^{th}-order Gaussian beam shape. Flat-top beam shapes have been proposed to achieve uniform depletion of the pump and the effects of the use of high-order super-Gaussian shapes for the pump pulse have been studied theoretically [38] and demonstrated experimentally [71]. Very recently, a mid-IR OPCPA at 3 µm has been successfully implemented [94]. They have shown that spatio-temporal shaping reduces the gain narrowing and maximizes the conversion efficiency. Another advantage of the flat-top beam profile is that for the same energy, the peak intensity is reduced. It is therefore possible to increase the pump energy while still staying below the damage threshold. Making use of the residual pump and reusing it for a following OPA stage can show a significant overall increase of the pump-to-idler efficiency [95].

Spatio-temporal shaping of the pump pulse is simulated for the LWIR OPCPA in GaSe using *Sisyfos* [81], see Fig. 3.22. This simulation assumes input parameter as given by the employed Cr:ZnS front-end and pump pulse of this system (see Ch. 4 and 5). The left column shows the temporal evolution, and the right column the spatial evolution. The upper part (a-d) shows a Gaussian pulse spatial and temporal profile of second order for the pump and the seed pulses. The first row in Fig. 3.22 shows the parametric amplification in GaSe for 12.17°

pump	Gauss Order 2			Gauss Order 10		
	E_{in}	E_{out}		E_{in}	E_{out}	
		intern	extern		intern	extern
	OPA1 with 2 mm GaSe					
pump	401 µJ	324 µJ	259 µJ	595 µJ	361 µJ	289 µJ
signal	1 nJ	64 µJ	51 µJ	1 nJ	198 µJ	158 µJ
idler		12 µJ	9.6 µJ		35 µJ	28 µJ
pump-to-idler efficiency			3.0 %			5.9 %
	OPA2 with 1 mm GaSe					
pump	214 µJ	176 µJ	141 µJ	235 µJ	185 µJ	148 µJ
signal	36 µJ	69 µJ	55 µJ	115 µJ	155 µJ	124 µJ
idler		6 µJ	4.8 µJ		8 µJ	6.4 µJ
pump-to-idler efficiency			1.5 %			1.3 %

Table 3.4: Simulation of a two stage OPCPA in GaSe with Sisyfos. Upper part (OPA1): 2 mm GaSe with 50 GW/cm^2 pump intensity, lower part (OPA2): 1 mm GaSe with recycled pump (Fresnel losses included). The signal seed has a Gaussian shape of order 2, whereas the pump is for the right hand side spatio-temporally shaped to a 10$^{\text{th}}$ order Gaussian.

under type II phase matching with a peak power of 50 GW/cm^2, which is the experimental lower damage threshold limit. In total, the pump energy is 401 µJ and the signal seed 1 nJ. The second row (c,d) is using the residual pump of the first stage and the amplified signal in 1 mm GaSe for a second amplification process. The input energies have been corrected by the expected Fresnel losses ($T_p = 80\,\% + 84\,\%$, $T_s = 80\,\% + 73\,\%$) due to internal and external reflections. The same calculation is done for a spatio-temporal Gauss pulse of 10$^{\text{th}}$ order in time and space with 50 GW/cm^2 and 595 µJ under the same PM conditions, shown in Fig. 3.22(e-h). The seed pulse of the signal remain the same.

Tab. 3.4 summarizes the energies of the pump, signal and idler pulses of Fig. 3.22. It shows the input energies for the simulation as well as the output energies, providing a second value corrected by 20 % internal losses for all pulses at the second surface of the GaSe. The upper part provides the values for the 1$^{\text{st}}$ OPA stage Fig. 3.22(a,b,e,f) and the lower part for the 2$^{\text{nd}}$ stage with recycled pump Fig. 3.22(c,d,g,h). The analysis confirms the improved conversion efficiency for a flat-top pump beam. For the first stage, the internal pump-to-idler conversion efficiency of the flat-top beam of 5.9 % is almost a factor 2 larger than for a 2$^{\text{nd}}$ order Gaussian pump beam reaching 3.0 %.
A closer look to the recycled pump in the 2$^{\text{nd}}$ OPA stage with 1 mm GaSe, however, leads to an alternative conclusion concerning the effectiveness of pump recycling. The Fresnel losses of the pump and the signal reduce the output energy of the system as this parametric stage is not reaching the OPA regime or exponential gain (compare to Sec. 2.5). The output idler energy is reduced by a factor 2 or lower. As a conclusion, pump recycling should be omitted in GaSe, if not significantly more pump energy is available.

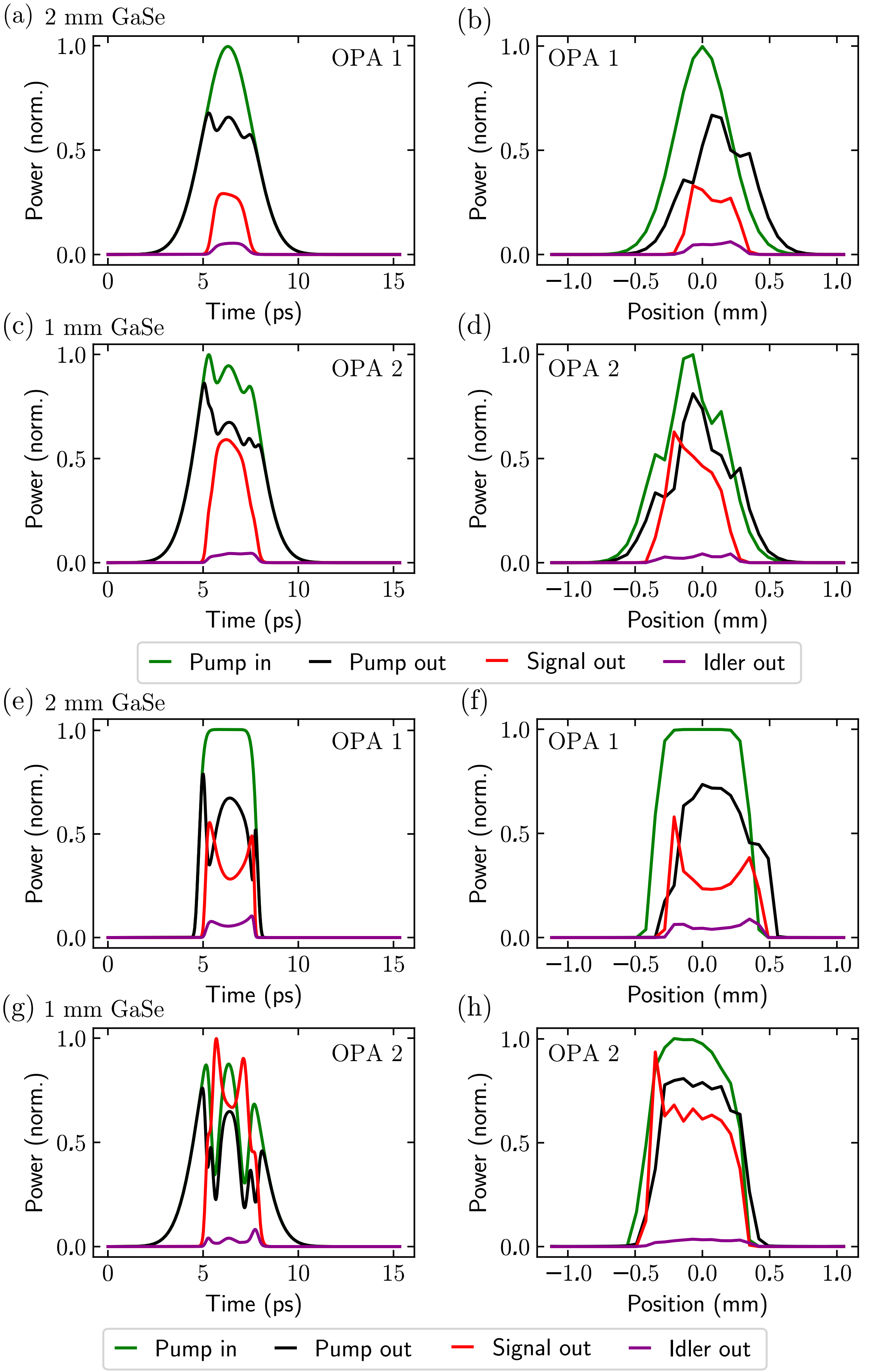

Figure 3.22: Simulation with Sisyfos of two stage GaSe ($d_{\mathrm{eff}} = 30\,\mathrm{pm/V}$) OPCPA for LWIR generation in 2 mm in OPA 1 ((a)(b),(e)(f)), and using the depleted pump in OPA 2 with 1 mm GaSe ((c)(d),(g)(h)), pump at 2.05 µm and signal at 2.4 µm. Upper part: with 2nd order Gaussian beam profile, lower part: with 10th order. Left column: temporal profile, right column: spatial profile.

3.5 Summary for LWIR OPCPA in GaSe

This chapter has summarized the properties of the nonlinear crystal GaSe for the generation for LWIR pulses using OPCPA. The crystal has low absorption between 0.65 and 18 µm and a comparably high effective nonlinearity of $d_{\mathrm{eff}} = 56.4\,\mathrm{pm/V}$ [96]. However, some design criteria differ from OPCPA implementations with other nonlinear crystals such as $\mathrm{ZnGeP_2}$. The analysis takes into account a pump wavelength of 2.05 µm and a signal at 2.4 µm for the LWIR and at 3.2 µm for the MWIR.

The non-collinear geometry reduces the bandwidth supported by the phase matching for LWIR pulses, which is opposite of similar approaches. This is mainly due to group velocity mismatch which plays an important role in long crystals. Due to the commercial availability, crystal thicknesses between 0.5 and 2 mm are considered. It has been shown that a 2 µm pump has a superior performance than a pump at 1 µm in terms of bandwidth and applicable pump energy. The cleaving angle of GaSe is dictated by the crystal structure and the crystal cannot be cut to the desired phase matching angle. Therefore, the crystal needs to be tilted for the parametric process which leads to internally elliptic beam profiles if the outer profile is circular. Coating of the crystal surface is not possible and the parametric process suffers from Fresnel losses at the crystal surface for all beams. On one side, there is less pump and seed energy available inside the crystal, and 20 % of the amplified signal and idler energy is lost due to internal reflection. Above 10 µm, type II phase matching provides a larger bandwidth than type I, but leads to a large walk-off angle of 3.4° for the pump and the idler pulses, both polarized in extraordinary direction. In a 2 mm crystal, this corresponds to a lateral displacement of 120 µm. Beam sizes should be chosen accordingly.
Contrary to MWIR parametric generation in $\mathrm{ZnGeP_2}$, shorter signal pulse durations in GaSe lead to a broader amplification spectrum. This comes at the expense of conversion efficiency. This property can potentially be used to broaden the signal spectrum in a first stage with a low amplification factor, and aiming for large gain in the subsequent stages with short crystals, provided there is enough pump energy available.

The MWIR OPCPA is built according to the design criteria in [80] and the results presented in Ch. 6. The first stage is built in non-collinear configuration in 2 mm $\mathrm{ZnGeP_2}$ at an internal non-collinear angle of 2° and the second stage is built in collinear geometry, both seeded with the signal. The total available pump energy is used staying below $10\,\mathrm{GW/cm^2}$ in every parametric stage.

4

Regenerative amplifier based on Ho:YLF

The maximum output energy of an OPCPA is, among other parameters, limited by the available pump energy. The pulse duration of the pump source of OPCPA systems is typically in the picosecond time range. For the mid- and long-wave infrared region, pump lasers beyond 2 µm are advantageous, as discussed in the previous chapter. Holmium doped amplifiers appear well suited for high power applications as demonstrated in [97–99]. They offer long upper state lifetimes of a few milliseconds, high stimulated emission cross sections and a low quantum defect. These characteristics enable kHz repetition rates with millijoule energies and picosecond pulse durations.

The host crystals Yttrium Lithium Fluoride ($LiYF_4$, YLF) and Yttrium Aluminium Garnet ($Y_3Al_5O_{12}$, YAG) have been proven suitable lattice structures for gain materials, enabling also doping with holmium ions and lasing in the infrared region. The doping ion in the crystal determines the absorption and emission bands of the material. In both crystal structures, the yttrium ions are partly replaced by the laser active rare earth ions without significant lattice structure change. The two crystals have different amplification characteristics and differ in their material type, thermal conductivity, nonlinear refractive index and emission cross section [100, 101]. Holmium doped YLF crystals, amplifying pulses at 2051 nm in π-direction, enable amplification with larger gain and less gain narrowing than holmium doped YAG [99, 102]. YLF is a birefringent crystal and amplifies different wavelength bands in π- and σ-orientation, defined with respect to the c-axis of the crystal. The YLF crystal profits from the lower nonlinear refractive index and a negative thermal lens compared to YAG. There is an emission band at 2051 nm (π-pol.) and a second one at 2061 nm (σ-pol.) with perpendicular polarization direction. Pumping both emission bands results in double pulsing. Hence, the seed pulse must only overlap with one emission band. The birefringent characteristics of Ho:YLF reduce thermally induced depolarization losses which can be a problem in Ho:YAG at high power because of its isotropic crystal structure. This work aims for the amplification in π-direction at 2051 nm in Ho:YLF associated with the $^5I_7 \rightarrow {}^5I_8$ transition.

Regenerative amplifiers (RA) are multipass amplifiers where the seed pulses pass multiple times through the gain medium. This type of amplifier exists in different geometries and allows gain factors of up to 10^7. Nanojoule seed pulses can be amplified to the millijoule level. The following chapter presents the characteristics and technical details of the home-built regenerative amplifier based on a Ho:YLF crystal.
The understanding of the regenerative amplifier was the main work of Lorenz von Grafenstein (former PhD student) who studied the physics and dynamics at different time scales in great detail, please refer to [80]. Based on his work, a simulation programme accurately reproducing the experimental outcome has been developed. This thesis relies for the RA on the previous experimental and simulated findings of his work. This chapter provides an overview of the physical equations underlying the simulation, which I transferred from Matlab to Python code to simulate the current implementation. This programme has been extended with spectral cavity losses and applied to intracavity spectral shaping presented in the last section 4.4 of this chapter. The RA presented here is pumped by a commercial continuous-wave Tm^{3+} fibre laser at 1941 nm emitting pulses up to 14.5 mJ of energy, being compressed down to 2.4 ps and resulting in a peak power exceeding 5.4 GW. The geometry of the RA is adapted from [99, 103] where the femtosecond Er fibre laser front-end was replaced by a Cr:ZnS oscillator.

4.1 Dynamics of high repetition rate regenerative amplifiers

If pulses are amplified in a regenerative amplifier where the repetition rate approaches the inverse of the laser upper level lifetime, the output energy is subject to instabilities. A phenomenon referred to as bifurcation occurs when the amplification of one pulse depends on the previous amplification cycle. On this time scale, the inversion state is not completely reset before the next pulse arrives. High repetition RAs have been thoroughly studied and evaluated, and are summarized in [80, 104–106]. The simulation qualitatively solves the basic relations between the pulse energy, the inversion and the absorbed fluence and thereby provides insights into the spectral and time dependent dynamics. This calculation is applicable to quasi-three and four-level laser systems and hence, to the gain crystal Ho:YLF which is used in this regenerative amplifier. The Ho ions have an upper state lifetime of 10 ms and hence, the repetition rate of 1 kHz falls in the critical range where bifurcation is expected. The large difference between the cavity round-trip time of 11.4 ns and the pulse duration on the ps-time scale allows to separate the simulation into pump and amplification cycles, as the inversion has a negligible effect on the time scale of the seed pulse duration. The intramanifold redistribution process is on the order of ns and fast enough to ensure the same emission and absorption spectrum for every round-trip. The inversion fraction determines the gain spectrum and redistributes between two amplification cycles. Eventually, the simulation can be divided into operation cycles consisting of one pump and one amplification cycle, and repeating the number of round-trips rt. All the following presented equations are in accordance with the definitions of [104].

The extracted fluence can be calculated with the modified Frantz-Nodvik equation applicable to narrowband pulses [107]. The spectral evaluation is split into wavelength intervals of $\delta\lambda = 0.25\,\mathrm{nm}$ to cover the spectral bandwidth of the amplified pulses. The gain crystal with length l is divided into n small slices of $\delta z = {}^{l}\!/_{n}$ to account for the changing pump energy along the crystal length due to absorption. For every crystal slice, the local inversion fraction is calculated from the ratio between the upper laser level local population N_2 and the dopant intensity N_{tot}

$$\beta(z) = \beta_n = \frac{N_2(z,t)}{N_{\mathrm{tot}}}. \tag{4.1}$$

The absorbed pump rate is given by

$$R_n = \frac{I(z)}{h\nu}\sigma_{abs}(\lambda), \tag{4.2}$$

where $I(z)$ is the pump intensity changing along z, h the Planck constant, ν the frequency of the interaction photon and σ_{abs} the wavelength dependent absorption cross section. The absorption of the pump along the propagation direction (longitudinal pumping) changes the pump rate and results in an inhomogeneous inversion along z.

The pump period is governed by the absorbed fluence which is dependent on the local inversion fraction and the pump rate. At the same time the ratio between the stored fluence and the saturation fluence determines the local inversion fraction and dictates the available gain. In the amplification cycle, the change of inversion β_n is calculated from the previous round-trip as the sum over the spectrum

$$\beta_n(\mathrm{rt}+1) = \frac{\sum_{\delta\lambda} J_n(\lambda, rt) - \sum_{\delta\lambda} J_n(\lambda, rt-1)}{J_{\mathrm{sto,tot}}/m} \tag{4.3}$$

assuming intramanifold redistribution on the ns time scale between two passages in the gain crystal. The spectral fluence J of the propagating pulse grows with every slice n as

$$J_{n+1}(\lambda, rt) = J_{sat}(\lambda) \ln\left[1 + G_n(\lambda, rt)\exp\left(\frac{J_n(\lambda, rt)}{J_{sat}(\lambda)} - 1\right)\right] \tag{4.4}$$

with the saturation fluence of

$$J_{sat}(\lambda) = \frac{hc}{\lambda(\sigma_{em}(\lambda) + \sigma_{abs}(\lambda))}, \tag{4.5}$$

where σ_{em} and σ_{abs} are the emission and absorption cross sections. The gain per crystal slice and round-trip is calculated by

$$G_n(\lambda, rt) = \exp\left[\frac{l}{m} N_{\mathrm{tot}} \left(\beta_n(rt)\sigma_{em}(\lambda) - (1-\beta_n(rt))\sigma_{abs}(\lambda)\right)\right]. \tag{4.6}$$

4.2 Simulation of the regenerative amplifier

Bifurcation and deterministic chaos are successfully reproduced by solving the above equations numerically [104] for the experimental input parameters. These two phenomena result in pulse trains where the individual pulses not necessarily have the same energy. This should be

avoided to ensure stable operation. A sufficiently high number of round-trips always leads to a more stable system, but at the same time leads to gain narrowing, a reduced average power and a high B-integral [98]. In this context, it is advisable to keep the number of round-trip as low as possible. Balancing higher seed energy with a lower number of round-trips is one way of ensuring a broader output spectrum and stable operation. As a consequence, the remaining parameters must be chosen such that their interplay leads to an amplification outside the chaotic regime. The optical components in the cavity have a certain damage threshold and limit the highest peak intensity of the amplified pulses. The peak intensity is determined by the intracavity mode size and extracted energy.
The implemented RA is equipped with a Ho:YLF gain crystal pumped in a longitudinal geometry by 50 W of a continuous-wave randomly polarized 1940 nm fibre laser. The laser is focussed to a sub-1 mm spot size inside the gain crystal which determines the maximum stored fluence in the crystal and determines the maximum reachable inversion. The pump volume therefore dictates the maximum extractable energy of the system for a given crystal. The beam waist is determined by the pump size and assumed to be constant over the crystal length as a lens with 1000 mm focal length is used to focus the pump beam, having a Rayleigh length of 15 cm. For too large pump volumes and too poor upper state inversion, the most relevant pulsing scheme is that of double pulsing, where one pulse experiences almost no gain and the next pulse is getting amplified to almost the double value than in the single pulse regime. The double-pulsing regime can often be avoided by reducing the focus of the pump laser. Besides the focus, the seed energy is a tuning parameter. However, the seed energy for the current system is limited by the maximum output power of the 2 µm Tm:fibre pre-amplifier (AdValue) seeded by the front-end oscillator. The number of round-trips is chosen following the aim of keeping the number of round-trips as low as possible for the maximum seed energy of 2.5 nJ.

An ideal configuration is found for 19 round-trips, as presented in Fig. 4.1. The pulse energy is amplified in every pass through the gain crystal until it is saturated, see Fig. 4.1(a). Up to round-trip number 10, the pulse energy is too small to be visible on this scale. At the same time, the inversion fraction and the corresponding gain is depleted until all available energy of the system is extracted, see Fig. 4.1(b). If the gain is equal to one, there is no inversion and gain left. A gain larger than one indicates that not all energy is extracted. Due to gain narrowing, the seed spectrum is broader than the output spectrum (Fig. 4.1(c)). The bandwidth reduces and almost stabilizes after 15 round-trips (Fig. 4.1(d)). On the time scale, the system as it is shown here does not show any sign of chaos and has a stable output energy. The Ho:YLF regenerative amplifier is built following this analysis.

4.3 Technical details

The regenerative amplifier (RA) is built as a ring cavity with double-X geometry. This geometry has been proven stable against pump power fluctuations, thermal lensing and spatial mode instabilities and has achieved larger amplification factors than similar systems with linear geometries [108]. The cavity consists of 6 mirrors and 2 thin-film polarisers (TFP) as in- and output ports, see Fig. 4.2. It additionally comprises a Pockels cell ($RbTiOPO_4$ (RTP)

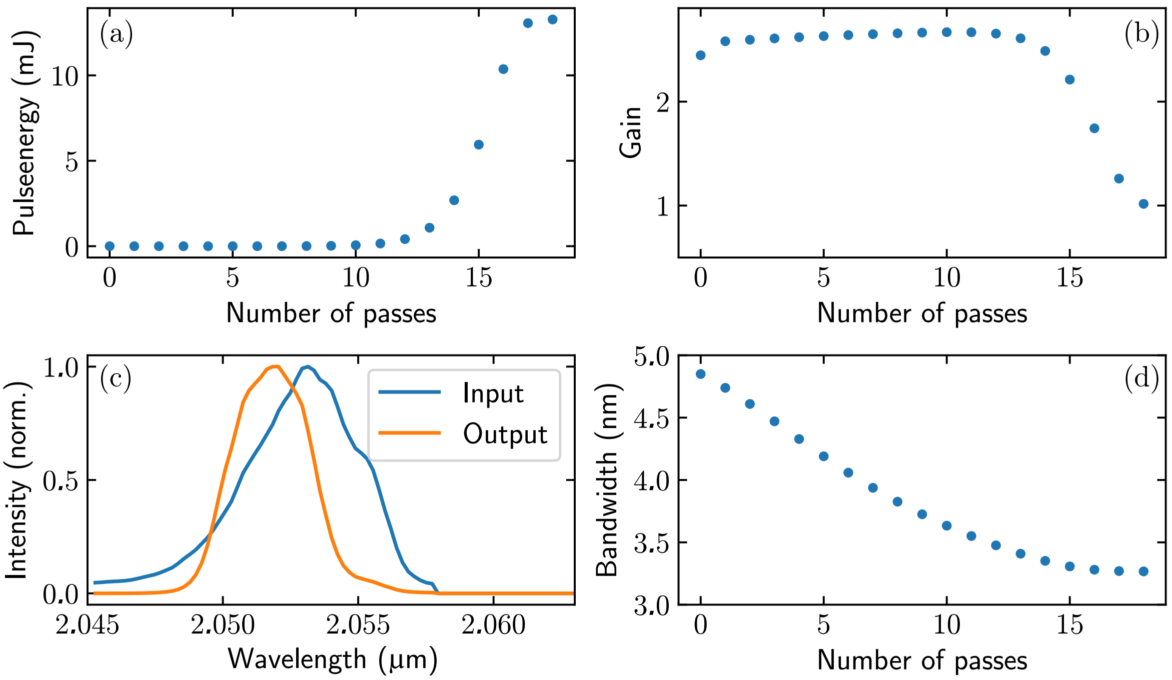

Figure 4.1: Simulation of the Ho:YLF regenerative amplifier showing (a) the exponentially amplified pulse energy reaching depletion after 19 round-trips, (b) the gain evolution until complete population depletion, (c) the seed and the output spectrum of the amplified pulses and (d) the bandwidth reduction due to gain narrowing as a dependence of the number of round-trips.

crystal) and the gain crystal Ho:YLF. This 50 mm long anti-reflection-coated rod with 0.5 % holmium doping concentration is pumped by 50 W from a continuous-wave randomly polarized thulium fibre laser (IPG Photonics) at 1940 nm. The pump laser is focussed with a 1000 mm lens to a spot size of 575 µm × 675 µm into the laser crystal. The gain crystal itself is water cooled to 10 °C while the cavity is maintained at room-temperature and purged with nitrogen to prevent atmospheric absorption of the pump and consequential blow-up of the focus. The housing of the cavity also avoids air turbulences and output energy instabilities.

The seed spectrum stems from a Cr:ZnS laser oscillator which directly provides the spectral part between 1.9 and 2.1 µm split from the remaining spectrum with a simple dichroic mirror containing 2 nJ energy, see Fig. 4.3(a). All other published 2 µm RAs have either used fs erbium doped fibre laser based front-ends [97, 99] or a Ho:fibre soliton oscillator [98]. They hence rely on subsequent nonlinear stages in order to provide the seed spectrum. Using the seed directly from a fs Cr:ZnS oscillator between 1.9 and 2.1 µm is yet to the best of my knowledge unique.

From the available spectrum, the chirped volume Bragg gratings (CVBG) select the wavelength range used to seed the RA, depicted as the green box Fig. 4.3(a). The pulses pass twice through a CVBG centred at 2051 nm with a spectral bandwidth of 11 nm and a stretching factor of 37 ps/nm. Subsequently, this spectrum is amplified in a Tm:fibre pre-amplifier to 7 nJ. The CVBGs stretch the pulses in time to roughly 1 ns duration and hence prevent self-phase modulation inside the pre-amplifier and reduce the B-integral accumulated inside the regenerative amplifier. Fig. 4.3(b) shows the seed spectrum after the pre-amplifier with 10 nm bandwidth indicating no signs of self-phase modulation. Another CVBG with 18 ps/nm stretching factor is used for further temporal stretching and eventually the regenerative

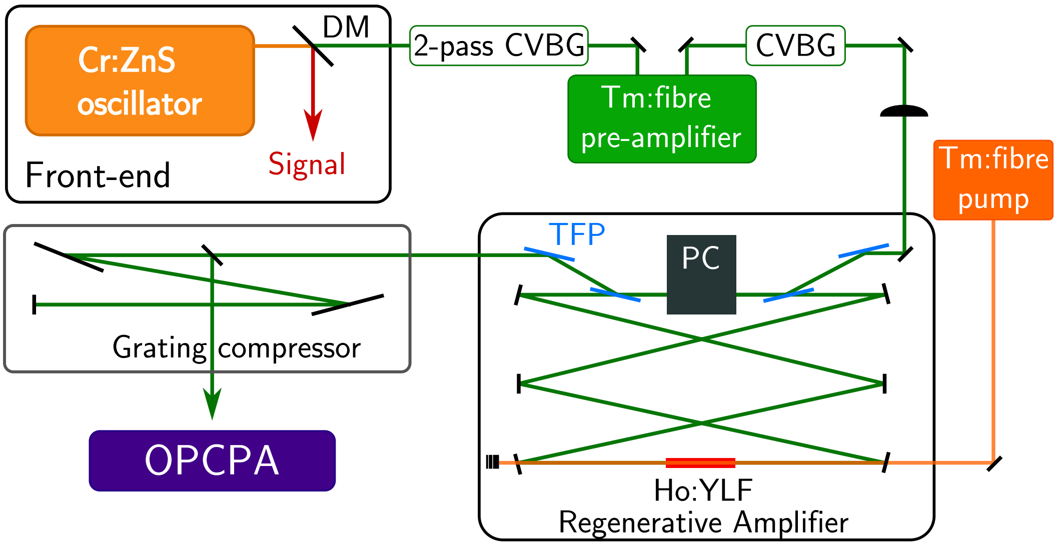

Figure 4.2: Scheme of the regenerative amplifier (RA) setup including the front-end with the fs Cr:ZnS oscillator and the dichroic mirror (DM), the stretching in chirped volume Bragg gratings (CVBG) to ≈ 1 ns and pre-amplification in a thulium doped fibre amplifier. The RA comprises the gain crystal Ho:YLF being pumped by a CW Tm:fibre laser at 1940 nm, the Pockels cell (PC) and the thin-film polarisers (TFP) as in- and output ports. It follows a Treacy-type grating compressor to compensate for the residual chirp of the amplified pulses before taken for the parametric stages of the OPCPA.

amplifier is seeded with 2.5 nJ of energy taking into account the losses prior to the injection into the RA.

The Pockels cell (PC) is operated at $\lambda/2$-voltage and synchronized to the front-end oscillator. If turned on and combined with a $\lambda/2$-plate, pulses in p-polarization stay inside the cavity. It is operated such that after the injection of one seed pulse, the PC is switched on for the time that equals the number of round-trips such that the pulse remains inside the RA. The coupling is conducted with two thin-film polarisers which are transparent for p-polarization and highly reflective for s-polarization. The PC allows to pick the pulses at a repetition rate of 1 kHz which sets the repetition rate of the entire OPCPA. The round-trip time is determined to be 11.4 ns which corresponds to a cavity length of 3.42 m. The number of passes through the laser medium is chosen to be 19, which is found to be the ideal number to ensure stable operation and the broadest spectrum in agreement with the simulations in Fig. 4.1. The amplified spectrum with a spectral width of 2.7 nm centred at 2051 nm is shown in Fig. 4.3(b).

The residual chirp of the amplified pulses is eliminated in a Treacy type grating compressor [109]. The AR-coated customized gratings with 900 lines/mm (Fraunhofer IOF) exhibit a diffraction efficiency of 98.5 % which results in a transmitted energy of 94 %. The compressed pulse duration is measured in a non-collinear autocorrelator (PulseCheck, APE GmbH) and is found to be 2.4 ps as its minimum being close the Fourier limit of 2.3 ps, see Fig. 4.4. The long-term measurement of the maximum pulse energy (Fig. 4.5) shows a mean value of 13.4 mJ with a root-mean-square (RMS) instability of 0.35 %. This output energy sets the record value for regenerative amplifiers at kHz repetition rate at 2 µm wavelength. The intensity profile is Gaussian with a very low asymmetry along x- and y-direction, see inset of

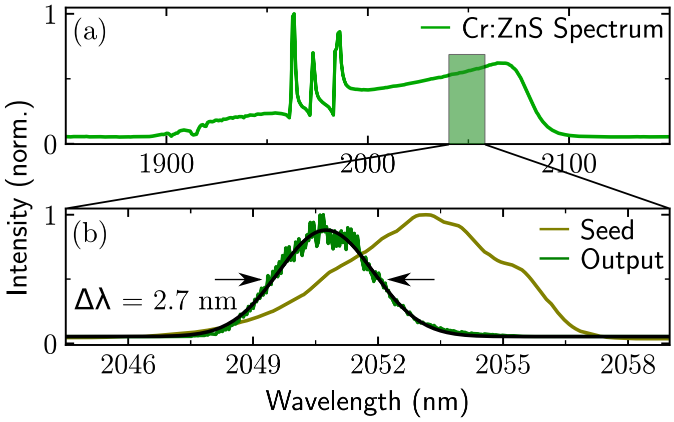

Figure 4.3: Spectra related to the regenerative amplifier with (a) the seed from the fs Cr:ZnS oscillator spectrum split at 2.1 µm and the CVBG selecting the amplified spectrum (green box), (b) the output of the Tm:fibre pre-amplifier (light green) with 2.5 nJ energy serving as the seed and the output spectrum of the RA after amplification and gain narrowing at 2051 nm (dark green and black Gaussian fit).

Fig. 4.5, due to the cavity geometry and the difference of refractive index of the YLF crystal in both axes. The M-square value is $M^2 < 1.2$. The regenerative amplifier with these parameters is used as the pump for the MWIR and LWIR OPCPA in this work.

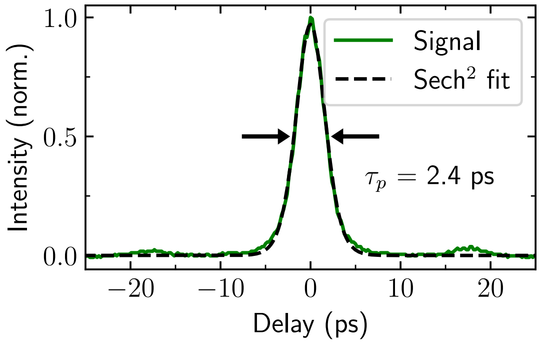

Figure 4.4: Autocorrelation measurement of the amplified pulses after compression with sech^2 fit and pulse duration of 2.4 ps (Fourier limit 2.3 ps).

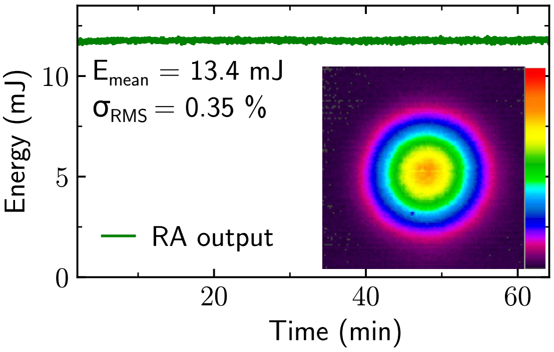

Figure 4.5: Long-term energy stability measurement after compression. Inset: far-field intensity distribution.

4.4 Spectral broadening of RA output pulses

According to the Fourier theory, a larger spectral width supports shorter pulse durations, reachable with a proper dispersion management. In a parametric process, the gain coefficient and the damage threshold in the nonlinear crystal depend on the incident peak intensity and the pulse duration, and pump pulses with sub-3 ps duration can be advantageous compared to longer pulse durations as discussed in the last section. A broader pump spectrum automatically translates into a broader idler spectrum if the phase matching supports all available spectral components. Also, in a theoretical framework from Fu et. al. [110], dual-chirping in DFG systems has been proposed being applicable to OPCPA systems if the pump pulses are short and spectrally broad. One possibility to enlarge the spectral width of the amplified pulses in the RA is to increase the seed pulse energy, requiring less round-trips and minimize the gain narrowing. Another option is to create a dip at the center of the spectrum such that the spectral components at the wings encounter more gain. This method is however limited to very few round-trips. Intracavity shaping with an etalon enables spectral shaping in every round-trip and has been proposed before [108]. To achieve this, a 200 µm thick uncoated BaF_2 substrate being transparent around 2050 nm serves as an etalon. The losses are solely dependent on the Fresnel reflections of the two surfaces which results in frequency depending losses where the substrate thickness and the angle of the etalon determine the modulation dip. In practice, the correct angle of the etalon needs to be found experimentally by trial and error. The introduced losses, however, result in an overall decrease of outcoupled energy.

The pulses exhibiting a bandwidth of 4 nm are compressed in the same Treacy type grating compressor and their duration measured in the same autocorrelator, see Fig. 4.6. The generated spectrum supports a Fourier limited pulse duration of $\tau = 1.6\,\text{ps}$. Despite the enlarged bandwidth (Fig. 4.7), it was not possible to compress the pulses down to Fourier limit when changing the compressor length. The most probable explanation is the sine-shaped phase which is imprinted on the pulse by the etalon which cannot be compensated by second and third order phase modulation in the grating compressor. Further investigations and compression attempts have not been conducted.

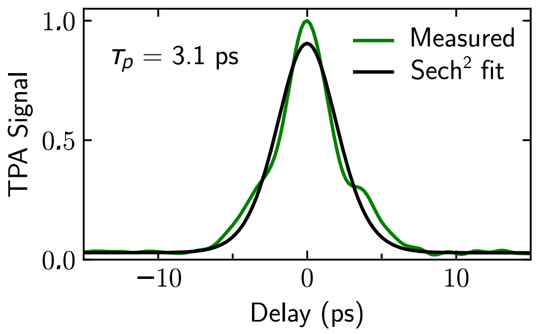

Figure 4.6: Autocorrelation measurement of RA pulses with intracavity shaping using a BaF_2 etalon after compression with sech^2-fit.

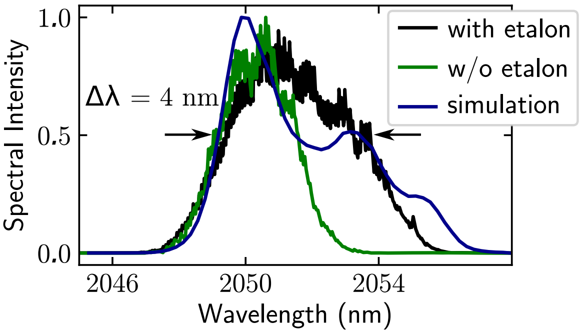

Figure 4.7: Comparison between amplified RA pulses with (black) and without (green) intracavity shaping. Simulation with etalon shaping in blue.

5

Front-end for mid-wave and long-wave infrared OPCPA

With the development of near-infrared (NIR) sources providing picosecond duration at the kilowatt level, OPCPA has emerged as a valuable technique for femtosecond pulse generation. The performance and development of suitable laser sources restrict the accessible wavelength range as the output key parameters of an OPA or OPCPA system are determined by the front-end. It is a crucial part of the system, as it provides the seed spectrum for the pump and the signal pulses and sets the repetition rate. The signal spectrum ultimately determines the maximum spectral width of the idler pulse and sets the lower limit for the achievable pulse duration. In order to support femtosecond pulse durations, ultrabroadband spectra are required. Typically, this prerequisite is achieved by additional broadening of the front-end pulses in nonlinear materials prior to amplification. Supercontinuum generation in bulk solid-state materials [111] or fibres [112] as well spectral broadening in noble-gas filled hollow core fibres [113] have been proposed in the past. The most straightforward way, however, is to use a front-end oscillator that naturally exhibits a broad spectral range sufficient for seeding the signal and pump arm directly.
However, the flexibility of the OPCPA output parameters comes at the expense of complex front-end architectures. In addition to a broad spectrum, the pump and signal pulses typically require spectral tunability as energy conservation reads $\hbar\omega_{\mathrm{pump}} = \hbar\omega_{\mathrm{signal}} + \hbar\omega_{\mathrm{idler}}$ and determines the output idler spectrum. This spectral tuning often necessitates optical parametric amplifiers, difference-frequency generation, or second-harmonic generation, just to name a few. If the spectral emission from the master oscillator is broad enough, the oscillator pulses can be split into two arms by frequency or by a certain ratio and can be individually manipulated.

In the past, front-end architectures based on Titanium Sapphire (Ti:Sa) oscillators have been proven suitable for implementing high peak power OPCPA systems [35]. Ti:Sa oscillators emitting at a wavelength of 800 nm with MHz repetition rate support few-cycle pulse durations in the near-infrared region [114, 115]. Hence, they fulfil the prerequisite of covering a broad spectral range. These lasers can serve as front-end lasers for MWIR and LWIR generation, but they come along with a number of difficulties which are thoroughly discussed in chapter 3. Pumping the nonlinear crystal below 1 µm poses the high risk of two-photon absorption and consequently crystal damage, the signal and the pump require wavelength shifting and the parametric process involves a large quantum defect. All this results in significant heat excess rates which requires cooling and limits the maximum pump energy. The simplest way of avoiding the aforementioned problems and to reduce the complexity of the system is the use of a front-end oscillator at a longer central wavelength.

Similar characteristics in terms of spectral width, pulse duration and repetition rate are offered by chromium doped zinc sulphite (ZnS) or zinc selenide (ZnSe) lasers which are referred to as the *Titanium Sapphires of the mid-infrared.* Chromium doped ZnSe and ZnS crystals offer high gain cross sections and a high optical-to-optical conversion efficiency [57]. The absorption spectrum spans from 1.3 to 2.1 µm which allows for pumping with off-the-shelf rare earth fibre lasers (Er^{3+} at 1.6 µm or Tm^{3+} at 1.9 µm) or commercially available diodes, see Fig. 5.1. The emission cross section spans from 1.8 to 3.4 µm (Fig. 5.2) and offers a large spectral range. The output spectrum is flexibly tunable via the laser cavity losses. Mainly the atmospheric absorption, the limited performance of dielectric coatings and the dispersion management restrict the maximum output spectrum. These lasers have the potential to become the master oscillator of choice for infrared OPCPA front-end architectures, and consequently enormous effort has been put in their development in the last decade [56, 116, 117].

Since the first demonstration of a femtosecond SESAM mode-locked Cr:ZnSe laser in 2006 [118], Cr-based laser systems have improved tremendously in terms of stability, pulse duration, repetition rate and peak power [53]. Depending on the target parameters, Kerr-lens mode locking is most appropriate for power scaling [119–123], soft aperture mode locking for the broadest spectra [54] and passive self-starting SESAM mode locking for high repetition rates [118, 124]. While MHz systems aim for high peak power and few-cycle pulse durations, GHz repetition rates are used in spectroscopy or as the basis for infrared frequency combs [11]. Cr-based ultrabroadband sources spanning over several octaves have been demonstrated [125] and enable CEP-stabilization [55].

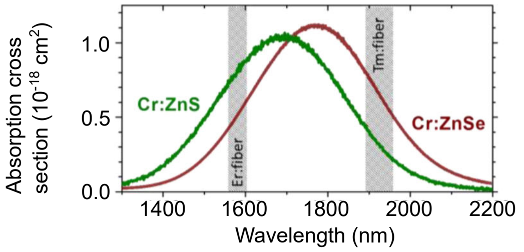

Figure 5.1: Absorption cross section of Cr:ZnS and Cr:ZnSe and emission lines of potential pump sources, taken from [53] (Fig. 3).

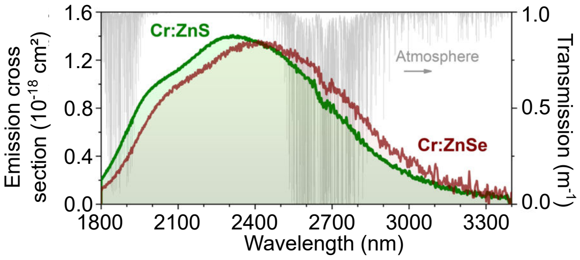

Figure 5.2: Emission cross section of Cr:ZnS and Cr:ZnSe and atmospheric vapour absorption cross section, taken from [53] (Fig. 4).

5.1 Femtosecond Cr:ZnS front-end oscillator

An overview of the front-end architecture for mid-wave infrared (MWIR) and long-wave infrared (LWIR) OPCPA of this work is given in Fig. 5.3. It shows that a simple dichroic mirror is sufficient to use the Cr:ZnS spectrum for the pump and signal generation. In the case of the signal generation, one can easily change between signal pulses fixed at 2.4 µm for LWIR and tunable between 2.8 and 3.2 µm for MWIR. Only very few components are necessary. The LWIR generation does not require any nonlinear stages. The MWIR generation necessitates one nonlinear stage in form of a frequency shift in a fluoride fibre. A related 5 µm OPCPA front-end based on an Er:fibre oscillator, developed in our group, is presented in Fig. 5.4. It shows the increased complexity and the multiple nonlinear stages of that system in order to generate a fixed signal wavelength at 3.4 µm. Hence, the system is set to one specific idler frequency. The comparison of these two systems clearly show the improvements in terms of flexibility and compactness for the current system. In the following two sections, the details about the LWIR and MWIR architecture are presented.

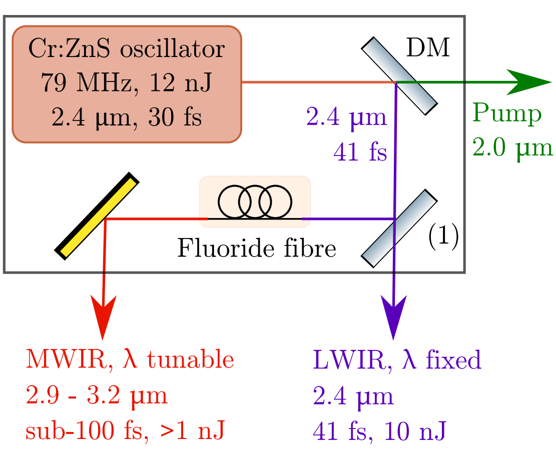
Cr:ZnS oscillator
79 MHz, 12 nJ
2.4 µm, 30 fs
DM
2.4 µm
41 fs
Pump
2.0 µm
Fluoride fibre
(1)
MWIR, λ tunable
2.9 - 3.2 µm
sub-100 fs, >1 nJ
LWIR, λ fixed
2.4 µm
41 fs, 10 nJ

Figure 5.3: Front-end architecture based on a Cr:ZnS oscillator for MWIR and LWIR OPCPA. Mirror (1) can be flipped to select the LWIR or MWIR signal pulses.

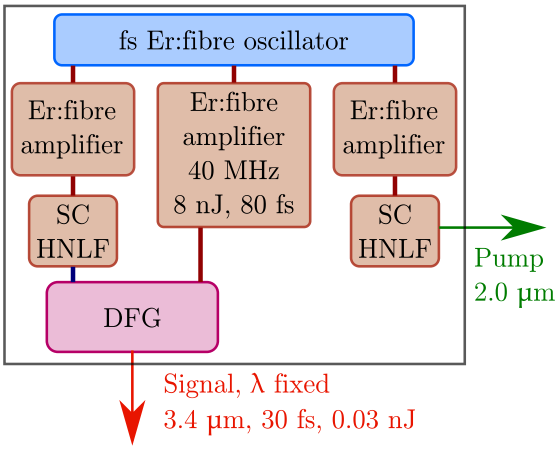
fs Er:fibre oscillator
Er:fibre amplifier
Er:fibre amplifier
40 MHz
8 nJ, 80 fs
Er:fibre amplifier
SC HNLF
SC HNLF
DFG
Pump
2.0 µm
Signal, λ fixed
3.4 µm, 30 fs, 0.03 nJ

Figure 5.4: Front-end architecture based on a Er:fibre oscillator of MWIR OPCPA adapted from [41], generating a fixed signal at 3.4 µm.

The Kerr-lens mode locked oscillator (IPG Photonics) using polycrystalline Cr:ZnS as the gain material is the key component of the front-end. It is operated at room temperature, the base plate is water cooled to 20 °C and running at 79 MHz. Being pumped with 4.3 W of a Er:fibre laser at 1.6 µm (IPG Photonics), the pulses are centred at 2.4 µm and have a spectrum spanning from 1.9 to 2.6 µm ($^1/_{e^2}$ level), see Fig. 5.5. An additional 3 mm AR-coated ZnSe window compensates the residual chirp and allows for pulses as short as 30 fs (Fig. 5.6). The oscillator has a total output power of 1.06 W which amounts to a 12 nJ pulse energy.

A dichroic mirror, placed behind the laser aperture, splits the spectrum at 2.1 µm into the pump and signal arm, see Fig. 5.7. It transmits wavelengths below 2.1 µm which are used to seed the regenerative amplifier and reflects the remaining part for the signal generation. This has the great advantage that pump and signal are passively synchronized. As the stability of the entire system relies on the output power stability of the oscillator, the long-term output

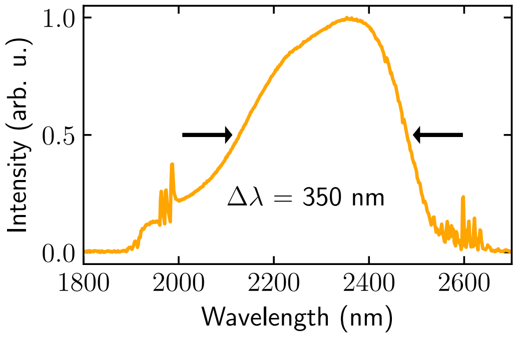

Figure 5.5: Spectrum of Cr:ZnS master oscillator with 350 nm FWHM bandwidth.

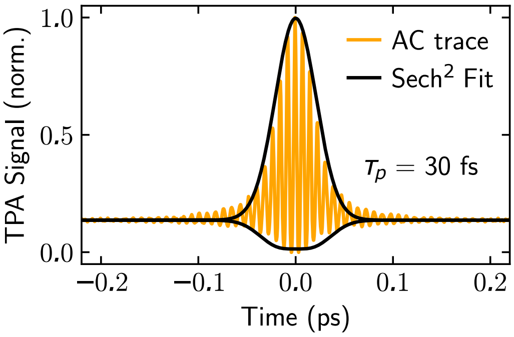

Figure 5.6: Autocorrelation trace of Cr:ZnS oscillator pulses (miniTPA, APE) and fit.

power behind the dicroic mirror was recorded over more than two hours, see Fig. 5.8. The spectral party beyond 2.1 µm has an average output power of 810 mW which corresponds to a pulse energy of 10 nJ. The root-mean-square (σ_{RMS}) stability amounts to 0.04 % which is reasonably good and in agreement with the literature [57].

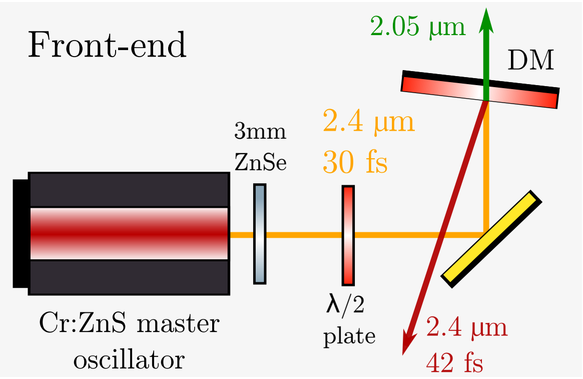

Figure 5.7: Front-end architecture comprising the master oscillator, a $\lambda/2$ waveplate and a dichroic mirror (DM).

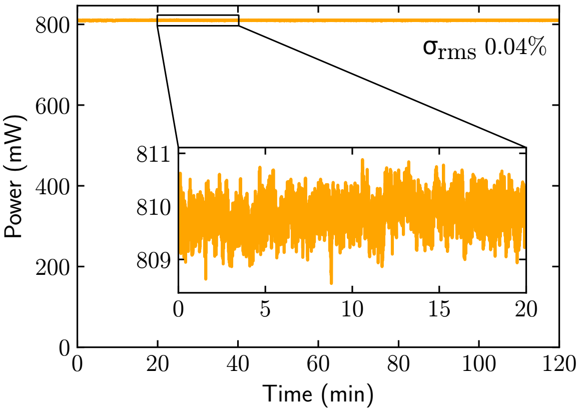

Figure 5.8: Long-term power stability of Cr:ZnS master oscillator behind dichroic mirror. Total output power is 1.06 W, corresponding to 12 nJ pulse energy.

5.2 LWIR front-end

Only a very limited number of research groups have aimed to reach the spectral region above 10 µm using parametric processes relying on rather complex front-end architectures [47–50]. However, the limited availability of suitable pump sources at 2 µm and the large quantum defect when pumping at 800 nm (Ti:Sa laser) or 1060 nm (Yb:YAG laser) have restricted the output energy in the long-wave infrared region (LWIR) to 10 µJ [23, 51]. All these system have a driver laser system around or below 1 µm which needs to be shifted to longer wavelengths prior to parametric amplification. The pump and the signal are generated by multiple nonlinear processes. Beside supercontinuum generation [50] and difference frequency generation [23, 47, 48], entire optical parametric amplification systems are necessary as the front-end [49, 51].

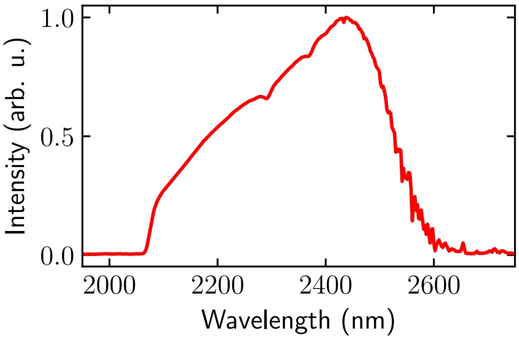

Figure 5.9: Spectrum of signal seed pulses for LWIR OPCPA beyond 2.1 µm.

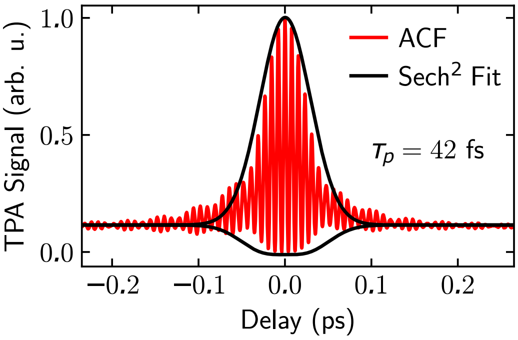

Figure 5.10: Autocorrelation trace of signal seed pulses for LWIR OPCPA - recorded with TPA mini AC (APE) - and sech^2 fit.

Their complexity and the cascading nature of pump and signal spectral shifting is closely associated with a poor conversion efficiency and high maintenance effort.

The simplicity of the system and the direct access to the pump and signal wavelength from the master oscillator are unique features of the LWIR front-end presented here. The broad Cr:ZnS oscillator spectrum entirely expands beyond 2 µm and offers seed pulses in the nJ energy range. This front-end profits, on one hand, from the oscillator providing directly the signal pulses centred at 2.4 µm (Fig. 5.9) with comparably high energies of 10 nJ. Though the spectral part below 2.1 µm was removed for the pump seed, the signal pulses still exhibit a pulse duration of 42 fs (Fig. 5.10). On the other hand, the same oscillator seeds the regenerative amplifier at 2.05 µm which emits pulses with an energy of >13 mJ at 1 kHz repetition rate (see ch. 4). The pump source provides enough energy to seed multiple parametric amplification stages in the LWIR spectral region. Without any additional nonlinearities, the pump at 2.05 µm and the signal at 2.4 µm combine to an idler wavelength beyond 10 µm [126].

5.3 MWIR front-end

The lack of laser gain materials in the mid-IR region beyond 4 µm has driven the development of OPCPA systems in this spectral region. The front-end architecture required to generate wavelengths between 5 and 8 µm is a challenge for similar reasons as for the LWIR spectral region. The use of 1 µm master oscillators and pump sources have been triggered by their maturity and the commercial availability. However, they demand spectral shifting of pump and signal spectrum and the front-end architectures are correspondingly complex. Mid-IR OPCPA systems involve multiple nonlinear processes, such as supercontinuum generation, difference frequency generation and/or second harmonic generation [28, 40, 41, 44]. The cascaded nonlinear effects increase the complexity of these systems, and entail the difficulty of stable operation and maintenance. Also, multiple nonlinear stages suffer from losses and poor conversion efficiencies and restrict the maximum output energy. Consequently, the preferred front-end architecture should be simple and not relying on cascaded nonlinear processes.

Spectral tunability of the signal pulses directly entails a wide range of idler wavelengths. It makes the system suitable for different spectroscopic applications and reduces the customization effort to a minimum. All the above mentioned systems [28, 40, 41, 44] are fixed in wavelength and lack spectral flexibility. The MWIR front-end presented in the following uses the same pump and signal pulses as the LWIR front-end presented above, but additionally tunes the signal pulses. Combining fluoride fibres with a Cr:ZnS master oscillator is a compact and easy way to achieve tunability [127] which is successfully demonstrated in [128, 129] and presented in the following section. It introduces how the signal pulses are flexibly tuned between 2.8 and 3.25 µm with only one nonlinear stage.

5.3.1 Raman self-frequency shifting of signal pulses

In the present front-end, the signal pulses from the master oscillator (directly used in the LWIR setup) at 2.4 µm and with 42 fs pulse duration are launched into a nonlinear ZBLAN (ZrF_4 BaF_2 LaF_3 AlF_3 NaF) fluoride fibre. For wavelengths longer than 2 µm the fibre exhibits negative group velocity dispersion (GVD). Dispersion, in principle, leads to temporal pulse broadening, especially if the pulse is not centred at the zero-dispersion wavelength. Depending on the sign of the GVD, the pulse is afterwards said to be positively or negatively chirped. A fibre's dispersion can be calculated as the combination of the material's and the fibre's waveguide dispersion [130].

In the case of (ultra-)short pulses, the nonlinear refractive index of the fibre material needs to be considered as the peak power is importantly increased. In fibres, self-phase modulation is a prominent phenomena which leads to a spectral broadening. However, when combining self-phase modulation and negative GVD, one can show that the nonlinear Schrödinger equation (NLSE, introduced in sec. 2.7, eq. 2.44) is solved for a hyperbolic secant pulse amplitude if both effects compensate each other perfectly and higher order dispersion terms are neglected. Pulses fulfilling this condition are called *solitons*. In the absence of losses and fibre imperfections, solitons propagate through dispersive fibres experiencing neither temporal nor spectral pulse broadening [63].

In 1986, Gordon described in his theoretical work [131] the effect of self-frequency shifting solitons inside fibres. The pulses experience a linear frequency chirp over the propagation distance while maintaining a well defined temporal shape. In this process, the higher frequency parts of the pulse seed the lower frequency parts through stimulated Raman scattering. Ultrashort pulses can therefore shift towards longer wavelengths while maintaining a temporal and spectral hyperbolic secant shape. In the same year, Mitschke and Mollenauer experimentally confirmed this effect and demonstrated a frequency shift for 1.5 µm sub-picosecond pulses in a fibre [132]. Simply speaking, the frequency shift depends mainly on the peak intensity inside the fibre, the pulse's initial chirp and the fibre parameters. The magnitude of the shift is tunable via the fibre length, the total energy or the temporal chirp of the launched pulses. The frequency shift, however, saturates after a certain propagation distance. The dissipative nature of the Raman effect leads to an increased pulse duration and a decrease of pulse energy. This is, over the propagation distance the peak intensity decreases and as a consequence, the nonlinear term diminishes. Since high frequency components convert into lower frequency components, the energy of the soliton not conserved. In principle, Raman self-frequency shifting is possible for normal and anomalous GVD, but the effect is less prominent for normal dispersion as the pulse duration significantly increases due to dispersion [133]. In the absence of intrapulse Raman scattering, solitons remain unchirped when transmitted through a fibre. However due to the spectral shift, the unchirped nature is not granted.

In this MWIR front-end, the signal pulses are tuned by exploiting the effect of Raman self-frequency shifting. The dispersion curve for the employed ZBLAN fibre is shown in Fig. 5.11. It is a single mode fibre with a core diameter of 6.5 µm. It has been fabricated and purchased from *Le verre Fluoré* with 60 cm and 2 m length. The fibre's dispersion has been calculated by C. Mei taking into account the material dispersion of the core and the cladding [134], and the waveguide properties. The Zero Dispersion Wavelength (ZDW) lies slightly below 2 µm and the whole signal seed spectrum experiences negative GVD which is advantageous for an efficient frequency shift.

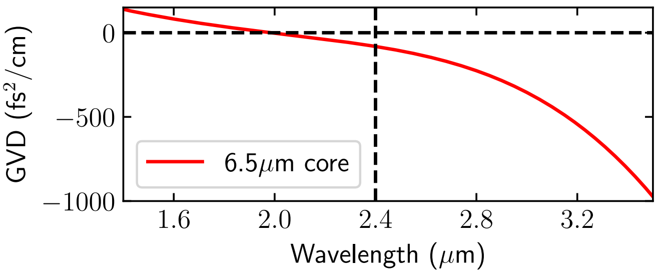

Figure 5.11: Calculated group velocity dispersion (GVD) for a 6.5 µm core ZBLAN fibre with a zero-dispersion wavelength (ZDW) at 1.99 µm. Vertical dashed line: laser central wavelength.

The 2.4 µm pulses (Fig. 5.9 and 5.10) are coupled into the fluoride fibre using a parabolic mirror with a focal length of 12.7 mm and the generated spectrum is recorded. Successful soliton formation was only possible with reflective optics. When using a *normal* transmitting lens, the spectrum only experienced nonlinear modulations. We believe that the chirp introduced by the propagation through the lens was too large in order to reach the soliton regime. In this case, one would require additional pre-chirp compensation. The tuning has been firstly demonstrated in a 60 cm long fibre, as depicted in Fig. 5.12. It shows clearly the generation of a well defined soliton shifting towards longer wavelengths if a certain amount of pulse energy is coupled into the fibre. The soliton wavelength is tuned by changing the coupling efficiency. This was realized by moving the fibre end facet out of focus to reduce the coupling. In this way, it is possible to tune the soliton up to 3.15 µm with an energy of 2.8 nJ. Alternatively, the tuning is achieved by introducing different amounts of chirp on the pulses prior to coupling [135] but was not investigated.

In order to generate an idler pulse above 4 µm, the corresponding signal wavelength should be further shifted to longer wavelengths. In order to do this, a 2 m long ZBLAN fibre is used instead. In the same way, the pulses are coupled to the fibre and tuned. The corresponding

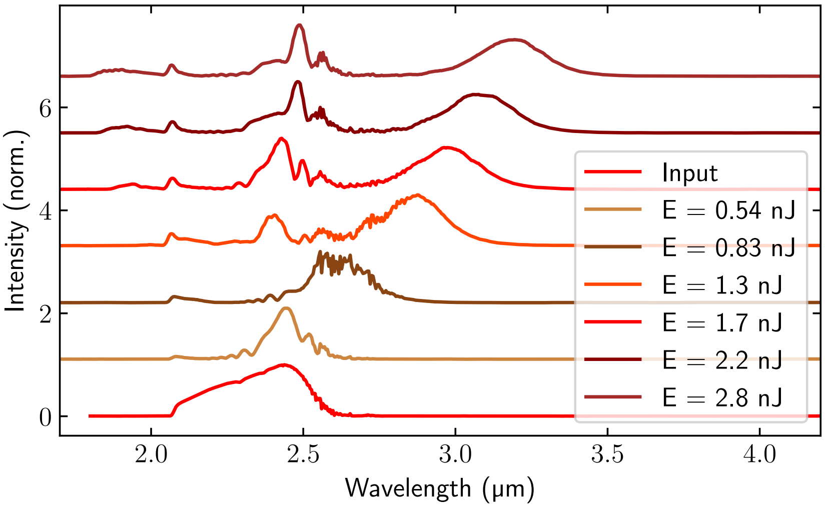

Figure 5.12: Spectrum of Raman self-frequency shifted solitons for different launched pulse energies behind 60 cm long ZBLAN fibre.

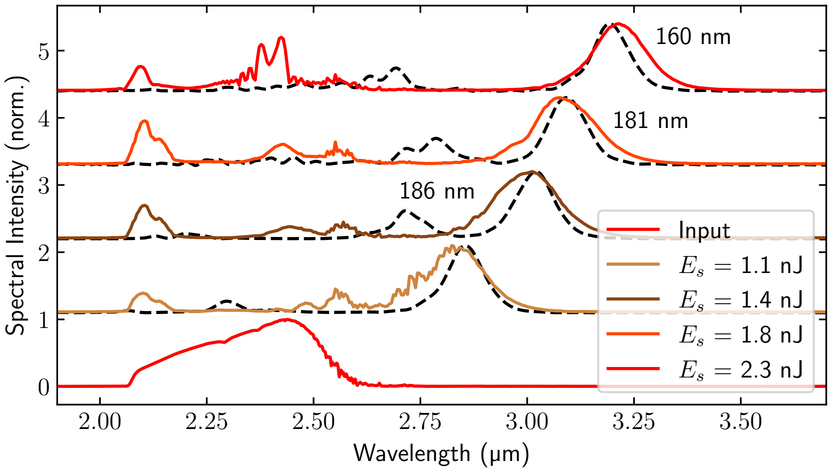

Figure 5.13: Measured self-frequency shifted solitons (solid lines) for different launched pulse energies behind 2 m long ZBLAN fibre and simulated soliton spectra (dashed lines) with *fiberdesk*. The spectral width (FWHM) has been fitted with a hyperbolic secant shape to the data.

spectra are shown in Fig. 5.13. In order to understand the process, the nonlinear Schrödinger equation introduced in equation 2.44 is solved. The simulation programme *fiberdesk* is used to solve the equation in a split step method. Besides the precise knowledge of the input pulses, the fibre parameters determine the temporal and spectral evolution of the pulse. With the input fibre parameters the simulation matches the output spectrum adequately. Details about the simulation follow in the next section 5.3.2. In Fig. 5.13, the measurement and simulation can be directly compared. The soliton is reliably tunable between 2.9 µm and 3.25 µm and reproducible after switching-off the system. The larger the frequency shift, the narrower the bandwidth and consequently, the longer the pulse duration. This behaviour is in accordance with the solution proposed by [133].

The soliton at 2.99 µm is characterized in order to prove the soliton nature of the pulse behind the fibre. Though the fibres are not explicitly polarization maintaining, the output soliton is found to be linear polarized. In Fig. 5.14, the spectrum and the corresponding autocorrelation trace is shown. The autocorrelation is measured in collinear configuration with a two-photon detection head (miniTPA, APE). The spectral part not contributing to the soliton pulse is removed by a dielectric mirror which only reflects the wavelengths beyond 2.8 µm. The pulse duration of 79 fs is slightly longer than the expected Fourier limit of 63 fs for a 140 nm bandwidth with hyperbolic secant shape. Even though transmissible optics where omitted in the measurement as much as possible, a $\lambda/2$ waveplate was necessary to ensure the right polarization for the autocorrelator. Hence, the actual pulse duration might be even a little shorter. But since the pulse shape is clean and well defined and is in the following chirped to ps-duration to match the pump pulse duration, the shifted signal pulse is perfectly suitable for the OPCPA.

The great advantage of this shift is that the architecture is maintained simple and is additionally tunable. This front-end architecture is also superior in terms of signal energy. While other front-end architectures have to amplify picojoule signal seed energies [41], this setup directly provides nanojoule energy. From the practical point of view, the increased amount of energy makes the alignment much easier, and also reduces the number of amplification stages necessary to reach a certain energy level.

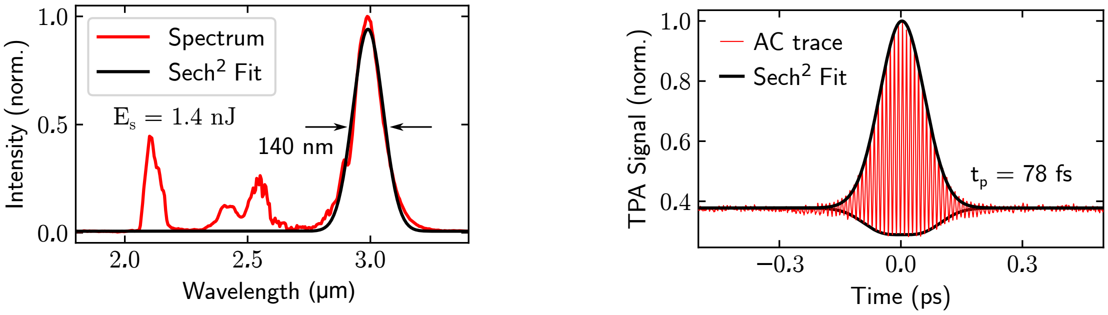

(a) Spectrum of shifted soliton with a 140 nm width at FWHM.

(b) Autocorrelation measurement confirming soliton duration of 78 fs.

Figure 5.14: Spectral and temporal characterisation of the self-frequency shifted soliton with 1.4 nJ at 2.99 µm behind the 2 m long ZBLAN fibre.

5.3.2 Simulation of pulse evolution inside the fibre

The evolution of the pulse in spectral and temporal domain can be simulated by solving the nonlinear Schrödinger equation. The simulation programme *Fiberdesk* [136] is used. The input spectrum and energy of the coupled pulses are provided as the starting parameters and from this, the evolution for a given fibre is calculated. The ZBLAN fibre parameters are key to the simulation results. From literature, the nonlinear refractive index is $n_2 = 5.4 \times 10^{-20}\,\mathrm{m^2/W}$ and the contributed Raman fraction $f_R = 0.24$ [137] were implemented. The mode field diameter is calculated to be 8.4 µm [63] and the additional shock time τ_A is calculated according to

$$\tau_{\text{shock}} = \tau_0 + \tau_A = \frac{1}{\omega_0} - \left[\frac{1}{n_{\text{eff}}}\frac{\partial n_{\text{eff}}(\omega)}{\partial \omega}\right]_{\omega_0} - \left[\frac{1}{A_{\text{eff}}}\frac{\partial A_{\text{eff}}(\omega)}{\partial \omega}\right]_{\omega_0} \tag{5.1}$$

being $\tau_A = 1.5\,\mathrm{fs}$. The derivative of the effective mode size $A_{\mathrm{eff}}(\omega)$ inside the fibre is calculated from the fibre properties. Similarly, the effective index $n_{\mathrm{eff}}(\omega)$ changes with frequency. These two parameters as well as the dispersion parameters up to $\mathcal{O}(\omega^{15})$ (see eq. 2.12) have been calculated from the material and waveguide dispersion by C. Mei, see Fig. 5.11. The theoretical spectral and temporal evolution are shown in Fig. 5.15 and Fig. 5.16. The spectral evolution in Fig. 5.15 shows how the soliton grows from the generated supercontinuum after a few mm inside the fibre. It then shifts in frequency as it propagates in the fibre. In addition, fig. 5.16 shows that the pulse does not split up only spectrally but also in the time domain. The different frequency components experience a different GVD and hence separate temporarily. In the context of parametric interactions, this splitting allows to select only the pulse of interest without the risk of parasitic amplification of the frequency components not contributing to the soliton. Consequently, the simulation gives a valuable insight into the dynamics of the soliton evolution and describes in good agreement the outcome for different launched pulse energies (see Fig. 5.13).

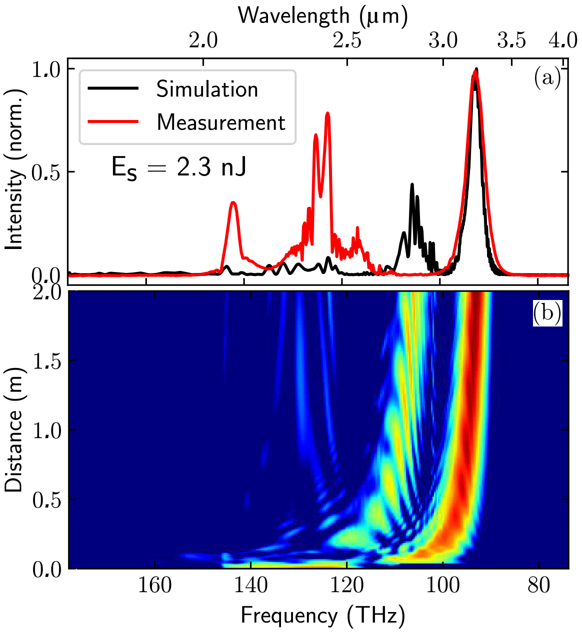

Figure 5.15: Lower graph (b): Simulated spectral evolution of soliton in 2 m long ZBLAN fibre using the nonlinear Schrödinger equation (eq. 2.44). Upper graph (a) measured spectrum for 3.2 µm soliton and simulation at 2 m.

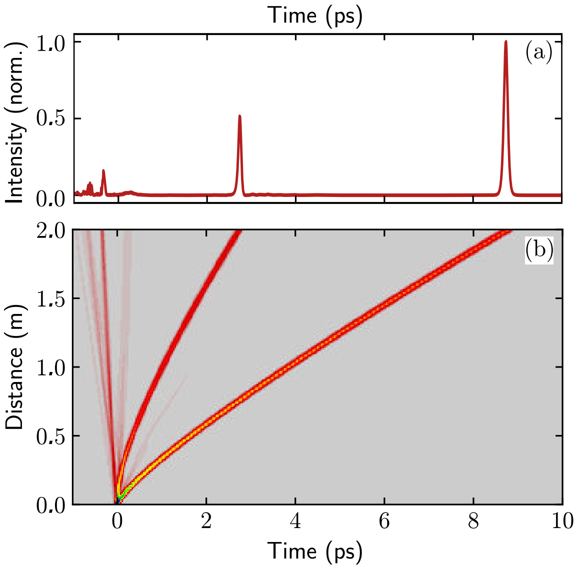

Figure 5.16: Lower graph (b): simulated temporal evolution of soliton in 2 m long ZBLAN fibre using the nonlinear Schrödinger equation (eq. 2.44), upper graph (a) temporal intensity distribution at 2 m.

5.3.3 Energy stability and timing jitter of the soliton

The energy stability of the soliton is crucial as it contributes to the overall stability of the OPCPA. There are two kinds of uncertainty, namely energy and time fluctuations. The soliton energy behind the ZBLAN fibre for the soliton at 3.2 µm in Fig. 5.17 was recorded of three hours and shows a stability of 0.4 %.

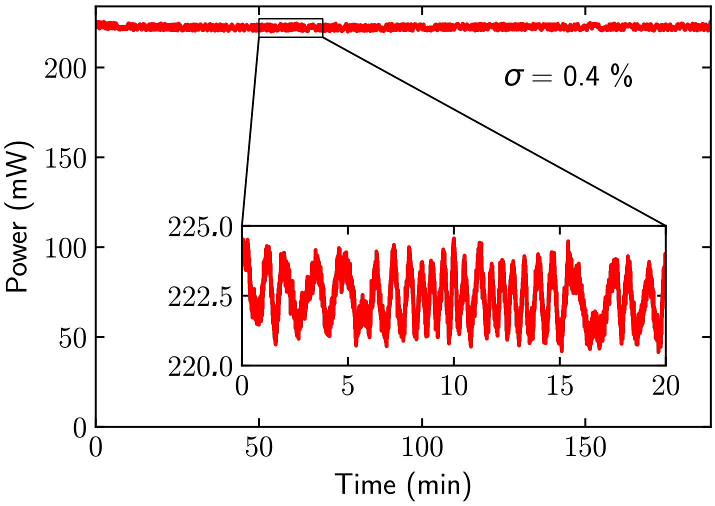

Figure 5.17: Stability measurement of 3.25 µm soliton behind the 2 m ZBLAN fibre.

In the following, the influence of the output energy on the timing jitter is studied. A modified and improved momentum method is used which reduces to Gordon's perturbation theory [131] for hyperbolic secant shaped pulses if the Raman induced frequency shifting is relatively small. The moment method describes the intrapulse Raman shift (IRS) in an analytic way for a slowly varying envelope [133, 138]. One can write the complex amplitude of a hyperbolic secant with a frequency shift as follows:

$$A(z,T) = \sqrt{\frac{E_p}{2T_p}}\,\mathrm{sech}\left(\frac{T-q_p}{T_p}\right)\exp\left(-i\Omega_p(t-q_p) - iC_p\frac{(T-q_p)^2}{2T_p^2}\right) \tag{5.2}$$

The phase term describes the frequency shift and the chirp. Here T_p is the soliton duration, C_p the time domain chirp, E_p the pulse energy, q_p the temporal shift and Ω_p the frequency shift from the original carrier frequency. The method defines the moment for the five quantities mentioned above which vary with propagation distance z. It then uses their differential equations to study the evolution of soliton parameters. The temporal shift and the frequency shift are defined as follows

$$q_p = \frac{1}{E_p}\int_{-\infty}^{\infty} T|A|^2\,\mathrm{d}T \tag{5.3}$$

$$\Omega_p = \frac{i}{2E_p}\int_{-\infty}^{\infty}\left(A^*\frac{\partial A}{\partial T} - A\frac{\partial A^*}{\partial T}\right)\mathrm{d}T. \tag{5.4}$$

If one now substitutes eq. 5.2 into eq. 5.3 and 5.4, taking the derivative and integrating it, under the assumption that $E_0 = 2P_0T_0$, where P_0 is the peak power and T_0 the initial pulse duration, the temporal shift and the frequency shift are calculated by

$$q_p(z) = \int_0^L \beta_2\Omega_p(z) + \gamma P_0\frac{T_0}{T_p(z)}\,\mathrm{d}z \tag{5.5}$$

$$\Omega_p(z) = -\frac{8T_R\gamma P_0T_0}{15}\int_0^L \frac{1}{T_P^3(z)}\,\mathrm{d}z, \tag{5.6}$$

where $\gamma = \frac{n_2\omega_0}{c_0A_\mathrm{eff}}$ is nonlinear parameter responsible for self-phase modulation, T_R is the Raman coefficient that accounts for the intrapulse Raman shift. With the fundamental soliton condition being

$$T_p(z) = \frac{2\beta_2}{\gamma E_p(z)}, \tag{5.7}$$

the temporal shift can be rewritten with equation 5.7 to

$$q_p(z) = \int_0^L \left(\frac{\gamma^2 P_0 T_0}{2\beta_2 \omega_0} E_p(z) - \left(\int_0^L \frac{T_R P_0 T_0 \gamma^4}{15\beta_2^2} E_p^3(z) \mathrm{d}z \right) \right) \mathrm{d}z, \tag{5.8}$$

if equation 5.6 is substituted into 5.5. The temporal shift contains two terms of which one only depends on γ and entirely relates to the Kerr effect. The second term depends on T_R and can be associated to the temporal shift caused by the Raman effect which is relevant for this analysis. If we assume energy conservation over the length of the fibre, the deviation in energy can be rewritten as $E_p = E_0(1+\epsilon)$ and can be treated as a perturbation. Rewriting now the second term of the temporal shift with the perturbation term, one finds

$$q_p(z) = \frac{T_R \gamma^4 E_0^4}{30\beta_2^2} \int_0^z \int_0^{z'} [1+\epsilon(z')]^4 \mathrm{d}z' \mathrm{d}z. \tag{5.9}$$

Ultimately, the relation between timing jitter and energy instability can be expressed as

$$\delta = \frac{q_p'(z) - q_p(z)}{q_p(z)} = (1+\epsilon)^4 - 1. \tag{5.10}$$

In Fig. 5.17 the energy stability for the soliton is found to be $\sigma = 0.4\,\%$. From the last equation, it is now possible to estimate the timing jitter to be $\delta = (1+0.004)^4 - 1 = 1.6\,\%$. For an 80 fs pulse, this corresponds to 1.3 fs which is clearly negligible when pumping the OPCPA with ps pulses.

The frequency shift of the soliton inside the 60 cm and 2 m long fibre is presented in Fig. 5.18. It shows the frequency shift from 2.4 µm to the soliton central wavelength as a function of the output soliton energy. Only output spectra with clear sech-shaped spectra are considered and the measured maximum frequency shift is 31 THz. The curves suggest for both fibre lengths that the frequency shift is not yet saturated and coupling more energy could lead to further red shifting. Unfortunately, this cannot be verified with the current setup since the signal pulse energy is restricted to the output pulse energy of the front-end oscillator.

As depicted in Fig. 5.18(b), one can estimate the frequency shift error depending on the energy fluctuation. The frequency shift is fitted with a linear function as a linear dependence is predicted by theory. From error propagation, an energy fluctuation of 0.4 % results in a frequency shift $\delta\Delta f = 55$ GHz which transfers to $\Delta\lambda = 3$ nm for the 3.2 µm soliton. In comparison with the lower limit spectral width of > 4.6 THz for all solitons, the frequency jitter of 1.2 % is of the order of the timing jitter and is small enough in the OPCPA context.

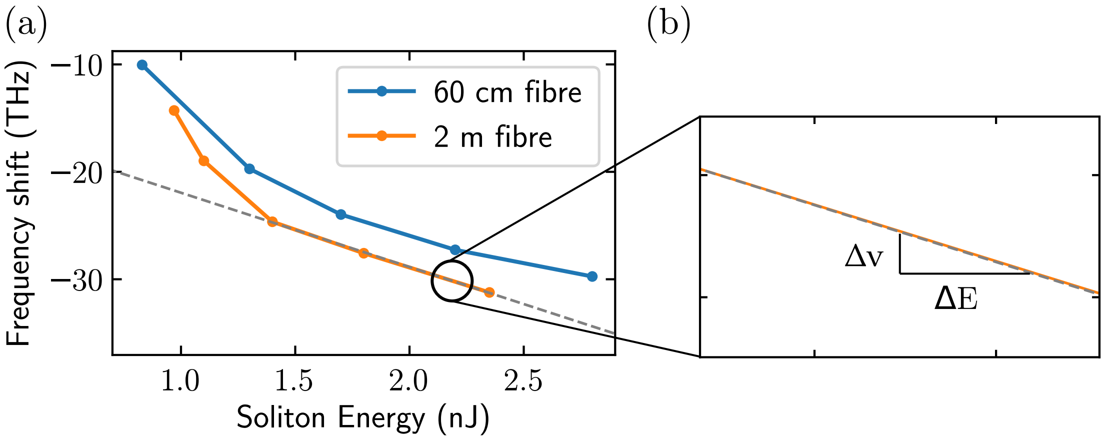

Figure 5.18: (a) Comparison and evolution of the measured frequency shift of solitons for different energies in the 2 m and 60 cm fibre. (b) How energy instability transfers to frequency jitter under assumption of linear energy-frequency dependency.

6

Mid-wave infrared OPCPA

The spectral region between 3 and 8 µm is called the mid-wave infrared region (MWIR) where numerous molecules have their characteristic vibrational absorption lines. This is why it is referred to as the *Fingerprint Region*. In the context of strong field physics, mid-IR pulses have been found advantageous compared to near-IR lasers usually used for the generation of high-harmonics or hard x-rays [14, 30]. For the latter, laser sources with electric fields on the order of the electron binding strength in matter are developed.

The development of mid-infrared OPCPA systems has been triggered by the lack of gain materials beyond 4 µm aiming for kHz repetition rates, femtosecond duration at the GW level. Their success has, so far, been restricted by the unfavourable pump-to-idler photon ratio when using 1 µm pump wavelengths. As a consequence, novel pump sources operating around 2 µm based on Ho-doped or Tm-doped gain media in combination with non-oxide nonlinear crystals, such as $ZnGeP_2$ (ZGP), have become the basis for high energy OPCPA systems beyond 4 µm. Nevertheless, the number of OPCPA systems in this spectral range is still very limited [39]. Multi-GW, few optical cycle pulses at 5.1 µm have been produced in an OPCPA system with a femtosecond Er:fibre laser front-end [41]. This system was upgraded to 89.4 fs, 3.4 mJ pulses at 4.9 µm with 33 GW peak power in a fourth amplification stage [43]. With a similar architecture, the generation of self-carrier-to-envelope-phase stable, sub-eight-optical-cycle duration pulses at 7 µm with 100 Hz repetition rate and 0.55 mJ output power was demonstrated in [44].

The present system uses a femtosecond Cr:ZnS laser oscillator which offers a fairly simple front-end, see Ch. 5. The idler pulses are tunable in the mid-IR region between 5.4 to 6.8 µm and have an energy of up to 400 µJ with sub-100 fs pulse duration at a 1 kHz repetition rate [128, 129]. The system relies on two parametric stages based on ZGP, of which one is non-collinear and the other collinear. Compared to [139], this OPCPA has a smaller footprint and a simpler architecture. The spectral tunability is unique beyond all existing MWIR OPCPA systems and makes this system promising for a wide range of application.

6.1 Two stage optical parametric amplifier

The optical parametric amplifier (OPA) setup comprises the front-end with the Cr:ZnS oscillator and the ZBLAN fibre introduced in sec. 5.3, the Ho:YLF regenerative amplifier pump at 2.05 µm introduced in ch. 4, and the two parametric stages. The first non-collinear OPA stage and the second collinear OPA stage are both seeded with the signal and equipped with a 2 mm ZGP crystal. The main layout is adapted from the previous setup [139] and the same parametric conditions apply with the difference that the signal pulses are tunable between 2.9 and 3.2 µm with 80 fs duration. Please refer to [80] for more details on the phase matching properties and parametric amplification parameters. The nonlinear crystals are both ZGP, cut for type-I phase matching (BAE Systems) and anti-reflection coated. The chosen type I phase matching has the following polarization scheme: pump(o) → signal(e) + idler(e). In order to ensure a broad phase matching bandwidth, OPA 1 is in non-collinear geometry with an internal angle of 2°, corresponding to an external angle of 6°. The phase matching angle is accordingly set to $\theta_{\mathrm{PM}} = 59°$. OPA 2, in contrast, is seeded with the amplified signal from OPA 1 and designed in a collinear geometry with $\theta_{\mathrm{PM}} = 55.4°$ to ensure the generation of an idler without angular dispersion.

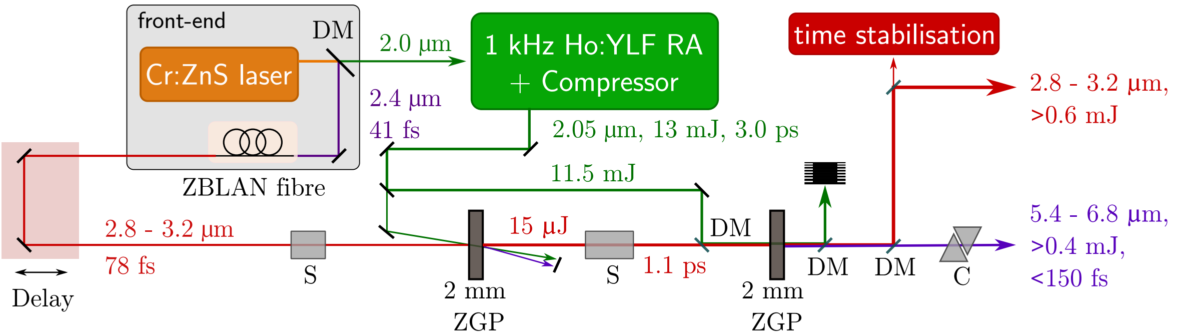

Figure 6.1: MWIR OPCPA setup with an idler output energy of >0.4 mJ tunable between 5.4 and 6.8 µm and sub-150 fs pulse duration. The setup includes the front-end with the Cr:ZnS oscillator and the soliton shifting ZBLAN fibre, the 2.05 µm Ho:YLF regenerative amplifier (RA) as the pump and two optical parametric amplification (OPA) stages. DM: dichroic mirror, S: stretcher, C: compressor.

The parametric efficiency depends heavily on the temporal overlap between the signal and the pump pulses, see sec. 3.4.2. The signal pulse duration is therefore matched to the pump pulse duration of 3.0 ps by introducing bulk material with negative GVD. In the following, if speaking of the signal pulse, the soliton at 3.2 µm is meant if not indicated otherwise. The signal pulses are initially stretched after the Raman frequency shift in the ZBLAN fibre in a 40 mm Al_2O_3 crystal to 830 fs, and further broadened to 1.1 ps between the first and the second OPA stage in 80 mm CaF_2. The resulting values for the group velocity dispersion (GVD) and the third-order dispersion (TOD) are given in Tab. 6.1. The calculated GVD and TOD values in the same materials but for different wavelengths illustrate that the pulse duration slightly changes when tuning the soliton. As a consequence, the corresponding idler also needs an adapted compression material.

	40 mm Al_2O_3		80 mm CaF_2	
λ (µm)	GDD (fs^2)	TOD (fs^3)	GDD (fs^2)	TOD (fs^3)
2.9	-19.5×10^3	115×10^3	-7.6×10^3	42×10^3
3.0	-22.0×10^3	134×10^3	-8.6×10^3	49×10^3
3.1	-24.7×10^3	155×10^3	-9.6×10^3	55×10^3
3.2	-27.7×10^3	180×10^3	-10.6×10^3	63×10^3

Table 6.1: GDD and TOD values of employed bulk stretchers for different signal wavelengths.

The 0.8 ps signal pulses are amplified to 15 µJ in OPA 1. The pump energy in this stage is set to 320 µJ and the beam waist is chosen such that the damage threshold of 10 GW/cm^2 [86] is not surpassed. In order to exploit the total remaining pump energy of 11.5 mJ in the second OPA stage, the pump beam is enlarged to 8.5 mm. A ZGP crystal cut at 55.4° with an aperture of 15×15 mm^2 in OPA 2 is used. The phase matching angle of OPA 2 is given for the longest signal wavelength. When the signal is tuned to lower wavelengths, this angle needs to be slightly adjusted. Between the 2.9 µm and 3.2 µm signal the difference in phase matching angle is 2° for OPA 2. This correction is negligible in the first OPA stage as the phase matching bandwidth supports the non-collinear amplification of all signal wavelengths simultaneously.

The parametric amplification process is examined with the programme *Sisyfos* (Simulation System For Optical Science) [81] which solves the nonlinear wave equation for Gaussian beams in the slowly varying envelope approximation (SVEA). With this programme, the nonlinear propagation and interaction between two input beams of different energies and transversal intensity profiles in spatial and temporal frequency space, creating a third output beam, are simulated. The results are summarized in Fig. 6.2 showing the amplified signal and corresponding idler spectrum after two amplification stages as implemented in the setup. All idler pulses have a bandwidth ranging from 3.9 THz for the shortest idler to 4.3 THz for the longest. Only the minor adjustment of the OPA 2 crystal angle is necessary to support amplification throughout all the spectrum. In addition, the comparison between the seed, the output of OPA 1 and OPA 2 confirms the broad phase matching bandwidth and shows no sign of gain narrowing through all amplification stages. Fig. 6.3 shows the simulated spectra for the shortest and longest signal wavelength. In conclusion, the shift of the signal wavelength does not degrade the output of OPA 2 and requires a 2° angle adjustment to support 1 mJ signal and idler output energy.

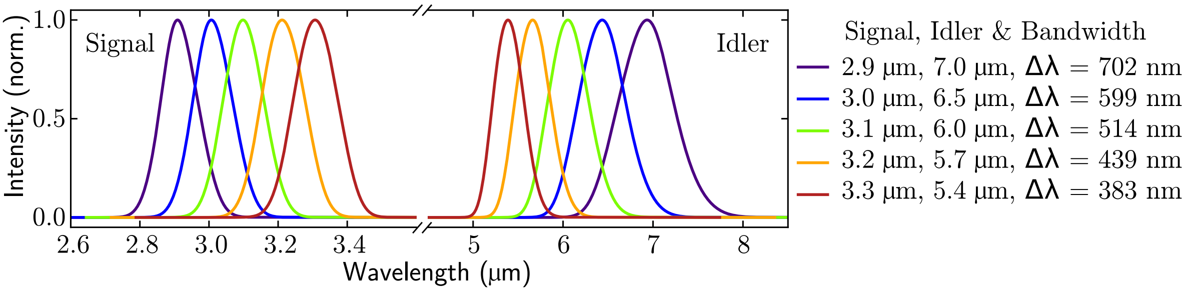

Figure 6.2: Simulation of 2-stage OPA using *Sisyfos* pumped at 2.05 µm based on ZGP for implemented configuration for the different signal wavelengths.

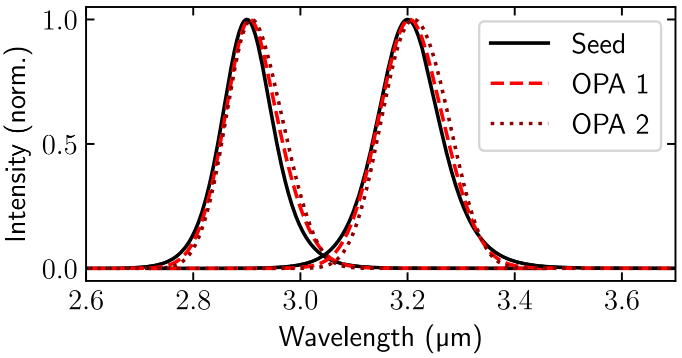

Figure 6.3: Simulated spectrum for 2-stage OPA pumped at 2.05 µm based on ZGP for the 2.9 µm and 3.2 µm signal. The simulation confirms that the entire seed spectrum is amplified without showing any signs of gain narrowing for all input seed wavelengths.

The temporal overlap between the signal and the pump pulses is crucial to ensure stable operation and frequency mixing. Thermal drifts stemming from the ambient surrounding as well as from heating of optical components lead to optical path differences and a changing delay between the pulses. Thermal expansion of the Ho:YLF crystal inside the regenerative amplifier seems to be the most crucial component which diminishes over a warm-up time of 3 h. However, a constant temporal delay shift between the pump and the signal is observable along a whole operation day if not actively controlled. The temporal shift translates into a decrease of output energy as well as into a drift of the amplified wavelengths which is disadvantageous for applications. In order to perform long-term energy stability measurements or performing a FROG measurement with a monochromator, which takes up to 2 h depending on the resolution, the delay has to be tracked and adjusted during operation.

The delay stage in front of OPA 1 sets the temporal overlap between the signal and the pump. Namely, the signal path is elongated and shortened which transfers into a temporal shift with respect to the pump pulse. In this system, as the signal path is changed, the temporal overlaps in both OPA stages are influenced simultaneously. This implementation is different from the system in [139] in which the pump path is shifted and synchronization between all three OPA stages is required. This makes stable operation more complex. The present system requires only one stage to be adjusted.

A partial reflection of the amplified uncompressed signal behind the second OPA stage generates second-harmonic (SH) light in 80 µm GaSe. The generated SH spectrum lies between 1.4 µm and 1.6 µm for which reliable near-infrared spectrometers exist. The process does not require a great efficiency as a small fraction of SH light is sufficient for spectral analysis. The fundamental beam is removed with an adequate short-pass filter and the remaining SH light is coupled into a fibre spectrometer (Ocean Optics NIRQuest, 900 nm - 2.5 µm). A Python based programme records the SH spectrum and performs a Gaussian fit. After averaging over 5 measurements, the central wavelength is calculated and compared with the target wavelength. Depending on the spectral offset, the delay stage in front of the first OPA stage is moved in steps of 0.01 mm ($\Delta t = 67$ fs). The process is repeated until the measured wavelength differs from the target wavelength by less than 2 nm. After a pause of 30 s, the measurement cycle restarts. This is an easy way to ensure timing stability successfully following the warm-up process. As a side note, the necessary spectrometer is clearly quite expensive for solving a timing issue, but it is easy to align and offers flexible operation over a broad spectral range.

6.2 Spectral characterization

The combined signal and idler energy amounts to 1.2 mJ behind the second OPA stage. The idler energy of up to 400 µJ surpasses the highest energy for reported tunable OPAs beyond 4 µm so far by one order of magnitude [22, 39]. The change of signal wavelength not only shifts the idler wavelength, but also redistributes the energy between the two pulses. This is, the ratio between signal and idler changes and the longer the idler wavelength, the lower its energy. The signal and idler output spectra were recorded with a scanning monochromator equipped with a HgCdTe detector (Horiba) and are shown in Fig. 6.4. The tunable signal pulses inherently transfer to the idler spectrum which extends from 5.4 to 6.8 µm. The bandwidth exceeds 4 THz for all idler spectra and supports a Fourier-limited pulse duration of 80 fs. However, the water vapour absorption in this spectral region increases the complexity of handling MWIR pulses. Also, the transmitted spectrum of the signal at the smallest wavelength (Fig. 6.4, blue curve) is limited by the anti-reflection coating of the used mirrors. The dip in the spectrum is therefore an artefact and not stemming from the amplification process or its limited bandwidth.

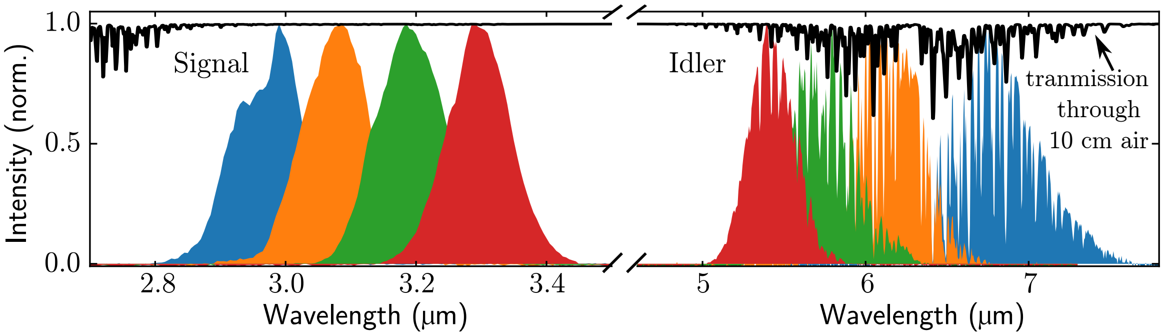

Figure 6.4: Measured spectrum of signal and idler pulses, color code transfers between signal and corresponding idler. The signal is tuned between 3.0 µm and 3.3 µm which translates into an idler covering 5.4 µm to 6.8 µm. The atmospheric absorption (transmission through 10 cm air) is shown by the black line, explaining the structured idler spectrum.

6.3 Temporal characterization

The pulsed nature of the signal and the idler are first confirmed by an autocorrelation (AC) measurement in an home-built autocorrelator containing $AgGaS_2$ (AGS) as the SH crystal. The autocorrelation trace revealing a pulse duration of 1.3 ps for the uncompressed 3 µm signal is shown in Fig. 6.5. This pulse duration agrees with the calculated stretching ratio in the bulk material. The idler pulses are compressed in two uncoated CaF_2 prisms both mounted on translation stages. For different idler frequencies, the amount of compression material changes due to the different dispersion values leading to different GVD and TOD values for the signal and idler wavelengths. Tab. 6.2 summarizes the calculated compression material. The idler at 5.4 µm requires 41 mm CaF_2, whereas the idler at 6.8 µm only 14 mm, according to calculations.

λ_{signal} (µm)	λ_{idler} (µm)	CaF_2	GDD (fs^2)	TOD (fs^3)
2.9	7.0	14 mm	-27.2×10^3	380×10^3
3.0	6.5	21 mm	-31.1×10^3	392×10^3
3.1	6.0	31 mm	-34.4×10^3	391×10^3
3.2	5.7	41 mm	-38.9×10^3	415×10^3

Table 6.2: GDD and TOD values for corresponding idler wavelength and required compression material.

The autocorrelation trace in Fig. 6.6 shows a compressed pulse duration of 135 fs for the 5.4 µm idler. The difference between the measured pulse duration and the theoretical Fourier limit is attributed to the structured spectrum due to atmospheric absorption and the uncompensated higher order dispersion. Both constraints prohibiting compression close to the Fourier limit are addressed in the following section.

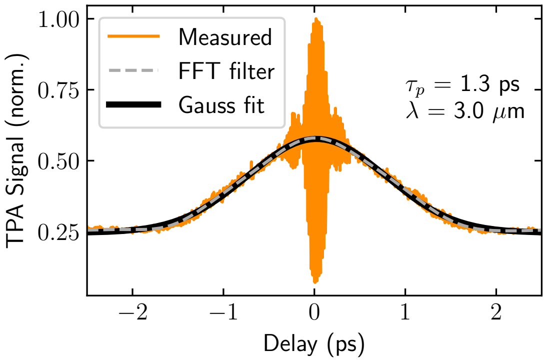

Figure 6.5: Autocorrelation measurement of amplified signal behind 2^{nd} OPA stage at 3.0 µm, uncompressed, recorded with mini TPA (APE).

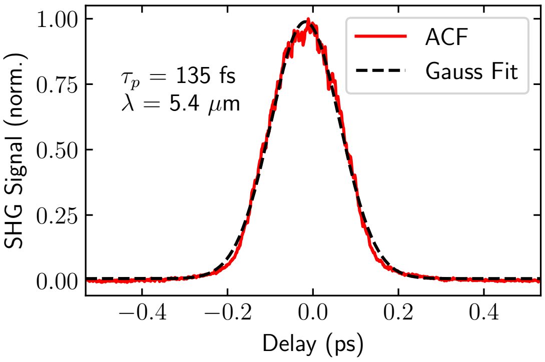

Figure 6.6: Autocorrelation measurement of idler pulses behind 2^{nd} OPA stage at 5.4 µm, in ambient condition (RH: 40 %) after compression in a CaF_2 prism pair, recorded with Pyrocam.

6.4 Precise phase shaping with AOPDF

The generation of ultrashort pulses requires a precise phase control. In the parametric process the phase of the pump and the signal are imprinted on the idler phase. If the idler spectrum supports femtosecond pulse durations, the chirp of the idler stemming from the pre-chirped signal pulse requires compensation where the second and third order phase have the largest influence on pulse duration. Indirect pulse shaping is one approach to overcome this problem [140–142], where the signal pulse is phase corrected prior to amplification such that the idler phase is compensated after bulk compression. Such a phase pre-shaping can be implemented via different techniques and devices. This MWIR OPCPA employs an acousto-optic programmable dispersive filter (AOPDF, Dazzler, Fastlite) [143–145] which is flexible in use. It imprints a polynomial phase up to the forth order onto the signal seed pulses. The second order phase can to large extent be compensated by bulk material only, as the sign of the GVD is reversed between signal and idler in the parametric process. It is therefore possible to use the same material for the signal stretching and the idler compression. The third order, however, leading to pre- or post-pulses in the temporal domain, is not reversed in the parametric process and adds up to even larger values with the compression material. Third order values of several $10^6\,\mathrm{fs}^3$ are expected in such systems. The AOPDF offers an elegant way to compensate third-order phases without modifying the setup. Additionally, it can add GDD only, compared to bulk material where GDD comes always with TOD. The amount of material required for stretching can therefore be reduced. The maximum amount of stretching and compressing material is generally limited by the maximum TOD that can be pre-compensated by the AOPDF on the signal pulse.

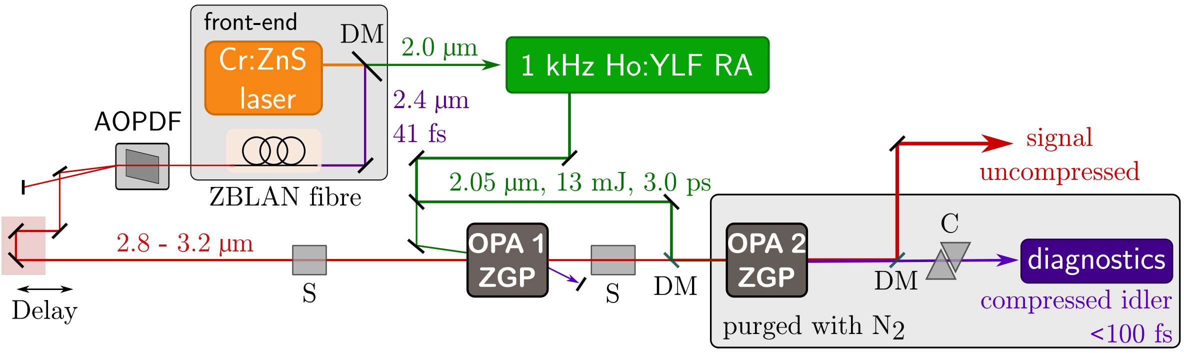

Figure 6.7: Two stage OPCPA setup based on ZGP including the AOPDF (Dazzler, Fastlite) for precise phase shaping and idler output purged with nitrogen. DM: dichroic mirror, S: stretcher, C: CaF_2 compressor.

An improved version of the previous setup is depicted in Fig. 6.7. It contains the same front-end with the Cr:ZnS oscillator and the fibre, the same Ho:YLF pump and keeps the same phase matching properties for OPA 1 and OPA 2. The implemented AOPDF for precise phase control of the signal is added behind the front-end fibre prior to OPA 1. One drawback of the AOPDF is that the throughput reduces the signal seed to 20 % of its initial value for the first OPA stage. In order to balance the lower seed energy, the beam sizes are slightly reduced by 20 % in OPA 1 in order to reach the same amplification energies as the setup without AOPDF. The second OPA stage, the autocorrelator and the spectrometer, as well as all beam paths, are put into a housing and purged with nitrogen in order to reduce the atmospheric absorption lines on the idler spectrum.

The idler spectra in nitrogen atmosphere are recorded with the same monochromator (iHR320, Horiba), see Fig. 6.8. The vapour absorption between 5.5 and 7 µm is too dominant to eliminate all spectral features by purging only. Modulations on the spectra are still visible and more prominent for longer idler wavelengths. Still, the pulses all support bandwidth $\geq 3.6\,\mathrm{THz}$ and the total intensity on the spectrometer remarkably increased with decreasing relative humidity. Similarly, the pulse duration is reduced with better purging. As a first approach, the theoretical TOD value was imprinted on the signal pulses and the autocorrelation trace was recorded with a home-built autocorrelator based on a $AgGaS_2$ crystal. GVD and TOD applied by the AOPDF were optimized with the AC trace. The shortest pulse duration of 98 fs was found for a TOD value of $1.54 \times 10^6\,\mathrm{fs}^3$. To confirm the well-compressed pulse duration, the second-harmonic (SH) frequency resolved optical gating (FROG) trace of the idler pulses were recorded in the same AC setup extended by a monochromator. As there are no spectrometer of the SH wavelength available, the monochromator was the only way to record the spectrum. This entails a long measurement time as for every delay step, a measurement time of 40 s is required to record the whole spectrum. In total, the FROG measurement lasted about 1 h. The measured and retrieved traces as well as the pulse and phase evaluation in temporal and spectral domain are shown in Fig. 6.9. The measured trace (Fig. 6.9(a)) shows a clean pulse shape with no sign of higher order dispersion or temporal pre- or post-pulses. The retrieved FROG trace (Fig. 6.9(b)) has an error of 0.67 % compared with the measurement and is in reasonable agreement with the experiment. The retrieved temporal pulse duration (Fig. 6.9(c), red curve) of 99 fs is close to the Fourier limit of 85 fs with a flat phase (green curve). The retrieved spectrum (Fig. 6.9, red curve) matches the measured spectrum (grey shaded, recorded with APE wavescan, non-triggered, structure attributed to repetition rate) as shown in Fig. 6.9(d).

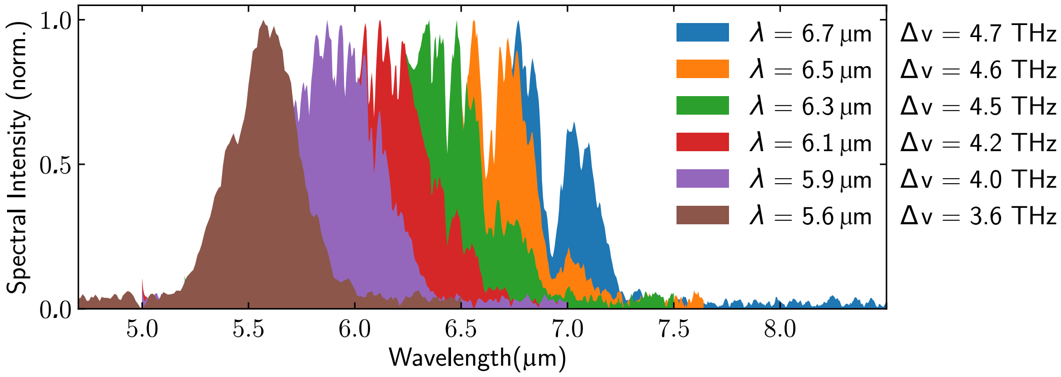

Figure 6.8: Measured spectrum of tunable idler pulse in nitrogen purged surrounding with the possibility of phase pre-shaping with Dazzler. In analogy to Fig. 6.4.

Finally, to prove the usefulness of the OPCPA system to perform experiments, the stability of the system was recorded. Fig. 6.10 shows the output energy of the 5.4 µm idler over 30 min. It has a mean value of 401 µJ and a root-mean-square deviation of 2.1 %. The inset of the figure shows the corresponding intensity profile. It shows no sign of saturation, but has an intensity structure which can be attributed to scattering of the lines of ZGP crystal growth. This is inherently stemming from the crystal itself. Lately, crystals of improved quality without growing lines have are available to us and could be used instead [51].

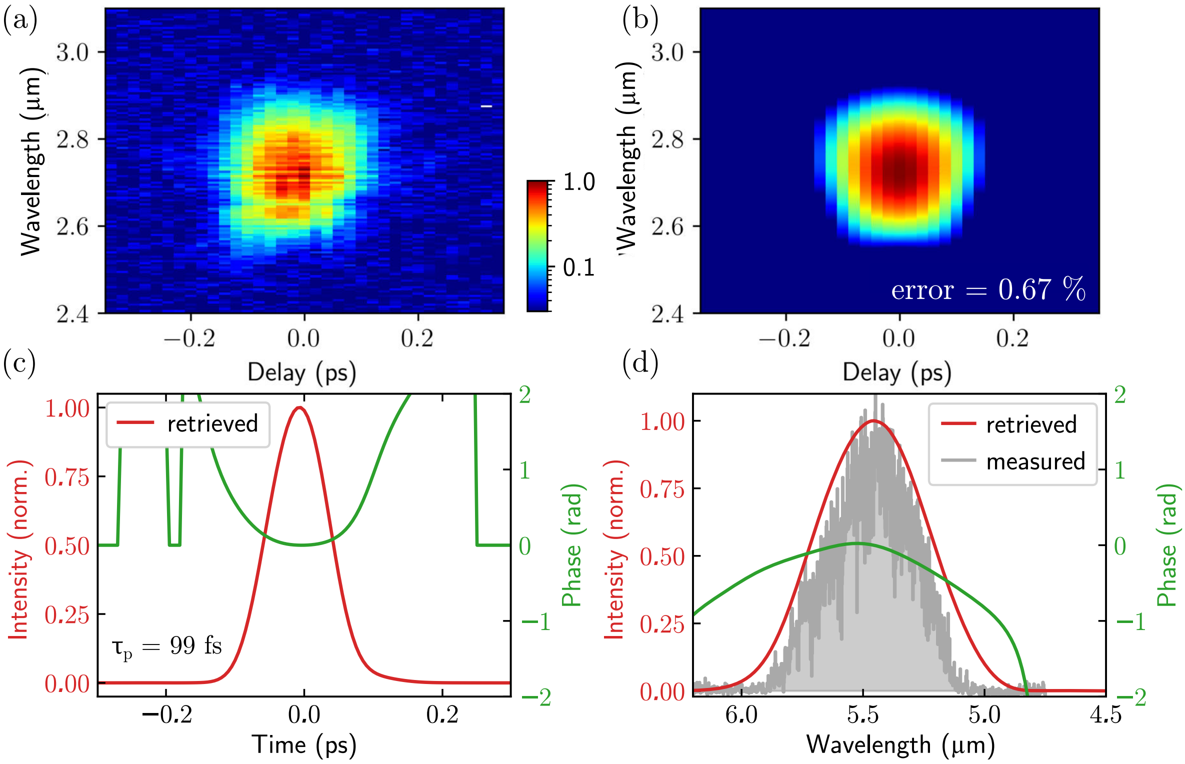

Figure 6.9: Characterization of idler pulses with home-built FROG setup, based on $AgGaS_2$ and recorded with monochromator (Horiba): (a) Measured and, (b) retrieved FROG trace, (c) retrieved pulse and phase in temporal domain, (d) retrieved pulse and phase in spectral domain, and measured spectrum (with APE wavescan) with grey background. The structure of the spectrum is not real and can be attributed to the repetition rate on the rotating grating inside the spectrometer.

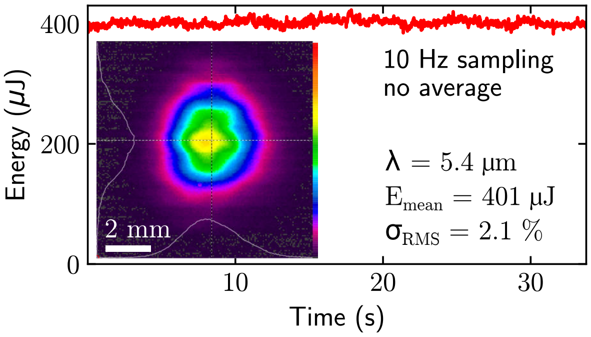

Figure 6.10: Long-term energy measurement for idler at 5.4 µm behind OPA 2 with root-mean-square stability of 2.1 %. Inset: Idler intensity profile, recorded with Pyrocam.

7

Long-wave infrared OPCPA

The mid-infrared spectral range is followed by the long-wave infrared (LWIR), spanning from 8 to 15 µm where a wide range of molecules have vibrational absorption lines. This spectral region is significant for molecular vibrational spectroscopy, metrology [11], trace-gas detection [146], biomedical diagnostics [6, 7] or food analysis [5], mostly relying on Quantum Cascade Lasers (QCL) emitting several milliwatts of output power. These types of lasers are broadly tunable across the infrared region, but emit pulses in the ms range with sub-µJ energies. In contrast, high power applications and material processing rely on CO_2 lasers which are the working horses at the wavelength of 10 µm delivering a peak power in the GW range with pulse energies of hundreds of kJ. However, the linewidth of these laser systems is heavily dependent on the gas-pressure of the active medium and restricted to the narrow bandwidth of the vibrational bands of the molecules [147]. Typically, CO_2 lasers have pulse durations of ≥ 100 ps. Producing pulses below 1 ps requires nonlinear post-compression and the current record of 500 fs has been reached with tremendous effort [18].

Laser systems providing pulses with fs-duration, µJ-energy at kHz repetition rates in the wavelength region beyond 10 µm could close the gap between the properties of QCLs and CO_2 lasers and open new horizons for time-resolved nonlinear spectroscopy. However, the number of systems in this spectral range is very limited. The reported sources use difference-frequency generation (DFG), intra-pulse DFG or OPA, all relying on driver sources at 800 nm or 1 µm. Very recently, in 2022, two groups reported on the generation of 10 µJ pulses with fs duration at 10.9 µm [23] and 11.4 µm [51] and have set the new record in terms of energy and peak power, after 20 years staying below 1 µJ. Tab. 7.1 summarizes the most important publications on systems aiming for this parameter range. These systems with NIR front-ends have generated few µJ energies with fs-duration in the kHz-range, not overcoming 145 MW of peak power.

Using a 2 µm driver offers better phase matching conditions for LWIR generation, as discussed in sec. 3.4.1. The generation of high peak power few-cycle pulses in the LWIR with an OPCPA using a 2 µm pump source has been explored numerically [148]. This article studies the parametric amplification in ZGP, GaSe and AGSe and presents promising phase matching bandwidths with Fourier limits down to 100 fs. This corresponds to 2.5 cycles for a 12 µm pulse.

λ	τ	E	P_p	f	crystal	Process	Driver	
12 µm	190 fs	1.4 µJ	6.9 MW	1 kHz	$HgGa_2S_4$	DFG	Ti:Sa	[47]
12 µm	190 fs	1.2 µJ	5.9 MW	1 kHz	$AgGaS_2$	DFG	Ti:Sa	[47]
12.5 µm	115 fs	0.3 µJ	2.5 MW	1 kHz	GaSe	DFG	Ti:Sa	[48]
13.5 µm	46 fs	0.4 µJ	8.2 MW	1 kHz	GaSe	OPA	Ti:Sa	[49]
10.3 µm	60 fs	1.1 µJ	17 MW	10 kHz	GaSe	IPDFG	Yb:YAG	[50]
10.9 µm	65 fs	10 µJ	145 MW	10 kHz	GaSe	DFG	Yb	[23]
11.4 µm	140 fs	10 µJ	67 MW	1 kHz	GaSe/AGSe	DFG	MWIR OPCPA	[51]

Figure 7.1: Overview of the most relevant publications on femtosecond, µJ laser systems beyond 10 µm listing the central wavelength λ, the pulse duration τ, the pulse energy E, the peak power P_p, the repetition rate f, the nonlinear crystal, the process for generating the pulses and the type of driver front-end.

Unfortunately, this proposal is still lacking implementation. To the best of my knowledge, generating LWIR pulses in an OPCPA has so far remained unexplored.

For LWIR generation, the transparency range of the nonlinear crystal needs to span from at least 2 µm up to 14 µm to allow the transmittance of the pump and the entire generated idler spectrum. The existing crystals have, however, limited availability and transparency range. Besides the well-known nonlinear infrared crystals ZGP, GaSe and AGSe, new crystals are developed and characterized. The new barium based nonlinear crystals $BaGa_4S_7$ (BGS), $BaGa_4Se_7$ (BGSe), $BaGa_2GeS_6$ (BGGS) and $BaGa_2GeSe_6$ (BGGSe) transparent in the MWIR and LWIR region have recently attracted much attention [85]. These crystals all support 1 µm as well as 2 µm pumping and transmit wavelengths up to 10 µm (BGGS and BGS) or 16 µm (BGGSe and BGSe). Unfortunately these crystal are not yet commercially available.

The following LWIR OPCPA relies on the well-known crystal gallium selenide. GaSe has a relatively high second-order nonlinear index of $d_{\text{eff}} = 54\,\text{pm/V}$ and a larger damage threshold [51] than ZGP [86] which is promising for high gain applications. Its band gap at 2.1 eV ($\lambda = 0.59\,\mu\text{m}$) limits the pump intensity at 1 µm due to two-photon absorption, and makes a pump wavelength at 2 µm much more suitable as discussed in sec. 3.4.1. GaSe has a structure consisting of stacked crystal layers which dictate the cleaving axis. Hence, this crystal cannot be cut to the desired phase matching angle and needs to be tilted in the setup to ensure phase matching. The material is soft and single crystal layers can easily be pealed off which prohibits anti-reflection coating. Crystals with a maximum aperture of 7x7 mm^2 are commercially available which limits the size of transmitted beam profile and the maximum pump energy. The tilt of the crystal for the parametric setup is additionally reducing the aperture and consequently the largest transmissive beam diameter.

7.1 Experimental setup

The presented source for the generation of LWIR radiation beyond 10 µm is the first OPCPA in this wavelength range [126]. Its setup, shown in Fig. 7.2, comprises the front-end based on a fs Cr:ZnS oscillator (see Chapter 5), a regenerative amplifier (RA) at 2.05 µm wavelength with 13 mJ energy and 3.0 ps pulse duration as the pump (see Chapter 4) and three nonlinear parametric stages based on the nonlinear crystal GaSe. The setup has two outputs at the wavelengths of 2.4 µm and 11.4 µm generated at the same time, both with µJ-energy, fs-duration at a 1kHz repetition rate.

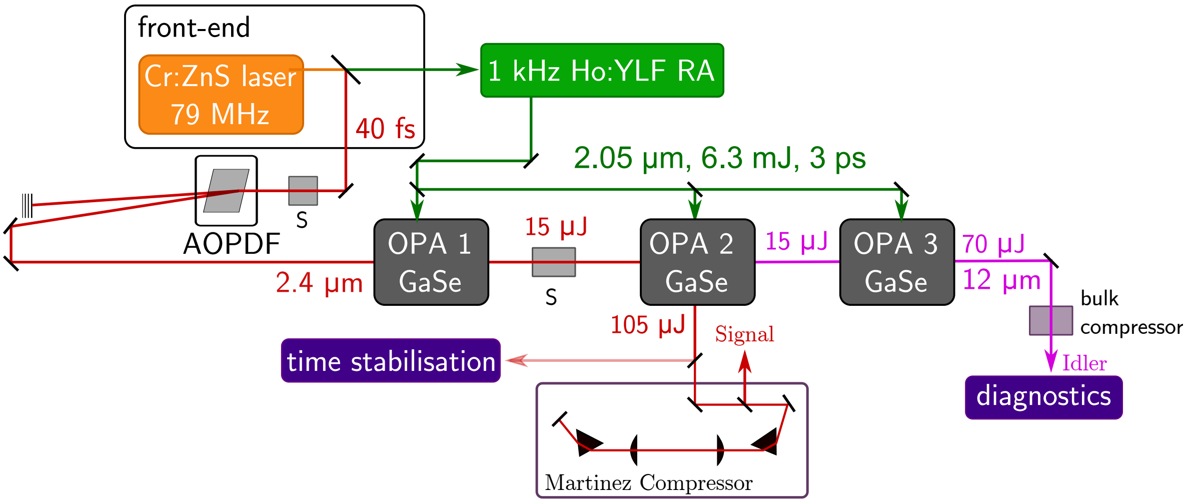

Figure 7.2: Setup of LWIR OPCPA comprising the front-end with the fs Cr:ZnS oscillator, a phase shaper (AOPDF) for the signal pre-shaping, the pump based on a regenerative amplifier and three OPA stages with the nonlinear crystal GaSe.

The signal pulses are stretched in 40 mm Al_2O_3 and subsequently phase modulated in an AOPDF (Fastlite, Dazzler) prior to amplification resulting in a pulse duration of 1.5 ps. The first OPA stage is equipped with a 2 mm thick GaSe crystal pumped with 300 µJ. The beam size of the pump is set to 700 µm diameter in order to stay below the damage threshold of 50 GW/cm^2. This damage threshold has been determined experimentally as a lower limit and all OPA stages have been designed accordingly. A small angle of 0.5° (other than phase matching direction) is introduced between the pump and the signal for the separability of the two pulses and to prevent the second stage from being seeded with the SH light of the pump. Though the phase matching angle numerically does not support the generation of second-harmonic of the pump, this process is taking place, however, with lower efficiency and gets amplified in the second stage if not removed. The signal pulses are amplified from 2 nJ to 15 µJ and are used to seed OPA 2.

Between OPA 1 and OPA 2 another 90 mm Al_2O_3 rod is stretching the pulse duration further to 1.9 ps. It is built collinearly to ensure a proper non-dispersive idler beam profile. The pump energy on this stage is 1.8 mJ and generates a combined output energy of 149 µJ (signal and idler) in 1 mm GaSe. After the separation of the idler from the signal and the pump, the idler pulses seed, with 8 µJ energy, the non-collinear OPA 3 stage in 1 mm GaSe. The non-collinear angle is chosen as small as possible, since non-collinear phase matching supports a narrower bandwidth (see Fig. 3.4b). This angle is necessary as the beamsplitter required for separating the idler beam from the pump and the signal reduces the idler energy and the coating layer does not stand the pump intensity. Damage on the beam splitter has been observed and the AR-coating layers at the back fluorescence for the idler pulses at this energy. In the experiment, the non-collinear angle of 2° externally corresponds to $\theta_{nc} = 0.7°$ internally. The OPA 3 is pumped with 4.8 mJ leading to an idler centred at 11.4 µm with 70 µJ energy and a bandwidth of 0.84 µm. This spectrum supports a Fourier limited pulse duration of 170 fs.

In all three stages, type II phase matching at 12.2° is used. This corresponds to an external angle of 36°. In this context, the crystal has to be tilted as the cleaving angle of the nonlinear crystal is restricted to the c-axis. A round external beam transfers into an elliptically beam internally. For the given phase matching angle, the intensity profile is in one direction 20 % larger than in the other. Numerically, type I phase matching is also allowed for the generation of LWIR idler pulses, but has a much narrower linewidth for the spectral range above 10 µm, see Fig. 3.10 in Sec. 3.2.3. For both phase matching types, the signal is polarized in ordinary direction, whereas the idler takes ordinary polarization for type I and extra-ordinary polarization for type II. This means that the polarization direction of the pump and the signal supports both phase matching types. In order to exclude the possibility of generating the idler in ordinary and extraordinary direction simultaneously, the output energy of the idler pulses behind OPA 2 was recorded in dependence of the external crystal angle, see Fig. 7.3. Type I phase matching has a slightly higher nonlinear coefficient d_{eff} which is confirmed by the higher output energy. The zero-energy point between the two angles is dividing the two phase matching types and idler polarization directions. The clean polarization of the idler after amplification has been confirmed with a polariser.

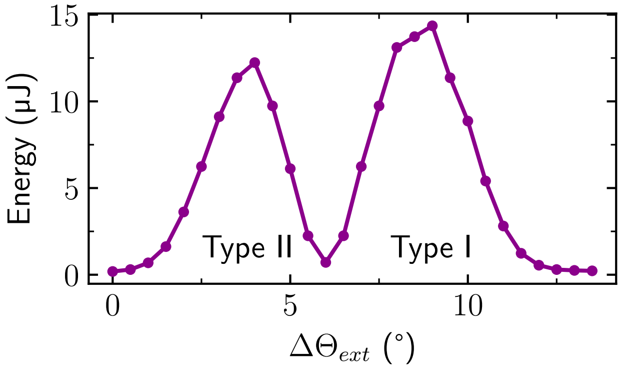

Figure 7.3: Measurement of idler energy behind 2nd OPA stage in dependence of the crystal angles, tuning over type I and type II phase matching.

As the GaSe crystals are all uncoated, the occurring Fresnel reflection lead to a reduction of 16 % for the p-polarized pump energy and 27 % for the signal seed energy, prior to amplification for the external angle of 36°. Internally, the Fresnel reflection at 12° leads to a transmittance of $\leq 80\,\%$ for all three beams, no matter the polarization direction. Taking this into consideration, the internal pump-to-idler conversion efficiency amounts to $^{87\,\mu\text{J}}/_{5.8\,\text{mJ}} = 1.5\,\%$. Subsequently, the idler and signal pulses are characterized in spectral and temporal domain.

7.2 Spectral analysis

The first OPA stage exhibits the highest gain, has the thickest nonlinear crystal of all OPA stages, and can be subject to severe gain narrowing, if badly designed. This affects the bandwidth of the whole system and consequently, the FTL pulse duration of the idler pulses. Ch. 3 thoroughly studies the best implementation for this stage which is a collinear type II phase matching for the generation of LWIR pulses in GaSe. Accordingly, the amplified signal spectrum behind OPA 1 is measured and shown in Fig. 7.4. The data show no sign of gain narrowing for different output energies and the bandwidth remains constant between 1 µJ and 15 µJ. Knowing that the seed has 2 nJ energy and the amplified signal has 15 µJ, this OPA stage exhibits a gain factor of up to 7500, in good agreement with the simulation presented in sec. 3.4.1. From the measurement, it is also apparent that the amplified spectrum is not comprising the whole seed spectrum and supports wavelengths beyond 2.4 µm only. This reduced bandwidth is mainly stemming from the group velocity mismatch and the corresponding parametric gain coefficient $\mathrm{sinc}^2(\Delta kL/2)$ scaling with the k-vector mismatch Δk and the thickness of the crystal L, see sec. 3.2.3.
As an initial try, all three OPA stages are seeded with the signal and its spectrum is recorded, shown in Fig. 7.5. The first OPA stage reduces the bandwidth down to 97 µm which narrows further to 77 nm and 73 nm in the second and third OPA stage with 1 mm GaSe, respectively. As already mentioned, the different group velocities are responsible for the narrow bandwidth and the supported bandwidth increases for thinner crystals (see sec. 3.2.3).

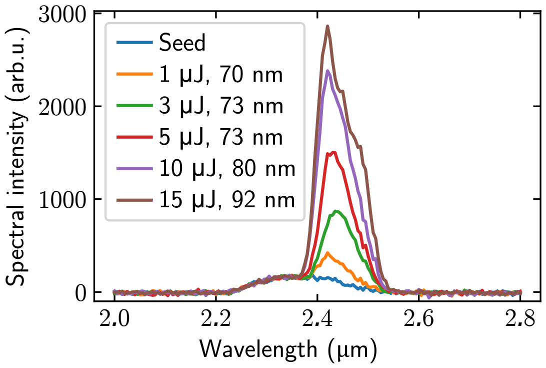

Figure 7.4: Measurement of the signal spectrum behind the 1st stage with GaSe for different output energies.

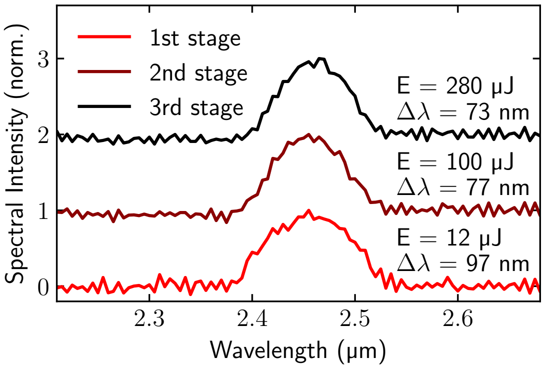

Figure 7.5: Signal spectrum of first, second and third OPCPA stages, all seeded with the signal pulse.

The spectrum of the signal and the idler are recorded for the setup presented in Fig. 7.2. Fig. 7.6 shows the signal seed and the amplified spectrum behind the first and the second OPA stage, the latter with a bandwidth of 79 nm (larger gain in OPA 2 than shown in Fig. 7.4). The shaded grey area indicates the parametric coefficient for the implemented type II phase matching in 2 mm GaSe. The idler spectra behind the second (blue curve) and the third (violet curve) stages are shown in Fig. 7.7. The simulated curve (dashed, black line) is nicely recovering the measured spectra. The spectral bandwidth of 0.84 µm supports a Fourier limited pulse duration of 170 fs. The experimental idler spectra exhibit slight spectral modulations which are attributed to a weak interference of the main and a residual idler pulse, the latter originating from reflections at the uncoated surfaces of the GaSe crystal. The idler spectrum behind OPA 1 cannot be measured as the energy is too low and the profile spatially dispersive.

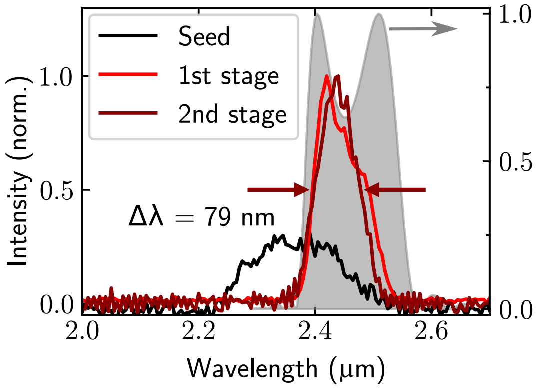

Figure 7.6: Signal spectra of LWIR OPCPA for the seed, the first and second OPA stage and parametric coefficient for type II phase matching at 12.2° in 2 mm GaSe (gray shaded area).

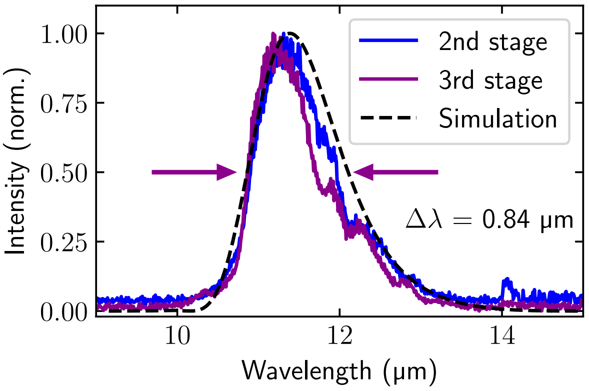

Figure 7.7: The corresponding idler spectra of the LWIR OPCPA behind the second and third stage. Both measured curves are in good agreement to the simulation (dashed line).

7.3 Temporal analysis

As a first step, the autocorrelation traces of the signal behind OPA 2 and the idler behind OPA 3 are recorded, both pulses without angular dispersion. The signal has negative GDD and requires a compression scheme introducing positive GDD. Therefore, using bulk material is not possible and a home-built Martinez compressor is used instead. It introduces second and third- order dispersion with two sapphire prisms on the signal behind OPA 2. It is built such that it adds $50 \times 10^3\,\mathrm{fs}^2$ GDD to the negatively chirped signal pulses. Due to the uncoated prisms and lenses, the compressor has a throughput of only 50 %. This value can be increased when using coated prisms and lenses in the Martinez compressor. The recorded collinear AC trace is recorded with a commercial autocorrelator (miniTPA, APE) and shown in Fig. 7.8. The pulse duration of 120 fs is close to the Fourier limit of 115 fs.

The idler is compressed in two 5 mm AR-coated ZnSe windows and two ZnSe lenses (necessary for the autocorrelation measurement) with a large beam diameter of >6 mm to avoid nonlinear absorption in the material. The idler pulse duration is measured in a home-built autocorrelator with a Pyrocam as the intensity detection unit. It is worth mentioning that this measurement was a challenge as adequate beam splitters for LWIR wavelengths are not available. Using thin silicon wafers instead has mislead initial characterizing experiments. Eventually, a D-shaped mirror was used as a hard-aperture beam splitter which has the advantage of reducing the number of transmissive optics in the AC and is considered the best solution. This beam splitting, however, always requires non-collinear geometry which makes initial adjustment quite challenging. Nevertheless, the idler AC trace was successfully recorded as shown in Fig. 7.9. A pulse duration of 185 fs is measured after optimization of the GVD and TOD values of the Dazzler. The trace does not show any residual signs of TOD, being close to the Fourier limit of 170 fs. The accompanied side pulses of the AC trace can be attributed to the uncoated

0.1 mm GaSe crystal serving as SH crystal. It stems from the Fresnel reflection inside crystal interacting with the main pulse after 1.8 ps. This is a measurement artefact and not a pre- or post-pulse of the idler.

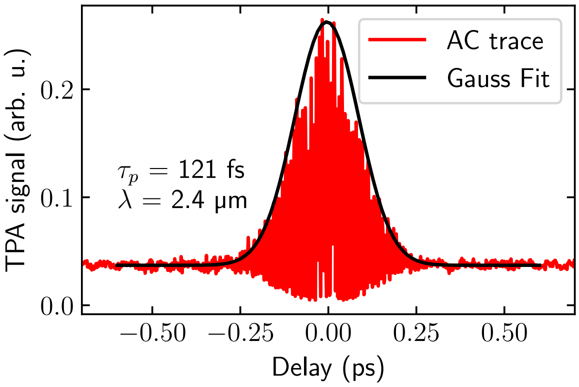

Figure 7.8: Autocorrelation of signal behind OPA 2 after compression in a Martinez compressor, recorded with the miniTPA (APE). The pulse duration is 121 fs (τ_{FTL} = 115 fs).

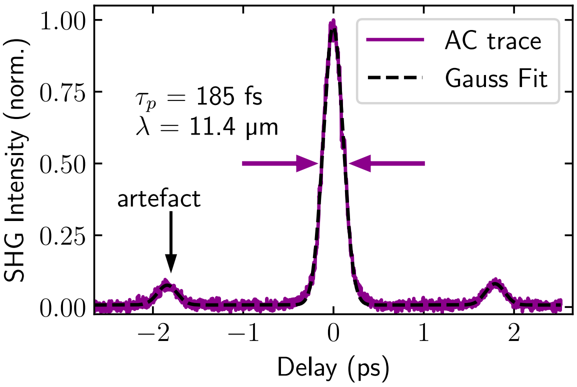

Figure 7.9: Autocorrelation of idler pulses behind OPA 3 after compression in bulk ZnSe showing a pulse duration of 185 fs (τ_{FTL} = 170 fs) in home-built autocorrelator.

7.4 FROG measurement and output stability

The phase-resolved evaluation of the idler pulses is conducted by replacing the Pyrocam at the output of the autocorrelator by a scanning monochromator to confirm the pulse duration of the AC measurement. The second-harmonic generation (SHG) frequency-resolved optical gating (FROG) trace is shown in Fig. 7.10 with a spectral resolution of 10 nm. The measured FROG trace in Fig. 7.10(a) is subject to a modulation on the spectrum which can be attributed to the uncoated GaSe SHG crystal inside the autocorrelator and is not a modulation on the idler pulse. It is the same effect that leads to the artefact satellite pulses in Fig. 7.9. This modulation cannot be reconstructed by the retrieval algorithm and is hence not visible there (Fig. 7.10(b)). The retrieved FROG trace deviates from the measurement by 0.4 %. The retrieved temporal pulse has a pulse duration of 185 fs (Fig. 7.10(c), red curve) which is close to the Fourier limit of 170 fs (black curve). This corresponds to less than 5 optical cycles for these LWIR pulses. The retrieved spectrum (Fig. 7.10(d)) has a flat phase (green curve) and is in good agreement with the measured one (grey area).

The output energy of the LWIR OPCPA system has been recorded over 80 min and shows an output power of 70.5 mW with a 1.7 % root-mean-square stability. Taking into account the 10 % of compression losses, the derived peak power amounts to 0.35 GW translating into a peak intensity of 8.4 TW/cm^2 when focussed to 100 µm. These output values surpass by far the parameters of published LWIR systems beyond 10 µm generated by DFG or OPA, see Tab. 7.1.

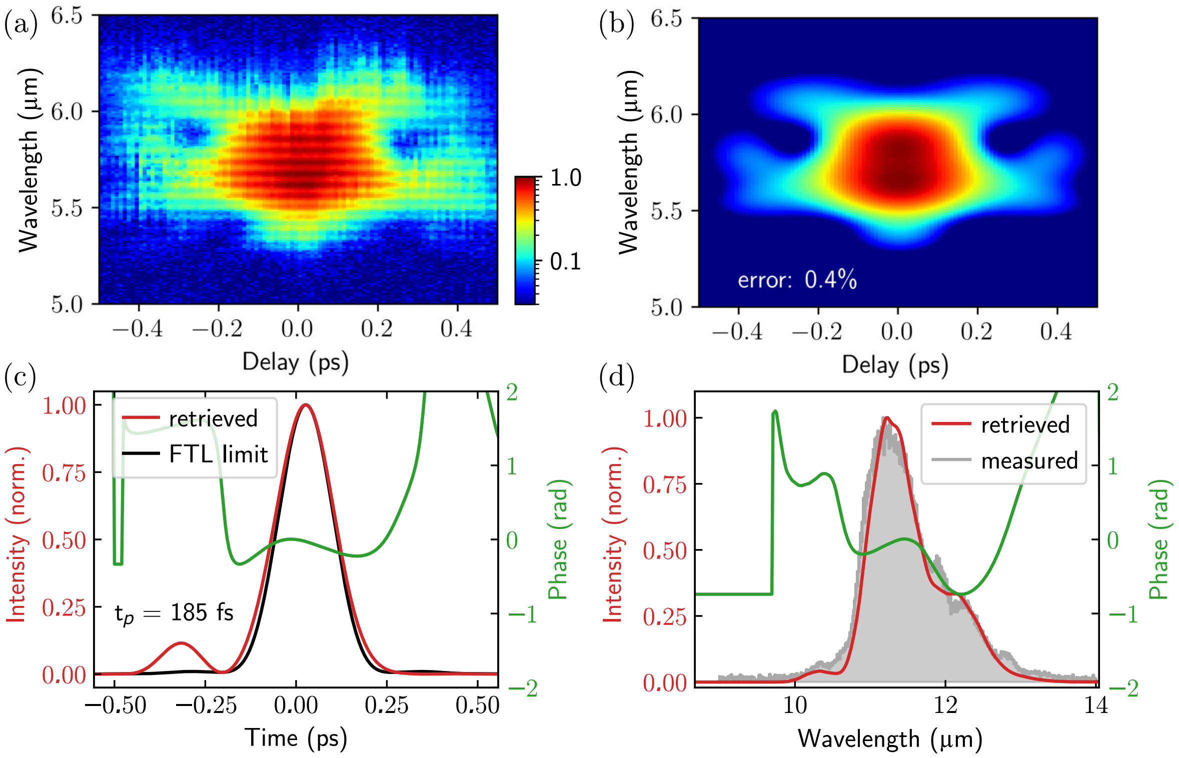

Figure 7.10: Measured and retrieved FROG traces for LWIR idler pulses at 11.4 µm behind OPA 3. (a) Measured trace, (b) retrieved trace with 0.4 % error, (c) temporal retrieval of 185 fs pulse duration ($\tau_{\mathrm{FTL}} = 170$ fs) and (d) spectral retrieval matching the measured spectrum (grey area).

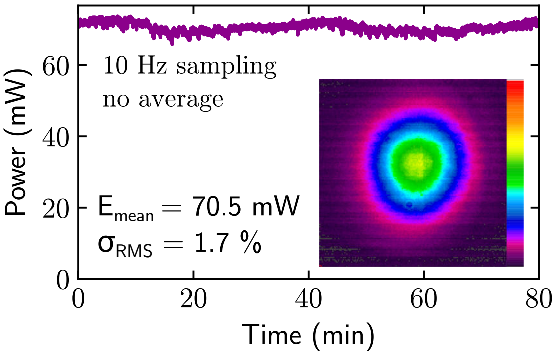

Figure 7.11: Long-term pulse stability of idler pulses behind OPA 3. Inset: far-field intensity distribution.

7.5 Comparison with simulation

Finally, it is possible to compare the experimental results with the simulations conducted in Ch. 3. The measured spectra deviate from the simulations, the latter suggesting a broader spectrum for the signal and idler pulses than measured. This might be due to an inaccuracy of the Sellmeier equations which are the basis for the parametric calculation. When comparing the simulation output for the Sellmeier coefficients provided by Kato et al. in 2013 [149] and Allakhverdiev in 2005 [150], the spectrum shifts and the bandwidth differs by a factor of 2. In [149], the authors have already shown a deviation of the phase matching behaviour from theory in GaSe for a near-IR OPCPA, therefore the extrapolation to the LWIR can expected to be even more inaccurate.

Still, the best agreement between simulation and measurement for the LWIR OPCPA in GaSe has been found with the Sellmeier values of Kato [149], a narrower input seed spectrum and a much lower effective nonlinearity of 30 pm/V. The simulation programme takes into account the beam profiles, walk-off angles, input energies, spectra and pulse durations. The spectra are shown in Fig. 7.12 and the corresponding energy and bandwidth are summarized in Tab. 7.1. From earlier comparison between experiments and simulations of the MWIR OPCPA in ZGP and their reasonable agreement [80], the performed calculations are in principle considered correct. The largest deviation is expected from the angular walk-off and the group velocity mismatch.

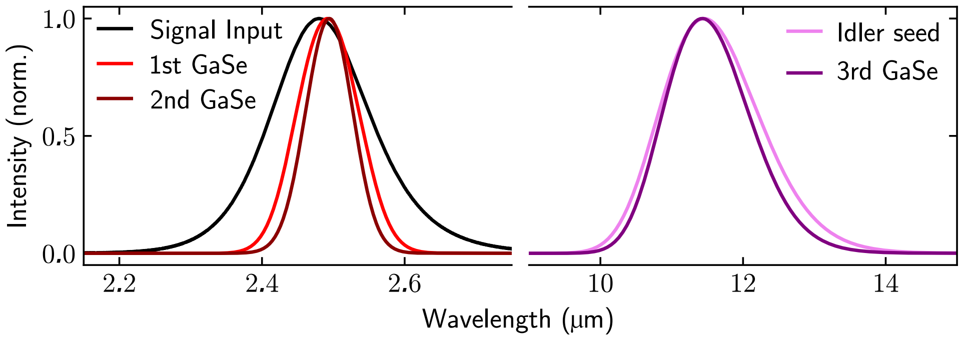

Figure 7.12: Simulation with best experimental agreement of three stage LWIR OPCPA based on GaSe with $d_{\mathrm{eff}} = 30\,\mathrm{pm/V}$, pumped at 2.05 µm with 50 GW/cm^2 and seeded at 2.4 µm. 1st stage with 2 mm GaSe and 2nd stage with 1 mm GaSe, both seeded with the signal, 3rd stage with 1 mm GaSe seeded with the idler.

Pump	Signal		Idler		d_{GaSe}
E_p	E_s	$\Delta\lambda$	E_i	$\Delta\lambda$	
0.28 mJ	15.4 µJ	100 nm	3.3 µJ		2 mm
1.6 mJ	92.6 µJ	77 nm	18.4 µJ	1.6 µm	1 mm
3.8 mJ	251.8 µJ		61.5 µJ	1.3 µm	1 mm

Table 7.1: Simulation for the implemented LWIR OPCPA configuration based on three stages with GaSe, pumped at 2.05 µm and seeded at 2.5 µm, calculated with $d_{\mathrm{eff}} = 30\,\mathrm{pm/V}$ using the Sisyfos code.

8

Nonlinear absorption of water

Librations, or hindered rotations, are playing an important role in energy dissipation in liquid water. Following librational dynamics in time, however, is a challenge due to the ultrafast energy dissipation in the hydrogen-bonded network [151, 152]. In the past, mainly the temporal dynamics of O-H bending and stretching vibrations have been investigated by femtosecond pump-probe measurements [12, 153, 154]. For the lifetime of librational excitations an upper limit of 100 fs was estimated but not measured directly so far [154].

The current LWIR OPCPA system is the first pump source that enables direct excitation of the librational L2 band with sufficient energy in order to expect a nonlinear transmission change. The L2 libration is a rotational mode around the axis shown as the dotted line in Fig. 8.1, hindered by the hydrogen bond network with the lowest moment of inertia among the other rotational modes. The resonances of liquid water in the mid-IR region, including the librational, OH-bending and OH-stretching modes are shown in Fig. 8.2. In this work, the librational L2 mode is excited with light pulses having a photon energy corresponding to the $v = 0 \rightarrow v = 1$ transition. So far, the peak intensities of laser systems in this spectral range with an energy of 10 µJ [23, 51] were too low in order to induce measurable nonlinear behaviour.

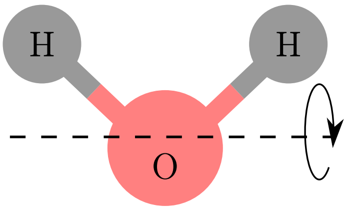

Figure 8.1: Librational L2 mode of a water molecule.

The potential of the novel LWIR source for ultrafast vibrational spectroscopy is demonstrated in this chapter. It presents a nonlinear transmission measurement where the librational (L2) mode at 660 cm^{-1} or 15.1 µm is directly excited with femtosecond pulses centred at 11.4 µm. An analysis of the intensity-dependent nonlinear transmission suggests a sub-20 fs decay time of this excitation. The estimate of the upper limit of the lifetime of the librational (L2) state is based on a rate equation model for an ensemble of two-level systems.

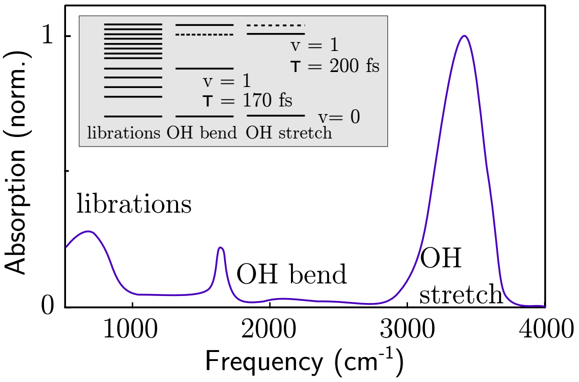

Figure 8.2: Absorption of different rotational bands in liquid water, including libration, OH-bending and OH-stretching modes and typical decay times. Modified figure taken from [154] (Fig. 1).

8.1 Experimental implementation

The water sample is irradiated with the output pulses of the LWIR OPCPA at 11.4 µm and a 185 fs pulse duration. The setup is shown in Fig. 8.3. Two identical cells made of two BaF_2 windows and a 12 µm spacer are prepared, one of which is filled with distilled liquid water. Since the output of the OPCPA is linearly polarized, the energy on the sample can be tuned by rotating a BaF_2 holographic wire grid polariser (Thorlabs, WP25H-B). A 50 mm AR-coated ZnSe lens is used to focus the laser beam to a spot size of 130 µm, measured by the knife edge method. The cell is moved out of focus and placed slightly before the minimal beam waist since the barium fluoride windows show fluorescence and white light generation if a certain energy threshold is exceeded. It was possible to find a spot size for which no fluorescence was visible and the experiment was conducted there ($2w_0 = 150$ µm). As a side note, diamond windows which were initially thought more suitable could not be used at all. Even at 50 % of the total energy, the windows showed black spots after irradiation indicating a local carbonization process.

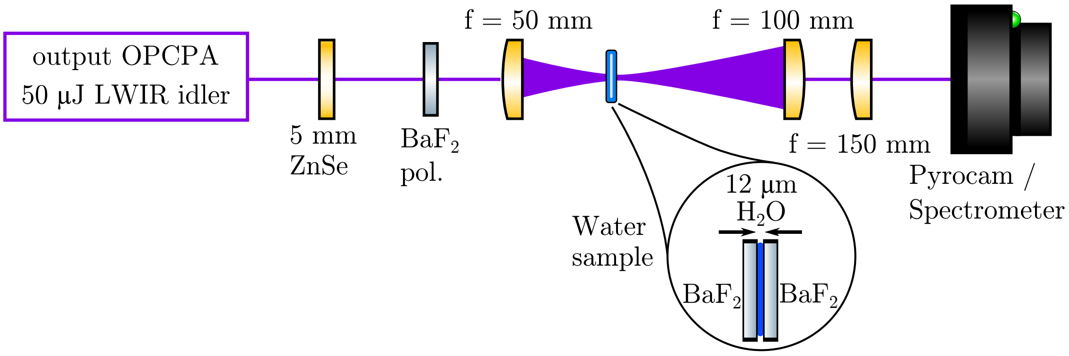

Figure 8.3: Setup of nonlinear transmission measurement of a 12 µm thick water sample between two 1 mm thick BaF_2 windows, irradiated with 200 fs long pulses at 11.4 µm. The ZnSe plate compresses the pulses, in addition to the dispersion of the BaF_2 polariser necessary for energy adjustment and the 50 mm ZnSe lens to reach a beam waist of 150 µm inside the water sample. Two ZnSe lenses project the transmitted light onto a Pyrocam (Spiricon) or spectrometer (Horiba).

After transmission through the sample, two AR-coated ZnSe lenses collect the transmitted LWIR light and focus it onto a Pyrocam (Ophir photonics, Spiricon, Pyrocam IIIHR) or a monochromator (Horiba, iHR320). The spot size on the camera is chosen such that it ensures linear detection across the entire excitation range. The induced dispersion of the polariser and the lens are taken into account and the pulse compression is corrected accordingly. Though compensating the dispersion of the additional optical elements by removing compression material, the final pulse duration in the water layer is calculated to be slightly longer, namely 200 fs.
The LWIR pulses overlap with the L2 absorption band of water, as shown in Fig. 8.4, where the pulse spectrum with and without water sample is plotted. Note that the displayed intensities are normalized in order to be comparable. The comparison between the incident and transmitted LWIR pulses shows a stronger absorption of the lower frequency components of the pulse spectrum which is in agreement with the absorbance of water (Fig. 8.4, black line). In particular, there is no nonlinear broadening of the pulse spectrum by self-phase modulation (white-light generation) in the very thin water film.

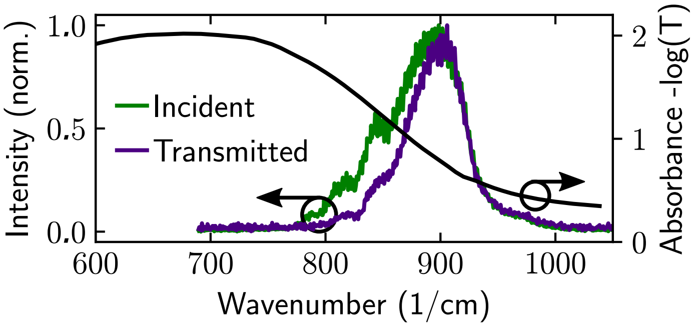

Figure 8.4: Normalized incident (green curve) and transmitted (purple curve) spectrum of LWIR pulses centred at 11.4 µm behind 12 µm thick water sample. Absorbance [155] of the librational band (shown in black) defined as $-\log_{10}(T) = \epsilon_0 cd$, where ϵ_0 the linear molar absorptivity, $c = 55$ mol/l the concentration of water and $d = 12 \times 10^{-4}$ cm the sample thickness.

The transmission is determined by dividing the number of counts on the Pyrocam with the water sample by the number of counts with the empty cell. The beam size on the camera is equal for both configurations but changes when freely propagating. The change of divergence induced by the BaF_2 windows is clearly visible. In the literature, the lower limit of the nonlinear refractive index of BaF_2 is measured to be 30×10^{-20} cm^2/W at 9.2 µm [156]. The error of the measurement is reduced by repeating the measurement 6 times with the empty cell and 12 times with the water cell. Every time the polariser is automatically turned by 10° which was initially calibrated. For a time of approximately 2 s, the mean value of the counts are taken and averaged over all repetitions.

The experimental result of the nonlinear transmission measurement of a 12 µm thick water cell is shown in Fig. 8.5. It shows a change of transmission of 1.4 % in the energy range between 2.1 and 27.6 µJ when irradiated with 200 fs LWIR pulses. This is the first measurement where the nonlinear transmission change by direct excitation of the L2 libration band is observed.

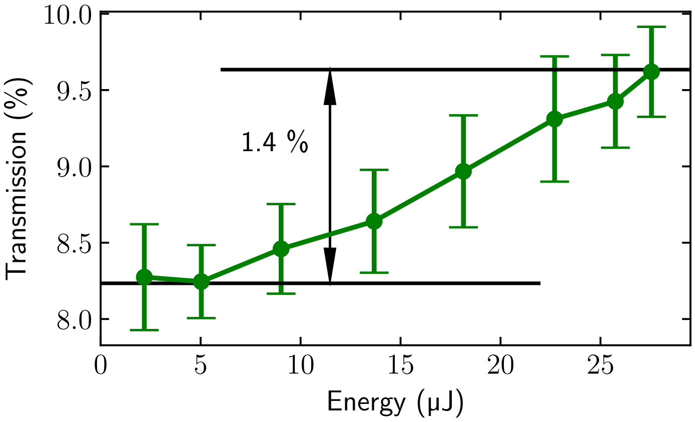

Figure 8.5: Experimental results of nonlinear transmission measurement of 12 µm thick water cell, irradiated with 200 fs LWIR pulses centred at 11.4 µm.

8.2 Theoretical approach

For the analysis of the experimental results, the libration is treated as a two-level quantum system with light-matter interaction in the incoherent limit. Here, the population densities of the two levels ν_0 and ν_1, the optical intensity of the incident light field I, the absorption cross section σ and the population relaxation time τ are the relevant quantities. The partial differential equations that describe the change of the population density n_1 and n_2 and the population inversion $\Delta n = n_2 - n_1$ are [157]

$$\begin{aligned}\frac{\partial n_1}{\partial t} &= \sigma(n_2 - n_1)\frac{I}{\hbar\omega} + \frac{n_2}{\tau}\\ \frac{\partial n_2}{\partial t} &= -\sigma(n_2 - n_1)\frac{I}{\hbar\omega} - \frac{n_2}{\tau}\\ \frac{\partial \Delta n}{\partial t} &= -2\sigma\Delta n\frac{I}{\hbar\omega} - \frac{2n_2}{\tau}\end{aligned}$$

where the last equation follows from subtracting the first equation from the second and using the total number of quantum states $n_0 = n_1 + n_2$. Consequently, the population inversion can be rewritten in terms of the light intensity as

$$\frac{\partial \Delta n}{\partial t} = 2\alpha\frac{I}{\hbar\omega} - \frac{n_0 + \Delta n}{\tau}, \tag{8.1}$$

where the absorption coefficient is defined as

$$\alpha(\omega, \Delta n) = -\Delta n \cdot \sigma(\omega), \tag{8.2}$$

with the frequency dependent absorption cross section $\sigma(\omega)$ of the $v = 0 \to v = 1$ transition. The coefficient α is proportional to the population inversion and can be calculated analytically

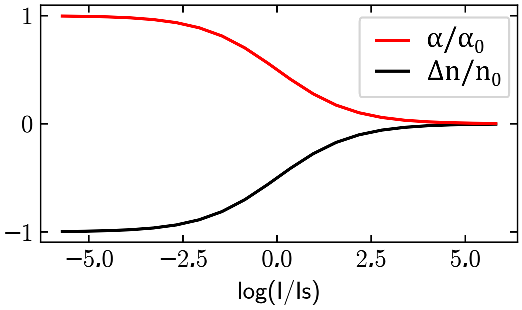

Figure 8.6: Stationary limit for population inversion and absorption as a function of the light field intensity.

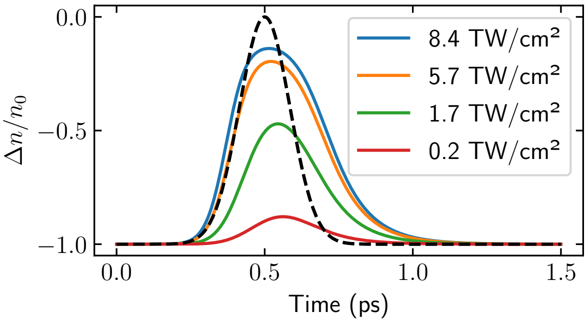

Figure 8.7: Time dependent population inversion for 200 fs pulse at different peak intensities and $\tau = 100\,\mathrm{fs}$ lifetime of the libration state. Excitation pulse profile shown by dashed line.

for the stationary limit. For $\partial\Delta n/\partial t$, the absorption coefficient α is given by

$$\alpha(I,\omega) = -\Delta n(I,\omega)\sigma(\omega) \tag{8.3}$$

$$= \frac{n_0}{1 + I/I_{\mathrm{sat}}(\omega)}\sigma(\omega), \tag{8.4}$$

where $I_{\mathrm{sat}} = \frac{\hbar\omega}{2\sigma(\omega)\tau}$ is the saturation intensity. For the stationary case, i.e. a continuous-wave light field, the population inversion reaches an equilibrium and with a maximum value $\Delta n = 0$, or equivalently $n_1 = n_2$. Accordingly, the absorption reduces to $\alpha = 0$, see Fig. 8.6. The saturation intensity is the value where $\Delta n = 0.5n_0$ and 25 % of the population is in the upper state ν_1. It depends on the upper state lifetime τ. In the present experiment, however, the inversion is not stationary as the irradiating light field is a femtosecond pulse with a duration of the order of the upper state lifetime. As a consequence, eq. 8.1 needs to be solved and Δn becomes dependent on the incident light pulse changing with time, see Fig. 8.7. This figure shows the temporal population inversion out of equilibrium excited by a light pulse at different peak intensities.

The excitation pulse has not only a time dependence but also exhibits a radial intensity profile which is assumed to be Gaussian. Hence, the intensity in the centre of the profile is much larger than at the borders. The population inversion for different intensities, shown in Fig. 8.7, apply for different radial distances r from the center of the beam at $r = 0$. The simulation in this work therefore decomposes the pulse spatially considering different rings of intensities in the beam profile. In every ring of thickness d_r, the interacting water molecules experience a different population inversion as they are irradiated with different intensities $I(r + d_r, t)$. In the simulation, the irradiated area is divided into small rings of $d_r = 1\,\mu\mathrm{m}$ and the volume up to $r = 200\,\mu\mathrm{m}$ radius is considered. In the experiment, the beam radius is 75 µm ($2w_0 = 150\,\mu\mathrm{m}$) which is why the spatial integration limits largely covers the relevant area.

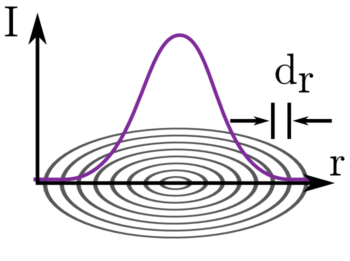

Figure 8.8: Surface irradiated by light pulse is divided into rings of thickness d_r.

The total number of water molecules per unit area n_{tot} contributing to the absorption can be calculated as

$$n_{\mathrm{tot}} = \frac{\rho_{\mathrm{H2O}}}{c_{\mathrm{mol}}} \cdot N_A \cdot d \tag{8.5}$$

where $\rho_{\mathrm{H2O}} = 997\,\mathrm{g/dm^3}$ is the density, $c_{\mathrm{mol}} = 55\,\mathrm{mol/l}$ the molecular concentration, $N_A = 6.022 \times 10^{23}\,\mathrm{mol^{-1}}$ the Avogadro constant and $d = 12 \times 10^{-4}\,\mathrm{cm}$ the sample thickness. As a side note, the number of thermally excited molecules according to the Boltzmann distribution is only 3.6 % and included in the absorption cross section σ. It therefore doesn't require further attention in the calculation.

The absorption coefficient is calculated from the time integration of the population inversion

$$\alpha_r = \frac{-\int \Delta n \cdot \sigma \cdot I(r,t)\,\mathrm{d}t}{\int I(r,t)\,\mathrm{d}t}, \tag{8.6}$$

according to eq. 8.2, considering the temporal profile of the excitation pulse. The initial condition is $\Delta n(t=0) = -n_{\mathrm{tot}}$. The cross section for water $\sigma = 6.53 \times 10^{-20}\,\mathrm{cm^2}$ is calculated from the weighted mean value from the incident pulse spectrum of the frequency dependent absorbance [155]. The time is integrated from 0 to 1.5 ps and the excitation pulse arrives after 0.5 ps. It covers the time well before the pulse arrives and extends up to complete relaxation, see Fig. 8.7. This graphs confirms the sufficient temporal integration limits for relaxation times up to 100 fs. The transmission is then calculated by

$$T = \sum_r f_r \cdot \mathrm{e}^{-\alpha_r}, \tag{8.7}$$

and weighted with the fractional contribution f_r of the surface rings, see Fig. 8.8, to the total area for all radii r. The central part of the intensity profile leads to the largest population inversion, but at the same time contributes to the overall transmission coefficient the least, as the central area is rather small compared to the boundaries. If a circle with a radius of 75 µm is split into rings of 5 µm, the central area contributes only 0.5 % compared to the outermost ring with 14.7 %.

The linear transmission coefficient without bleaching T_0 is calculated to be 8.0 % for a 12 µm thick water sample if irradiated with LWIR 200 fs pulses, as in the experiment. In the rate equation 8.1, the lifetime τ governs the slope of the transmission change. It directly relates to the level of bleaching and the change of absorption. The consequences of the lifetime dependence are visible in Fig. 8.9. It shows the transmission coefficient for different input energies assuming a 200 fs pulse with a beam waist of 150 µm. The longer the lifetime, the larger the transmission change. This can be understood intuitively as the population relaxes significantly from $v = 1$ to $v = 0$ for lifetimes shorter than the laser pulse duration and water molecules can be reexcited by the same pulse. This phenomenon is more prominent for shorter lifetimes than for those approaching the laser pulse duration. The change of absorption is shown in Tab. 8.1 in dependence of the libration excited state lifetime and the corresponding stationary saturation intensity. It shows that input intensities of the order of TW/cm^2 are necessary in order to achieve significant bleaching of the sample.

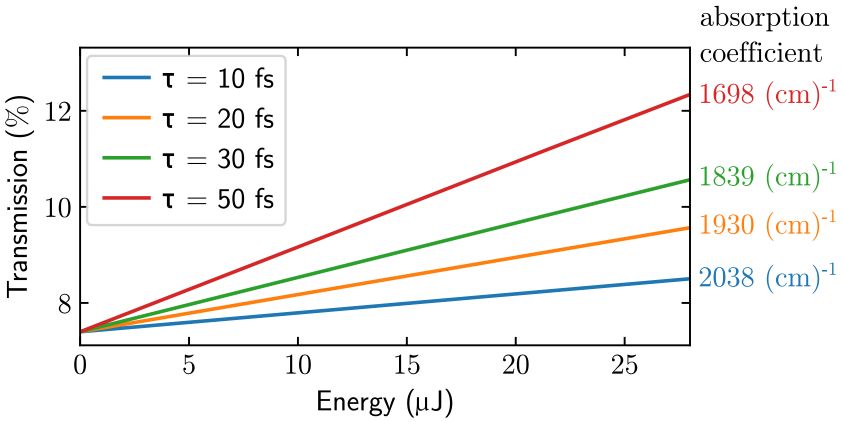

Figure 8.9: Transmission calculated from non-stationary solution of two-level quantum system for different vibrational upper state lifetime τ, calculated for 150 µm spot size, 12 µm sample thickness and 200 fs pulse duration, in dependence of input energy. Absorption coefficient α defined as $T = e^{-\alpha d}$.

τ (fs)	I_{sat} (TW/cm^2)	ΔT (%)
20	66.7	2
50	2.67	4.7
100	1.34	7.8
200	6.7	11.3

Table 8.1: Calculated transmission change for a 12 µm thick water sample, irradiated with energies between 2.1 and 27.6 µJ for a pulse ($\Delta E = 25.5$ µJ) at 11.4 µm wavelength with 200 fs duration. The calculated linear transmission coefficient is 8.0 %.

8.3 Analysis of the experimental results

Fig. 8.10 repeats the transmission data of the water sample for the LWIR pulses with energies between 2.1 and 27.6 µJ, already presented in sec. 8.1. The peak intensity amounts to 0.11 TW/cm^2 and 1.47 TW/cm^2, respectively, for a 200 fs pulse duration with a beam waist diameter of 150 µm. The measurement shows a transmission change of 1.4 %, namely from 8.3 % to 9.6 % showing a dependency of the transmission on the incident energy. The graph includes a linear fit of the experimental data yielding

$$T = 0.08 + 5.6 \times 10^{-3}\,(\mu\text{J})^{-1} E_p. \tag{8.8}$$

The literature value and the experimental transmission of 8.0 % at low energies agree within the errors.

In Fig. 8.10, the transmission change calculated from the rate equation in eq. 8.1 described in the first part of this chapter, is shown for the lifetime of 10 and 20 fs. In the limit of treating the L2 libration as a pure two-level quantum system, one thus estimates a lifetime of the upper librational level is of 10 to 20 fs. The simulation, however, makes a number of assumptions that allows this calculation to only provide a rough estimation of the lifetime. First of all, the population inversion across the sample thickness is assumed to be homogeneous.

The deposited energy in the water sample leads to local heating in the irradiated area. Though, as the energy state transition is far away from $k_B T$ at room temperature, and the number of excited molecules stemming from the Boltzmann distribution is for an estimated temperature

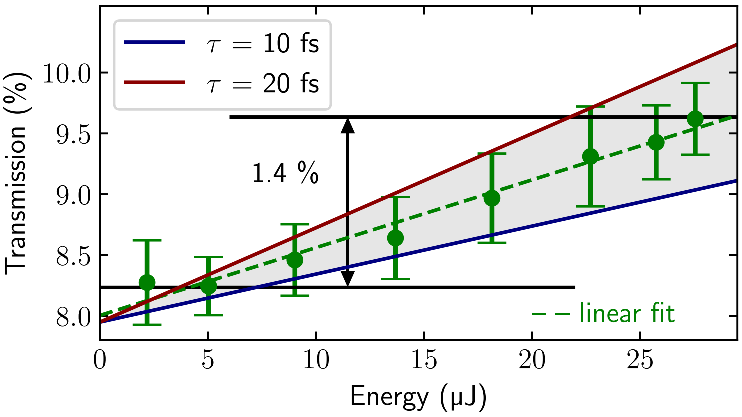

Figure 8.10: Experimental results of LWIR transmission measurement of 12 µm water sample with a transmission change of 1.4 % between 2 and 27 µJ. The graph includes a linear fit for the experimental results with $T = 0.08 + 5.6 \times 10^{-3}\,(\mu\mathrm{J})^{-1} E_p$, and the calculated transmission (solution of rate equations presented in sec. 8.2) is drawn with an y-offset of 0.55 % for a lifetime of 10 and 20 fs.

change of $\Delta T = 5\,\mathrm{K}$ [153] to a good approximation unaffected. This is true as long as the whole sample stays at the same temperature over the whole measurement time.
The distribution of energy across the hydrogen network of liquid water happens on different time scales for different mechanisms. The LWIR pulses are generated at a 1 kHz repetition rate which corresponds to a temporal separation of 1 ms between two subsequent excitations. Heat flows from the irradiated water cylinder into the surrounding water (thermal bath) and occurs on a sub-1 ms time scale [158]. For this reason, the same initial thermal conditions of the irradiated spot apply for every excitation.
Within the irradiated cylinder of water, the coupling between the different water excitation states occurs on the timescale much faster than the classical heat conduction and results from the multiple coupling mechanisms between different molecular modes. The estimated lifetime describes the timescale on which energy transfer occurs within the irradiated area, before the heat flows into the surrounding bath. S. Ashihara et. al. [153, 154] found a redshift of the fundamental transition from pump-probe experiments in the infrared due to transient heating and observed reshaping of the librational absorption. At a maximum of $1650\,\mathrm{cm}^{-1}$, they also observed an asymmetric envelope of the O-H bending absorption and a broad librational absorption background. Such effects are not included in the present 2-level model.

The estimated lifetime of the (L2) librational band of less than 20 fs is in agreement with earlier experimental estimates of a lifetime below 100 fs [154] and theoretical predictions [152]. The sensitivity of the measurement could be improved by directly exciting at the peak absorption wavelength of the band, namely at 15 µm, leading to stronger bleaching in a larger energy range and at the same time use shorter pulses. However, one oscillation cycle at 15 µm corresponds to 50 fs. In order to isolate the response of libration level relaxation from other dissipation channels, one would require a sub-cycle LWIR laser pulses with significant peak intensities which is a challenge and has not yet been developed.

9

Summary and outlook

In this thesis, novel optical parametric chirped pulse amplification (OPCPA) systems are introduced for the mid-wave infrared (MWIR) and long-wave infrared (LWIR) spectral range. A front-end based on a Cr:ZnS oscillator provides 30 fs pulses centred at 2.4 µm with a bandwidth spanning from 1.9 to 2.6 µm. Such pulses serve as the seed for the pump and the signal for an MWIR and LWIR OPCPA system. This front-end is remarkably simple and compact compared with similar systems. It only requires a dichroic mirror which splits the spectrum of the Cr:ZnS oscillator at 2.1 µm to seed the pump at 2.05 µm and the signal pulses at 2.4 µm with 42 fs pulse duration. The driver of the OPCPA is a Ho:YLF regenerative amplifier providing sufficient energy to pump multiple parametric stages. The idler pulses of both OPCPA systems have femtosecond duration and micro- to millijoule energy covering the spectral range beyond 4 µm where no solid state lasers exist.

The regenerative amplifier with the gain material Ho:YLF generates pump pulses at 2.05 µm with a record energy of 13.4 mJ. After compression to 3 ps, the peak power amounts to 5.4 GW at a repetition rate of 1 kHz which is the highest reported value for kHz regenerative amplifiers at 2 µm so far. The entire available pump energy is used to pump a 2-stage optical parametric amplifier emitting tunable idler pulses in the MWIR spectral range between 5.4 and 6.8 µm. The signal pulses at 2.4 µm for the parametric process are solitons which are Raman self-frequency shifted in a ZBLAN fibre. The soliton pulses are tunable between 2.8 and 3.2 µm depending on the coupled energy into the fibre. The nonlinear crystal $ZnGeP_2$ (ZGP) supports amplification throughout the entire tuning range leading to a total signal and idler output power of up to 1.2 mJ. By indirect phase shaping of the signal pulses using an acousto-optic programmable dispersive filter (AOPDF), idler pulses as short as 100 fs were achieved by subsequent bulk compression. This is the first MWIR OPCPA which can be flexibly tuned and offering high energy, femtosecond pulses for a wide range of applications.

The LWIR OPCPA directly uses the signal pulses at 2.4 µm of the Cr:ZnS oscillator to create idler pulses beyond 10 µm wavelength at 1 kHz repetition rate. The three optical parametric amplification (OPA) stages are based on GaSe which requires a subtle revision of design criteria as the nonlinear crystal has a comparably high group velocity mismatch for the involved pulses.

This system generates 14 µJ signal pulses at 2.4 µm with 124 fs pulse duration compressed in a Martinez prism-compressor. Simultaneously, idler pulses centred at 11.4 µm with a total energy of 70 µJ are generated. After compression in bulk material and indirect signal phase shaping with an AOPDF, a pulse duration of 185 fs was obtained leading to an unprecedented peak power of 365 GW, which is the highest reported value for LWIR pulses beyond 10 µm so far.

The idler pulse spectrum of the LWIR pulses at 11.4 µm overlaps with the absorption spectrum of the librational L2 band of liquid water providing sufficient energy for nonlinear absorption spectroscopy. A peak intensity of 1.5 TW/cm^2 enabled for the very first time to measure the nonlinear transmission change of water resulting from bleaching of directly excited librational states. A 12 µm thick water sample in a BaF$_2$ cell was irradiated with up to 27 µJ energy and the transmitted light recorded with a Pyrocam. A transmission change of 1.4 % was observed which can be attributed to the bleaching of the librational transition. Assuming that the librational states can be described by a two-level quantum system and the cross section deduced from the weighted spectrum, the estimated transmission was numerically calculated from the population inversion when excited with a 200 fs pulse. Comparing the outcome of the model with the experimental results, the lifetime of the L2 librational state of water was estimated to be shorter than 20 fs.

There is room for improvements on the performance of the LWIR OPCPA. Higher idler energy with a broader spectrum could be achieved by replacing the nonlinear crystal GaSe in the first stage by ZGP. This change is, however, restricted to low power applications as ZGP absorbs the LWIR idler and is only an option in the first stage. The ZGP crystal can be anti-reflection coated which reduces the internal Fresnel losses. As soon as BaGa$_2$Se$_7$ (BGSe) is commercially available cut to the right phase matching angle and anti-reflection coated, this new crystal is a promising alternative to ZGP in all OPA stages. In general, novel crystals providing sufficient phase matching bandwidth with a reasonable high effective nonlinearity can possibly lead to superior performance.
Alternatively, additional spectrum could be generated by shorter signal pulses in the first parametric stage. As discussed in the thesis, this comes at the expense of conversion efficiency and one additional OPA stage should compensate for the lower energy output by the use of the remaining pump energy. Still, the compressibility of the idler pulses is questionable.

In a multipass cell, the pump spectrum could be broadened due to self-phase modulation and recompressed to a shorter pulse duration in a subsequent pulse compression scheme. From the square-root law for the damage threshold [86, 159, 160], the peak intensity on the GaSe crystal could be increased to 122 GW/cm^2 for a 500 fs pulse. The higher peak intensity results in a higher gain coefficient. The shorter pulse duration also reduces the amount of signal chirp prior to amplification and only the AOPDF could introduce enough second order phase to match the signal pulse duration to the pump pulse. Less bulk material tremendously reduces the amount of third-order phases. A broader pump spectrum combined with the dual-chirp technique could lead to even shorter idler pulse durations due to a larger phase matching bandwidth, improving the temporal resolution in nonlinear spectroscopy measurements beyond 10 µm.

References

1. Maiman, T. H. Stimulated Optical Radiation in Ruby. *Nature* **187** (1960).
2. Collins, R. J., Nelson, D. F., Schawlow, A. L., Bond, W., Garrett, C. G. & Kaiser, W. Coherence, narrowing, directionality, and relaxation oscillations in the light emission from ruby. *Physical Review Letters* **5,** 303–305. doi:`10.1103/PhysRevLett.5.303` (1960).
3. Idachaba, F., Ike, D. U. & Hope, O. Future Trends in Fiber Optics Communication. *Proceedings of the World Congress on Engineering* **I,** 2–6 (2014).
4. Moreno-Barriuso, E., Lloves, J. M., Marcos, S., Navarro, R., Llorente, L. & Barbero, S. Ocular aberrations before and after myopic corneal refractive surgery: LASIK-induced changes measured with laser ray tracing. *Investigative Ophthamology & Visual Science* **42,** 1396–1403 (2001).
5. Wilson, R. H. & Tapp, H. S. Mid-infrared spectroscopy for food analysis: Recent new applications and relevant developments in sample presentation methods. *TrAC - Trends in Analytical Chemistry* **18,** 85–93. doi:`10.1016/S0165-9936(98)00107-1` (1999).
6. Ollesch, J., Drees, S. L., Heise, M. H., Behrens, T., Brüning, T. & Gerwert, K. FTIR spectroscopy of biofluids revisited: An automated approach to spectral biomarker identification. *Analyst* **138,** 4092–4102. doi:`10.1039/c3an00337j` (2013).
7. Pleitez, M., Von Lilienfeld-Toal, H. & Mäntele, W. Infrared spectroscopic analysis of human interstitial fluid in vitro and in vivo using FT-IR spectroscopy and pulsed quantum cascade lasers (QCL): Establishing a new approach to non invasive glucose measurement. *Spectrochimica Acta - Part A: Molecular and Biomolecular Spectroscopy* **85,** 61–65. doi:`10.1016/j.saa.2011.09.007` (2012).
8. Davis, K. B. *et al.* Bose-Einstein condensation in a gas of sodium atoms. *Phys. Rev. Lett.* **75,** 3969–3973. doi:`10.1103/PhysRevLett.75.3969` (1995).
9. Meyer, H. M. *et al.* Direct photonic coupling of a semiconductor quantum dot and a trapped ion. *Physical Review Letters* **114,** 1–5. doi:`10.1103/PhysRevLett.114.123001` (2015).
10. Gall, M., Wurz, N., Samland, J., Chan, C. F. & Köhl, M. Competing magnetic orders in a bilayer Hubbard model with ultracold atoms. *Nature* **589,** 40–45. doi:`10.1038/s41586-020-03058-x` (2021).
11. Schliesser, A., Picqué, N. & Hänsch, T. W. Mid-infrared frequency combs. *Nature Photonics* **6,** 440–449. doi:`10.1038/nphoton.2012.142` (2012).

12. Huse, N., Ashihara, S., Nibbering, E. T. & Elsaesser, T. Ultrafast vibrational relaxation of O-H bending and librational excitations in liquid H_2O. *Chemical Physics Letters* **404,** 389–393. doi:`10.1016/j.cplett.2005.02.007` (2005).
13. Dawlaty, J. M., Shivaraman, S., Chandrashekhar, M., Rana, F. & Spencer, M. G. Measurement of ultrafast carrier dynamics in epitaxial graphene. *Applied Physics Letters* **92,** 1–3. doi:`10.1063/1.2837539` (2008).
14. Koc, A. *et al.* High-flux table-top hard X-ray source driven by femtosecond mid-infrared pulses at a 1 kHz repetition rate. *Optics Letters* **46,** 210–213. doi:`10.1364/OL.409522` (2021).
15. Faist, J., Capasso, F., Sivco, D. L., Sirtori, C., Hutchinson, A. L. & Cho, A. Y. Quantum cascade laser. *Science* **264,** 553–556. doi:`10.1126/science.264.5158.553` (1994).
16. Patel, C. K. N. Continuous-Wave Laser Action on Vibrational-Rotational Transitions of CO_2. *Physical Review* **136.** doi:`10.1103/PhysRev.136.A1187` (1964).
17. Snakenborg, D., Klank, H. & Kutter, J. P. Microstructure fabrication with a CO_2 laser system. *Journal of Micromechanics and Microengineering* **14,** 182–189. doi:`10.1088/0960-1317/14/2/003` (2004).
18. Polyanskiy, M. N., Pogorelsky, I. V., Babzien, M., Kupfer, R., Vodopyanov, K. L. & Palmer, M. A. Post-compression of long-wave infrared 2 picosecond sub-terawatt pulses in bulk materials. *Optics Express* **29,** 31714–31725. doi:`10.1364/oe.434238` (2021).
19. Nagy, T., Simon, P. & Veisz, L. High-energy few-cycle pulses: post-compression techniques. *Advances in Physics: X* **6,** 1–41. doi:`10.1080/23746149.2020.1845795` (2020).
20. Viotti, A.-L. *et al.* Multi-pass cells for post-compression of ultrashort laser pulses. *Optica* **9,** 197–216. doi:`10.1364/optica.449225` (2022).
21. Maidment, L., Schunemann, P. G. & Reid, D. T. Molecular fingerprint-region spectroscopy from 5 to 12 µm using an orientation-patterned gallium phosphide optical parametric oscillator. *Optics Letters* **41,** 4261–4264. doi:`10.1364/ol.41.004261` (2016).
22. Cheng, S. *et al.* Compact Ho:YLF-pumped $ZnGeP_2$-based optical parametric amplifiers tunable in the molecular fingerprint regime. *Optics Letters* **45,** 2255–2258. doi:`10.1364/ol.389535` (2020).
23. Budriūnas, R., Jurkus, K., Vengris, M. & Varanavičius, A. Long seed, short pump: converting Yb-doped laser radiation to multi-µJ few-cycle pulses tunable through 2.5–15 µm. *Optics Express* **30,** 13009–13023. doi:`10.1364/oe.455180` (2022).
24. Tittel, F. K., Richter, D. & Fried, A. Mid-Infrared Laser Applications in Spectroscopy. *Solid-State Mid-Infrared Laser Sources* **516,** 458–529. doi:`10.1007/3-540-36491-9_11` (2007).
25. Malevich, P. *Generation of intense mid-IR pulses and their application for remote sensing* PhD thesis (Technische Universität Wien, 2017).

26. Lewenstein, M., Balcou, P., Ivanov, M. Y., L'Huillier, A. & Corkum, P. B. Theory of high-harmonic generation by low-frequency laser fields. *Physical Review A* **49,** 2117–2132. doi:`10.1103/PhysRevA.49.2117` (1994).

27. Popmintchev, T. *et al.* Bright coherent ultrahigh harmonics in the kev x-ray regime from mid-infrared femtosecond lasers. *Science* **336,** 1287–1291. doi:`10.1126/science.1218497` (2012).

28. Hong, K.-H. *et al.* Multi-mJ, kHz, 2.1 µm optical parametric chirped-pulse amplifier and high-flux soft x-ray high-harmonic generation. *Optics Letters* **39,** 3145. doi:`10.1364/ol.39.003145` (2014).

29. Weisshaupt, J. *et al.* High-brightness table-top hard X-ray source driven by sub-100-femtosecond mid-infrared pulses. *Nature Photonics* **8,** 927–930. doi:`10.1038/nphoton.2014.256` (2014).

30. Wolter, B. *et al.* Strong-field physics with mid-IR fields. *Physical Review X* **5,** 1–16. doi:`10.1103/PhysRevX.5.021034` (2015).

31. Strickland, D. & Mourou, G. Compression of amplified chirped optical pulses. *Optics Communications* **56,** 219–221. doi:`10.1016/0030-4018(85)90120-8` (1985).

32. Piskarskas, A., Stabinis, A. & Yankauskas, A. Phase phenomena in parametric amplifiers and generators of ultrashort light pulses. *Soviet Physics Uspekhi* **29,** 869–879. doi:`10.1070/PU1986v029n09ABEH003501` (1986).

33. Dubietis, A., Jonušauskas, G. & Piskarskas, A. Powerful femtosecond pulse generation by chirped and stretched pulse parametric amplification in BBO crystal. *Optics Communications* **88,** 437–440. doi:`10.1016/0030-4018(92)90070-8` (1992).

34. Fattahi, H. *et al.* Third-generation femtosecond technology. *Optica* **1,** 45–63. doi:`10.1364/OPTICA.1.000045` (2014).

35. Cerullo, G. & De Silvestri, S. Ultrafast optical parametric amplifiers. *Review of Scientific Instruments* **74,** 1–18. doi:`10.1063/1.1523642` (2003).

36. Baudisch, M., Wolter, B., Pullen, M., Hemmer, M. & Biegert, J. High power multi-color OPCPA source with simultaneous femtosecond deep-UV to mid-IR outputs. *Optics Letters* **41,** 3583–3586. doi:`10.1364/ol.41.003583` (2016).

37. Petrov, V. Frequency down-conversion of solid-state laser sources to the mid-infrared spectral range using non-oxide nonlinear crystals. *Progress in Quantum Electronics* **42,** 1–106. doi:`10.1016/j.pquantelec.2015.04.001` (2015).

38. Guardalben, M. *et al.* Design of a highly stable, high-conversion-efficiency, optical parametric chirped-pulse amplification system with good beam quality. *Optics Express* **11,** 2511–2524. doi:`10.1364/oe.11.002511` (2003).

39. Dubietis, A. & Matijošius, A. Table-top optical parametric chirped pulse amplifiers: past and present. *Opto-Electron Advances* **6,** 2200460. doi:`10.29026/oea.2023.220046` (2023).

40. Elu, U. *et al.* Table-top high-energy 7 µm OPCPA and 260 mJ Ho:YLF pump laser. *Optics Letters* **44,** 3194–3197. doi:`10.1364/OL.44.003194` (2019).

41. Von Grafenstein, L. *et al.* 5 µm few-cycle pulses with multi-gigawatt peak power at a 1 kHz repetition rate. *Optics Letters* **42,** 3796–3799. doi:`10.1364/ol.42.003796` (2017).

42. Andriukaitis, G. *et al.* 90 GW peak power few-cycle mid-infrared pulses from an optical parametric amplifier. *Optics Letters* **36,** 2755–2757. doi:`10.1364/ol.36.002755` (2011).

43. Von Grafenstein, L. *et al.* Multi-millijoule, few-cycle 5 µm OPCPA at 1 kHz repetition rate. *Optics Letters* **45,** 5998–6001. doi:`10.1364/OL.402562` (2020).

44. Sanchez, D. *et al.* 7 µm, ultrafast, sub-millijoule-level mid-infrared optical parametric chirped pulse amplifier pumped at 2 µm. *Optica* **3,** 147–150. doi:`10.1364/optica.3.000147` (2016).

45. Qu, S. *et al.* 9 µm few-cycle optical parametric chirped-pulse amplifier based on $LiGaS_2$. *Optics Letters* **44,** 2422–2425. doi:`10.1364/ol.44.002422` (2019).

46. Namboodiri, M. *et al.* High power 9 µm source for spectroscopy and HHG. *Proc. SPIE* **11670,** 1–6. doi:`10.1117/12.2576133` (2021).

47. Rotermund, F., Petrov, V. & Noack, F. Difference-frequency generation of intense femtosecond pulses in the mid-IR (4-12 µm) using $HgGa_2S_4$ and $AgGaS_2$. *Optics Communications* **185,** 177–183. doi:`10.1016/S0030-4018(00)00987-1` (2000).

48. Kaindl, R. A., Wurm, M., Reimann, K., Hamm, P., Weiner, A. M. & Woerner, M. Generation, shaping, and characterization of intense femtosecond pulses tunable from 3 to 20 µm. *Journal of the Optical Society of America B* **17,** 2086–2094. doi:`10.1364/josab.17.002086` (2000).

49. Junginger, F. *et al.* Single-cycle multiterahertz transients with peak fields above 10 MV/cm. *Optics Letters* **35,** 2645–2647. doi:`10.1364/ol.35.002645` (2010).

50. Liu, K. *et al.* Multimicrojoule GaSe-based mid-infrared optical parametric amplifier with an ultrabroad idler spectrum covering 4.2–16 µm. *Optics Letters* **44,** 1003–1006. doi:`10.1364/ol.44.001003` (2019).

51. Duda, M. *et al.* 10-µJ few-cycle 12-µm source based on difference-frequency generation driven by a 1-kHz mid-wave infrared OPCPA. *Optics Letters* **47,** 2891–2894. doi:`10.1364/ol.456971` (2022).

52. Sorokina, I. T., Dvoyrin, V. V., Tolstik, N. & Sorokin, E. Mid-IR Ultrashort Pulsed Fiber-Based Lasers. *IEEE Journal of Selected Topics in Quantum Electronics* **20,** 0903412. doi:`10.1109/JSTQE.2014.2310655` (2014).

53. Sorokina, I. T. & Sorokin, E. Femtosecond Cr^{2+}-Based Lasers. *IEEE Journal of Selected Topics in Quantum Electronics* **21,** 16015190. doi:`10.1109/JSTQE.2014.2341589` (2015).

54. Nagl, N., Gröbmeyer, S., Pervak, V., Krausz, F., Pronin, O. & Mak, K. F. Directly diode-pumped, Kerr-lens mode-locked, few-cycle Cr:ZnSe oscillator. *Optics Express* **27,** 24445–24454. doi:`10.1364/oe.27.024445` (2019).

55. Steinleitner, P. *et al.* Single-cycle infrared waveform control. *Nature Photonics* **16,** 512–518. doi:`10.1038/s41566-022-01001-2` (2022).

56. Mirov, S. B., Fedorov, V. V., Martyshkin, D., Moskalev, I. S., Mirov, M. & Vasilyev, S. Progress in mid-IR lasers based on Cr and Fe-doped II-VI chalcogenides. *IEEE Journal of Selected Topics in Quantum Electronics* **21,** 292–310. doi:`10.1109/JSTQE.2014.2346512` (2015).

57. Mirov, S. B. *et al.* Frontiers of Mid-IR lasers based on transition metal doped chalcogenides. *IEEE Journal of Selected Topics in Quantum Electronics* **24,** 1601829. doi:`10.1109/JSTQE.2018.2808284` (2018).

58. Nagl, N. *A new generation of ultrafast oscillators for mid-infrared applications* (Jan. 2021).

59. Maxwell, J. C. A dynamical theory of the electromagnetic field. *Philosophical Transactions of the Royal Society of London* **155,** 459–512. doi:`10.1098/rstl.1865.0008` (1865).

60. Saleh, B. & Teich, M. C. *Fundamental of Photonics* (John Wiley and Sons, Ltd, 2019).

61. Diels, J.-C. & Rudolph, W. *Ultrashort laser pulse phenomena: fundamentals, techniques and applications on a femtosecond time scale* 1st ed. (Academic Press, San Diego, 1996).

62. Weiner, A. M. *Ultrafast Optics* 1–580. ISBN: 9780471415398. doi:`10.1002/9780470473467` (Wiley, 2009).

63. Agrawal, G. P. *Nonlinear fiber optics* 3rd ed., 1–728. doi:`10.1016/C2018-0-01168-8` (Academic Press, San Diego, 2001).

64. Mero, M. & Petrov, V. Compensated Mid-Infrared Pulses From a Noncollinear Optical Parametric Amplifier Dispersion Compensated Mid-Infrared Pulses From a Noncollinear Optical Parametric Amplifier. *IEEE Photonics Journal* **9.** doi:`10.1109/JPHOT.2017.2697498` (2017).

65. Smith, A. V. *Crystal nonlinear optics: with SNLO examples* 766. ISBN: 9780692056783 (AS-Photonics, 2015).

66. Armstrong, J. A., Bloembergen, N., Ducuing, J. & Pershan, P. S. Interactions between light waves in a nonlinear dielectric. *Physical Review* **127,** 1918–1939. doi:`10.1103/PhysRev.127.1918` (1962).

67. Ross, I. N., Matousek, P., New, G. H. C. & Osvay, K. Analysis and optimization of optical parametric chirped pulse amplification. *Journal of the Optical Society of America B* **19,** 2945–2956. doi:`10.1364/josab.19.002945` (2002).

68. New, G. *Introduction to nonlinear optics* 1–257. doi:`10.1017/CBO9780511975851` (Cambridge University Press, 2011).

69. Siegmann, A. E. *Lasers* ISBN: 0198557132 (University Science Books, 1986).

70. Boyd, R. W. Nonlinear Optics. *Nonlinear Optics,* 1–609. doi:`10.1016/C2015-0-05510-1` (2020).

71. Waxer, L. J., Bagnoud, V., Begishev, I. A., Guardalben, M. J., Puth, J. & Zuegel, J. D. High-conversion-efficiency optical parametric chirped-pulse amplification system using spatiotemporally shaped pump pulses. *Optics Letters* **28,** 1245–1247. doi:`10.1364/ol.28.001245` (2003).

72. Bagnoud, V., Begishev, I. A., Guardalben, M. J., Puth, J. & Zuegel, J. D. 5 Hz, >250 mJ optical parametric chirped-pulse amplifier at 1053 nm. *Optics Letters* **30,** 1843–1845. doi:`10.1364/OL.30.0018430` (2005).

73. Flemens, N. *et al.* High quantum efficiency parametric amplification via hybridized nonlinear optics. arXiv: `2207.04147` (2022).

74. Manley, J. M. & Rowe, H. E. Some general properties of nonlinear elements-part I. general energy relations. *Proceedings of the IRE* **44,** 904–913. doi:`10.1109/JRPROC.1956.275145` (1956).

75. Manzoni, C. & Cerullo, G. Design criteria for ultrafast optical parametric amplifiers. *Journal of Optics* **18,** 1–33. doi:`10.1088/2040-8978/18/10/103501` (2016).

76. Jansonas, G., Budriūnas, R., Vengris, M. & Varanavičius, A. Interferometric measurements of nonlinear refractive index in the infrared spectral range. *Optics Express* **30,** 30507–30524. doi:`10.1364/oe.458850` (2022).

77. Yan, X., Liao, M., Suzuki, T. & Ohishi, Y. Analysis of soliton self-frequency shift in ZBLAN fiber as a broadband supercontinuum medium. *Optical Components and Materials X* **8621,** 862112. doi:`10.1117/12.2003249` (2013).

78. Pigeon, J. J., Tochitsky, S. Y., Welch, E. C. & Joshi, C. Measurements of the nonlinear refractive index of noble gases and major air constituents at 10 µm using four-wave mixing. *Optics Letters* **41,** 3924–3927. doi:`10.1364/OL.41.003924` (2017).

79. Schimpf, D. N., Eidam, T., Seise, E., Hädrich, S., Limpert, J. & Tünnermann, A. Circular versus linear polarization in laser-amplifiers with Kerr-nonlinearity. *Optics Express* **17,** 18774–18781. doi:`10.1364/oe.17.018774` (2009).

80. Von Grafenstein, L. *Generation of intense few-cycle pulses in the mid-wave infrared* PhD thesis (Humboldt Universität zu Berlin, 2018).

81. Arisholm, G. & Fonnum, H. *Simulation System For Optical Science (SISYFOS) – tutorial, version 2* 2021.

82. Petrov, V. Parametric down-conversion devices: The coverage of the mid-infrared spectral range by solid-state laser sources. *Optical Materials* **34,** 536–554. doi:`10.1016/j.optmat.2011.03.042` (2012).

83. Hemmer, M., Thai, A., Baudisch, M., Ishizuki, H., Taira, T. & Biegert, J. 18-µJ energy, 160-kHz repetition rate, 250-MW peak power mid-IR OPCPA. *Chinese Optics Letters* **11,** 013202. doi:`10.3788/col201311.013202` (2013).

84. Mayer, B. W., Phillips, C. R., Gallmann, L. & Keller, U. Mid-infrared pulse generation via achromatic quasi-phase-matched OPCPA. *Optics Express* **22,** 20798. doi:`10.1364/oe.22.020798` (2014).

85. Petrov, V. *et al.* Barium nonlinear optical crystals for the mid-IR: Characterization and applications. *Journal of the Optical Society of America B* **38,** 46–58. doi:`10.1364/mics.2020.mtu1c.6` (2021).

86. Griebner, U., von Grafenstein, L., Bock, M. & Elsaesser, T. Generation of few-cycle millijoule pulses at 5 µm employing a $ZnGeP_2$-based OPCPA pumped with GW peak power pulses at 2 µm. *Proc. of SPIE* **10713,** 1–4. doi:`10.1117/12.2319811` (2018).

87. Rotermund, F., Petrov, V. & Noack, F. Femtosecond noncollinear parametric amplification in the mid-infrared. *Optics Communications* **169,** 183–188. doi:`10.1016/S0030-4018(99)00397-1` (1999).

88. Trapani, P. D. *et al.* Matching of group velocities in three-wave parametric interaction with femtosecond pulses and application to traveling-wave generators. *Journal of the Optical Society of America B* **12,** 2237–2244. doi:`10.1364/josab.12.002237` (1995).

89. Martinez, O. E., Gordon, J. P. & Fork, R. L. Negative group-velocity dispersion using refraction. *Journal of the Optical Society of America A* **1,** 1003–1006. doi:`10.1364/JOSAA.1.001003` (1984).

90. Fork, R. L., Martinez, O. E. & Gordon, J. P. Negative dispersion using pairs of prisms. *Optics Letters* **9,** 150–152. doi:`10.1364/ol.9.000150` (1984).

91. Kane, S. & Squier, J. Grism-pair stretcher–compressor system for simultaneous second- and third-order dispersion compensation in chirped-pulse amplification. *Journal of the Optical Society of America B* **14,** 661–665. doi:`10.1364/josab.14.000661` (1997).

92. Martinez, O. E. 3000 times grating compressor with positive group velocity dispersion: Application to fiber compensation in 1.3-1.6 µm region. *IEEE Journal of Quantum Electronics* **23,** 59–64. doi:`10.1109/JQE.1987.1073201` (1987).

93. Keller, U. *Ultrafast Lasers: A Comprehensive Introduction to Fundamental Principles with Practical Applications* 1st ed., 1–810. ISBN: 9783319610870 (Springer Nature Switzerland AG, 2021).

94. Zou, X. *et al.* Flat-Top Pumped Multi-Millijoule Mid-Infrared Parametric Chirped-Pulse Amplifier at 10 kHz Repetition Rate. *Laser and Photonics Reviews* **15,** 2000292. doi:`10.1002/lpor.202000292` (2021).

95. Fattahi, H. in *High Energy and Short Pulse Lasers* chap. 3 (2016). doi:`10.5772/64438`.

96. Abdullaev, G. B., Kulevskii, L. A., Prokhorov, A. M., Savel'ev, A. D., Salaev, E. Y. & Smirnov, V. V. GaSe, A New Effective Material for Nonlinear Optics. *JETP Letters* **16,** 90–92 (1972).

97. Hemmer, M. *et al.* 2-µm wavelength, high-energy Ho:YLF chirped-pulse amplifier for mid-infrared OPCPA. *Optics Letters* **40,** 451–454. doi:`10.1364/ol.40.000451` (2015).

98. Kroetz, P. *et al.* Overcoming bifurcation instability in high-repetition-rate Ho:YLF regenerative amplifiers. *Optics Letters* **40,** 5427–5430. doi:`10.1364/ol.40.005427` (2015).

99. Von Grafenstein, L., Bock, M., Griebner, U. & Elsaesser, T. High-energy multi-kilohertz Ho-doped regenerative amplifiers around 2 µm. *Optics Express* **23,** 14744–14752. doi:`10.1364/oe.23.014744` (2015).

100. Aggarwal, R. L., Ripin, D. J., Ochoa, J. R. & Fan, T. Y. Measurement of thermo-optic properties of $Y_3Al_5O_12$, $Lu_3Al_5O_{12}$, YAI_3, $LiYF_4$, $LiLuF_4$, BaY_2F_8, $KGd(WO_4)_2$, and $KY(WO_4)_2$ laser crystals in the 80-300 K temperature range. *Journal of Applied Physics* **98,** 1–14. doi:`10.1063/1.2128696` (2005).

101. Dergachev, A. High-energy, kHz-rate, picosecond, 2-µm laser pump source for mid-IR nonlinear optical devices. *Solid State Lasers XXII: Technology and Devices* **8599,** 1–14. doi:`10.1117/12.2001386` (2013).

102. Malevich, P. *et al.* High energy and average power femtosecond laser for pumping mid-IR OPAs. *Conference on Lasers and Electro-Optics, CLEO 2013* **38,** 2746–2749. doi:`10.1364/cleo_si.2013.cth3h.5` (2013).

103. Von Grafenstein, L., Bock, M., Ueberschaer, D., Griebner, U. & Elsaesser, T. Ho:YLF chirped pulse amplification at kilohertz repetition rates – 4.3 ps pulses at 2 µm with GW peak power. *Optics Letters* **41,** 4668–4671. doi:`10.1364/ol.41.004668` (2016).

104. Von Grafenstein, L., Bock, M. & Griebner, U. Bifurcation analysis in high repetition rate regenerative amplifiers. *IEEE Journal of Selected Topics in Quantum Electronics* **24,** 3000213. doi:`10.1109/JSTQE.2018.2818462` (2018).

105. Kroetz, P. *et al.* Numerical study of spectral shaping in high energy Ho:YLF amplifiers. *Optics Express* **24,** 9905–9921. doi:`10.1364/oe.24.009905` (2016).

106. Kroetz, P. *et al.* Study on laser characteristics of Ho:YLF regenerative ampliers: Operation regimes, gain dynamics, and highly stable operation points. *Applied Physics B: Lasers and Optics* **123,** 1–17. doi:`10.1007/s00340-017-6704-0` (2017).

107. Frantz, L. M. & Nodvik, J. S. Theory of pulse propagation in a laser amplifier. *Journal of Applied Physics* **34,** 2346–2349. doi:`10.1063/1.1702744` (1963).

108. Murari, K. *et al.* Intracavity gain shaping in millijoule-level, high gain Ho:YLF regenerative amplifiers. *Optics Letters* **41,** 1114–1117. doi:`10.1364/ol.41.001114` (2016).

109. Treacy, E. B. Optical pulse compression with diffraction gratings. *IEEE Journal of Quantum Electronics* **5,** 454–458. doi:`10.1109/JQE.1969.1076303` (1969).

110. Fu, Y., Midorikawa, K. & Takahashi, E. J. Dual-chirped optical parametric amplification: A method for generating super-intense mid-infrared few-cycle pulses. *IEEE Journal of Selected Topics in Quantum Electronics* **25.** doi:`10.1109/JSTQE.2019.2925720` (2019).

111. Manassah, J. T., Alfano, R. R. & Mustafa, M. Spectral distribution of an ultrafast supercontinuum laser source. *Physics Letters* **107A,** 305–309. doi:`10.1016/0375-9601(85)90641-3` (1985).

112. Dudley, J. M., Genty, G. & Coen, S. Supercontinuum generation in photonic crystal fiber. *Reviews of Modern Physics* **78,** 1135–1184. doi:`10.1103/RevModPhys.78.1135` (2006).

113. Corkum, P. B., Rolland, C. & Srinivasan-Rao, T. Supercontinuum generation in gases. *Physical Review Letters* **57,** 2268–2271. doi:`10.1103/PhysRevLett.57.2268` (1986).

114. Ell, R. *et al.* Generation of 5-fs pulses and octave-spanning spectra directly from a Ti:sapphire laser. *Optics Letters* **26,** 373–376. doi:`10.1364/ol.26.000373` (2001).

115. Xu, L. *et al.* High-power sub-10-fs Ti:sapphire oscillators. *Applied Physics B: Lasers and Optics* **65,** 151–159. doi:`10.1007/s003400050260` (1997).

116. Mirov, S. B., Fedorov, V. V., Moskalev, I. S. & Martyshkin, D. V. Recent progress in transition-metal-doped II-VI Mid-IR lasers. *IEEE Journal on Selected Topics in Quantum Electronics* **13,** 810–821. doi:`10.1109/JSTQE.2007.896634` (2007).

117. Nagl, N. *A new generation of ultrafast oscillators for mid-infrared applications* 1–160. ISBN: 9783030897536 (Springer International Publishing, 2021).

118. Sorokina, I. T., Sorokin, E. & Carrig, T. J. Femtosecond pulse generation from a SESAM mode-locked Cr:ZnSe laser. *Conference on Lasers and Electro-Optics/Quantum Electronics and Laser Science Conference and Photonic Applications Systems Technologies* (2006).

119. Tolstik, N., Sorokin, E. & Sorokina, I. T. Kerr-lens mode-locked Cr:ZnS laser. *Optics Letters* **38,** 299–301 (2012).

120. Vasilyev, S., Moskalev, I., Mirov, M., Mirov, S. & Gapontsev, V. Three optical cycle mid-IR Kerr-lens mode-locked polycrystalline Cr^{2+}:ZnS laser. *Optics Letters* **40,** 5054–5057. doi:`10.1364/ol.40.005054` (2015).

121. Vasilyev, S., Moskalev, I., Mirov, M., Mirov, S. & Gapontsev, V. Multi-Watt mid-IR femtosecond polycrystalline Cr^{2+}:ZnS and Cr^{2+}:ZnSe laser amplifiers with the spectrum spanning 2.0–2.6 µm. *Optics Express* **24,** 1616–1623. doi:`10.1364/oe.24.001616` (2016).

122. Moskalev, I. *et al.* 140 W Cr:ZnSe laser system. *Optics Express* **24,** 21090–21104. doi:`10.1364/oe.24.021090` (2016).

123. Wang, Y., Fernandez, T. T., Coluccelli, N., Gambetta, A., Laporta, P. & Galzerano, G. 47-fs Kerr-lens mode-locked Cr:ZnSe laser with high spectral purity. *Optics Express* **25,** 25193–25200. doi:`10.1364/oe.25.025193` (2017).

124. Barh, A. *et al.* Watt-level and sub-100-fs self-starting mode-locked 2.4 µm Cr:ZnS oscillator enabled by GaSb-SESAMs. *Optics Express* **29,** 5934–5946. doi:`10.1364/oe.416894` (2021).

125. Wang, Q. *et al.* Broadband mid-infrared coverage (2–17 µm) with few-cycle pulses via cascaded parametric processes. *Optics Letters* **44,** 2566–2569. doi:`10.1364/ol.44.002566` (2019).

126. Fürtjes, P., Bock, M., von Grafenstein, L., Ueberschaer, D., Griebner, U. & Elsaesser, T. Few-cycle 65-µJ pulses at 11.4 µm for ultrafast nonlinear longwave-infrared spectroscopy. *Optica* **9,** 1303–1306. doi:`10.1364/optica.472650` (2022).

127. Nagl, N., Mak, K. F., Wang, Q., Pervak, V., Krausz, F. & Pronin, O. Efficient femtosecond mid-infrared generation based on a Cr:ZnS oscillator and step-index fluoride fibers. *Optics Letters* **44,** 2390–2393. doi:`10.1364/ol.44.002390` (2019).

128. Fuertjes, P., von Grafenstein, L., Ueberschaer, D., Mei, C., Griebner, U. & Elsaesser, T. Compact OPCPA system seeded by a Cr:ZnS laser for generating tunable femtosecond pulses in the MWIR. *Optics Letters* **46,** 1704–1707. doi:`10.1364/ol.419956` (2021).

129. Fuertjes, P., von Grafenstein, L., Mei, C., Bock, M., Griebner, U. & Elsaesser, T. Cr:ZnS-based soliton self-frequency shifted signal generation for a tunable sub-100 fs MWIR OPCPA. *Optics Express* **30,** 5142–5150. doi:`10.1364/oe.450210` (2022).

130. Snyder, A. W. & Love, J. D. *Optical waveguide theory* 1st ed. (Springer New York, NY, 1983).

131. Gordon, J. P. Theory of the soliton self-frequency shift. *Optics Letters* **11,** 662–664. doi:`10.1364/ol.11.000662` (1986).

132. Mitschke, F. M. & Mollenauer, L. F. Discovery of the soliton self-frequency shift. *Optics Letters* **11,** 659–661. doi:`10.1364/ol.11.000659` (1986).

133. Santhanam, J. & Agrawal, G. P. Raman-induced spectral shifts in optical fibers: General theory based on the moment method. *Optics Communications* **222,** 413–420. doi:`10.1016/S0030-4018(03)01561-X` (2003).

134. Fluoré, L. V. *Fluoride Fibers: General Properties* Accessed: 30.09.2022. 2022.

135. Tauser, F., Adler, F. & Leitenstorfer, A. Widely tunable sub-30-fs pulses from a compact erbium-doped fiber source. *Optics Letters* **29,** 516–518. doi:`10.1364/ol.29.000516` (2004).

136. Schreiber, T. *Fiberdesk - Nonlinear Pulse Propagation* Accessed: 10.10.2022. 2020–2022.

137. Yan, X., Liao, M., Suzuki, T. & Ohishi, Y. Analysis of soliton self-frequency shift in ZBLAN fiber as a broadband supercontinuum medium. *Optical Components and Materials X* **8621,** 1–7. doi:`10.1117/12.2003249` (2013).

138. Chen, Z., Taylor, A. J. & Efimov, A. Soliton dynamics in non-uniform fiber tapers: analytical description through an improved moment method. *Journal of the Optical Society of America B* **27,** 1022–1030. doi:`10.1364/josab.27.001022` (2010).

139. Von Grafenstein, L., Bock, M., Ueberschaer, D., Koç, A., Griebner, U. & Elsaesser, T. 2.05 µm chirped pulse amplification system at a 1 kHz repetition rate—2.4 ps pulses with 17 GW peak power. *Optics Letters* **45,** 3836–3839. doi:`10.1364/ol.395496` (2020).

140. Monmayrant, A., Weber, S. & Chatel, B. A newcomer's guide to ultrashort pulse shaping and characterization. *Journal of Physics B: Atomic, Molecular and Optical Physics* **43,** 1–34. doi:`10.1088/0953-4075/43/10/103001` (2010).

141. Yin, Y. *et al.* Towards terawatt sub-cycle long-wave infrared pulses via chirped optical parametric amplification and indirect pulse shaping. *Scientific Reports* **7,** 1–10. doi:`10.1038/srep45794` (2017).

142. Liu, K. *et al.* Microjoule Sub-Two-Cycle Mid-Infrared Intrapulse-DFG Driven by 3-µm OPCPA. *IEEE Photonics Technology Letters* **31,** 1741–1744 (2019).

143. Verluise, F., Laude, V., Cheng, Z., Spielmann, C. & Tournois, P. Amplitude and phase control of ultrashort pulses by use of an acousto-optic programmable dispersive filter: pulse compression and shaping. *Optics Letters* **25,** 575–577. doi:`10.1364/OL.25.000575` (2000).

144. Maksimenka, R. *et al.* Direct mid-infrared femtosecond pulse shaping with a calomel acousto-optic programmable dispersive filter. *Optics Letters* **35,** 3565–3567. doi:`10.1364/ol.35.003565` (2010).

145. Maksimenka, R. & Tournois, P. Mid-infrared high-frequency high-resolution reflective acousto-optic filters in mercury halides. *Optics Communications* **285,** 715–719. doi:`10.1016/j.optcom.2011.10.078` (2012).

146. Jahjah, M. *et al.* Atmospheric CH_4 and N_2O measurements near Greater Houston area landfills using a QCL-based QEPAS sensor system during DISCOVER-AQ 2013. *Optics Letters* **39,** 957–960. doi:`10.1364/ol.39.000957` (2014).

147. Polyanskiy, M. N., Pogorelsky, I. V., Babzien, M., Kupfer, R., Vafaei-Najafabadi, N. & Palmer, M. A. High-peak-power long-wave infrared lasers with CO_2 amplifiers. *Photonics* **8,** 2–13. doi:`10.3390/photonics8040101` (2021).

148. Voronin, A. A., Lanin, A. A. & Zheltikov, A. Modeling high-peak-power few-cycle field waveform generation by optical parametric amplification in the long-wavelength infrared. *Optics Express* **24,** 23206–23220. doi:`10.1364/oe.24.023207` (2016).

149. Kato, K., Tanno, F. & Umemura, N. Sellmeier and thermo-optic dispersion formulas for GaSe. *Applied Optics* **52,** 2325–2328. doi:`10.1364/AO.52.002325` (2013).

150. Allakhverdiev, K. R. *et al.* Corrected infrared Sellmeier coefficients for gallium selenide. *Journal of Applied Physics* **98,** 093515. doi:`10.1063/1.2128694` (2005).

151. Bakker, H. J. & Skinner, J. L. Vibrational spectroscopy as a probe of structure and dynamics in liquid water. *Chemical Reviews* **110,** 1498–1517. doi:`10.1021/cr9001879` (2010).

152. Petersen, J., Møller, K. B., Rey, R. & Hynes, J. T. Ultrafast librational relaxation of H_2O in liquid water. *Journal of Physical Chemistry B* **117,** 4541–4552. doi:`10.1021/jp308648u` (2013).

153. Ashihara, S., Huse, N., Espagne, A., Nibbering, E. T. & Elsaesser, T. Vibrational couplings and ultrafast relaxation of the O-H bending mode in liquid H_2O. *Chemical Physics Letters* **424,** 66–70. doi:`10.1016/j.cplett.2006.04.051` (2006).

154. Ashihara, S., Huse, N., Espagne, A., Nibbering, E. T. & Elsaesser, T. Ultrafast structural dynamics of water induced by dissipation of vibrational energy. *Journal of Physical Chemistry A* **111,** 743–746. doi:`10.1021/jp0676538` (2007).

155. Zelsmann, H. R. Temperature dependence of the optical constants for liquid H_2O and D_2O in the far IR region. *Journal of Molecular Structure* **350,** 95–114. doi:`10.1016/0022-2860(94)08471-S` (1995).

156. Polyanskiy, M. N., Babzien, M., Pogorelsky, I. V., Kupfer, R., Vodopyanov, K. L. & Palmer, M. A. Single-shot measurement of the nonlinear refractive index of air at 9.2 µm with a picosecond terawatt CO_2 laser. *Optics Letters* **46,** 2067–2070. doi:`10.1364/ol.423800` (2021).

157. Wünsche, H.-J. *Vorlesungsskript Optik / Photonik II - Nichtlineare Optik und Laserphysik* tech. rep. (Humbold-Universität zu Berlin, 2005).

158. Møller, K. B., Rey, R. & Hynes, J. T. Hydrogen bond dynamics in water and ultrafast infrared spectroscopy: A theoretical study. *Journal of Physical Chemistry A* **108,** 1275–1289. doi:`10.1021/jp035935r` (2004).

159. Stuart, B. C., Feit, M. D., Rubenchik, A. M., Shore, B. W. & Perry, M. D. Laser-induced damage in dielectrics with nanosecond to subpicosecond pulses. *Physical Review Letters* **74,** 2248–2251. doi:`10.1103/PhysRevLett.74.2248` (1995).

160. Mero, M., Liu, J., Rudolph, W., Ristau, D. & Starke, K. Scaling laws of femtosecond laser pulse induced breakdown in oxide films. *Physical Review B* **71,** 1–7. doi:`10.1103/PhysRevB.71.115109` (2005).

A

Glossary

ACF	Autocorrelation function
AOPDF	Acousto-optic programmable dispersive filter
AR	Anti-reflection (coating)
CEP	Carrier envelope phase
CPA	Chirped pulse amplification
CVBG	Chirped volume Bragg grating
DFG	Difference frequency generation
DM	Dichroic mirror
EUV	extreme ultraviolet (spectral region)
FM	Figure of merit
FROG	Frequency resolved optical gating
FTL	Fourier transform limit
FWHM	Full width half maximum
GDD	Group delay dispersion
GVD	Group velocity dispersion
GVM	Group velocity mismatch
HHG	High harmonic generation
HR	High reflection (coating)
IR	Infrared
IRS	Intrapulse Raman shift
LIDT	Light induced damage threshold
LWIR	Long-wave infrared (spectral region, 8 - 15 µm)
MWIR	Mid-wave infrared (spectral region, 3 - 8 µm)
NIR	Near-infrared (spectral region, 1.5 - 3 µm)
NLSE	Nonlinear Schrödinger equation
OPA	Optical parametric amplifier
OPG	Optical parametric generation

OPCPA	Optical parametric chirped pulse amplification
OPO	Optical paramteric oscillator
OR	Optical rectification
PC	Pockels cell
PM	Phase matching
QCL	Quantum cascade laser
RA	Regenerative amplifier
RH	Relative humidity
RMS	Root-mean-square
SC	Supercontinuum
SFG	Sum-frequency generation
SFSS	Self-frequency shifted soliton (Raman)
SHG	Second harmonic generation
Sisyfos	Simulation system for optical science
SLM	Spatial light modulator
SPM	Self-phase modulation
SSL	Solid state laser
SVEA	Slowly varying envelope approximation
SWIR	Short-wave infrared (spectral region, 1.5 - 3 µm)
TFP	Thin-film polariser
TOD	Third-order dispersion
TPA	Two-photon absorption
UV	Ultraviolet (spectral region, 150 - 380 nm)
VIS	Visible (spectral region, 380 - 780 nm
ZBLAN	ZrF_4 BaF_2 LaF_3 AlF_3 NaF fluoride fibre
ZDW	Zero-dispersion wavelength

Crystals and Materials

AGS	silver gallium sulfide ($AgGaS_2$)
AGSe	silver gallium selenide ($AgGaSe_2$)
BBO	beta barium borate (BaB_2O_4)
BiBO	bismuth borate (BiB_3O_6)
BGS	barium gallium sulfide ($BaGa_4S_7$)
BGSe	barium gallium selenide ($BaGa_4Se_7$)
BGGS	barium gallium germanium sulfide ($BaGa_2GeS_6$)
BGGSe	barium gallium germanium selenide ($BaGa_2GeSe_6$)
CSP	cadmium silicon phosphide ($CdSiP_2$)
GaSe	gallium selenide
KTA	potassium titanyle arsenate ($KTiOAsO_4$)
LBO	lithium triborate (LiB_3O_5)
LGS	lithium gallium sulfide ($LiGaS_2$)
LN	lithium niobate ($LiNbO_3$)
PPSLT	periodically poled stoichiometric lithium tantalate ($LiTaO_3$)
RTP	rubidium titanyl phosphate ($RbTiOPO_4$)
Sapphire	silver oxide (Al_2O_3)
Ti:Sa	titanium sapphire
YLF	yttrium lithium fluoride ($LiYF_4$)
YAG	yttrium aluminium garnet ($Y_3Al_5O_{12}$)
YCOB	yttrium calcium oxoborate ($YCa_4O(BO_3)_3$)
ZGP	zinc germanium phosphide ($ZnGeP_2$)
ZnSe	zinc selenide
ZnS	zinc sulfide

B

Publications

Publications in peer reviewed journals

- P. Fuertjes, L. von Grafenstein, D. Ueberschaer, C. Mei, U. Griebner, and T. Elsaesser, "Compact OPCPA system seeded by a Cr:ZnS laser for generating tunable femtosecond pulses in the MWIR", Opt. Lett. **46**, 1704 (2021).
- P. Fuertjes, L. von Grafenstein, C. Mei, M. Bock, U. Griebner, and T. Elsaesser,"Cr:ZnS-based soliton self-frequency shifted signal generation for a tunable sub-100 fs MWIR OPCPA", Opt. Express **30**, 5142 (2022).
- P. Fürtjes, J. Tomm, U. Griebner, G. Steinmeyer, S. Balabanov, E. Gavrishchuk, and T. Elsaesser, "Kinetics of excitation transfer from Cr^{2+} to Fe^{2+} ions in co-doped ZnSe", Opt. Lett. **47**, 2 (2022).
- M. Duda, L. von Grafenstein, M. Bock, D. Ueberschaer, P. Fuertjes, L. Roškot, M. Smrž, O. Novák, and U. Griebner, "10-µJ few-cycle 12-µm source based on difference-frequency generation driven by a 1-kHz mid-wave infrared OPCPA", Opt. Lett. **47**, 2891 (2022).
- P. Fuertjes, M. Bock, L. von Grafenstein, D. Ueberschaer, U. Griebner, and T. Elsaesser, "Few-cycle 65-µJ pulses at 11.4 µm for ultrafast nonlinear longwave-infrared spectroscopy", Optica **9**, 11 (2022).

Conference contributions

The speaker is underlined

- Pia Johanna Fürtjes, Lorenz von Grafenstein, Chao Mei, Uwe Griebner, and Thomas Elsaesser, "OPCPA Front-End based on a Cr:ZnS Laser for Femtosecond Pulse Generation in the Mid-Infrared" in CLEO Europe June 2021, online
- Pia Johanna Fürtjes, Lorenz von Grafenstein, Chao Mei, Uwe Griebner, and Thomas Elsässer, "Soliton Self-Frequency Shifted Signal Generation in a Cr:ZnS Based Tunable Sub-100 fs MWIR OPCPA" in ASSL October 2021, online

- Pia Johanna Fürtjes, Martin Bock, Lorenz von Grafenstein, Uwe Griebner, and Thomas Elsaesser, "LWIR OPCPA based on a Cr:ZnS front-end" in Mid-infrared Coherent Cources conference March 2022, Budapest
- Pia Johanna Fürtjes, Martin Bock, Lorenz von Grafenstein, Uwe Griebner, and Thomas Elsaesser, "LWIR OPCPA based on a Cr:ZnS front-end" in Europhoton September 2022, Hannover
- Pia Johanna Fürtjes, Martin Bock, Lorenz von Grafenstein, Uwe Griebner, and Thomas Elsaesser, "LWIR OPCPA at 11.4 µm delivering 65 µJ femtosecond pulses at 1 kHz repetition rate" in Europhoton December 2022, Barcelona

C

Selbstständigkeitserklärung

Ich erkläre, dass ich die Dissertation selbständig und nur unter Verwendung der von mir gemäß § 7 Abs. 3 der Promotionsordnung der Mathematisch-Naturwissenschaftlichen Fakultät, veröffentlicht im Amtlichen Mitteilungsblatt der Humboldt-Universität zu Berlin Nr. 42/2018 am 11.07.2018 angegebenen Hilfsmittel angefertigt habe.

Berlin, den

Pia Johanna Fürtjes

D

Danke

An dieser Stelle möchte ich mich bei all jenen bedanken, ohne die es mir nicht möglich gewesen wäre, diese Arbeit erfolgreich fertigzustellen. Zunächst danke ich Prof. Thomas Elsässer für die Möglichkeit, am Max-Born-Institut unter so guten Bedingungen meine Dissertation angefertigt haben zu dürfen. Ich danke meinem Projektleiter Uwe Griebner, der mich tagtäglich mit seinem jahrelangen Wissen unterstützt hat und mit mir immer wieder alle Details durchgegangen ist. Ein großes Danke geht an Lorenz, der mir zwei Jahre lang alle meine Fragen beantwortet hat! Danke für dein immer offenes Ohr, deine Herzlichkeit und deine Unterstützung.

Danke schön auch an Dennis und Martin, für die Hilfe und die gute Zeit im Labor. Ein besonderer Dank geht an Isabel und Azize, für die gemeinsamen Mittagessen, für die aufbauenden Gespräche, wenn es sich so angefühlt hat, als würde mal wieder gar nichts funktionieren, und sonst auch.

Ein herzliches Dankeschön geht auch an meine Mitbewohnerin Anne, für die aufmunternde Abende bei gutem Essen und Wein nach langen Labortagen. Danke an meine Eltern, auf die ich mich immer verlassen kann und die immer wieder betonen, wie stolz sie auf mich sind.

Zum Schluss danke ich meinem liebsten Sebastian, für all die aufbauenden Worte, das Feiern von Erfolgen, die Ablenkung von der Arbeit und die wundervolle gemeinsame Zeit.